DEVELOPMENT AND CHARACTERIZATION OF HIGH-PERFORMANCE AMMONIA BORANE BASED ROCKET PROPELLANTS

by

Michael Baier

A Dissertation

Submitted to the Faculty of Purdue University

In Partial Fulfillment of the Requirements for the degree of

Doctor of Philosophy

School of Aeronautics and Astronautics

West Lafayette, Indiana

August 2021

THE PURDUE UNIVERSITY GRADUATE SCHOOL
STATEMENT OF COMMITTEE APPROVAL

Dr. Steven Son, Chair
School of Aeronautics and Astronautics

Dr. Robert Lucht
School of Mechanical Engineering

Dr. Timothée Pourpoint
School of Aeronautics and Astronautics

Dr. Christopher Goldenstein
School of Mechanical Engineering

Approved by:
Dr. Gregory Blaisdell

To the late Dr. Karl Reid, who helped encourage me to start my PhD,
To my girlfriend Kim, whose continued love and support helped encourage me to finish my PhD,
And to my family, who supported me every step of the way.

ACKNOWLEDGMENTS

I would first like to thank my advisor Dr. Steven Son for all his guidance over the past several years. His willingness to take me on as a graduate student and constant support have helped shape me into the researcher I am today. I would also like to express my thanks to the other members of my advisory committee: Dr. Robert Lucht, Dr. Timotheé Pourpoint, and Dr. Christopher Goldenstein, for all their assistance and guidance in the various research efforts undertaken in the course of this work. Likewise, I would also like to thank Dr. Ramachandran and his students for their assistance in preparing much of the ammonia borane (and other amine-boranes) used over the course of this work.

Next, I would like to express my gratitude to all the staff and personnel who keep the Zucrow labs running smoothly and safely. I would particularly like to thank Jason Gabl, for all his guidance over the years with regards to safely and effectively performing much of the hypergolic propellant work discussed throughout this dissertation. In addition, I would also like to thank Aman Satija for all his invaluable insights into the complex world of laser diagnostics.

I would also like to thank all the graduate student colleagues I have had the pleasure of knowing over the course of the past six years. Graduate school is an inherently transient period and I'm glad to have gotten the opportunity to share my journey through graduate school with you all. Special thanks are due to Kate Clements, Austin McDonald, Chris Jarocki, and Andrew Noel for their willingness to help me complete many of the experimental efforts outlined in this work. I could not have done it all without you all, and I am truly grateful for your help over the years.

Finally, I would like to thank NASA for their financial support through the Space Technology Research Fellowship (grant number 80NSSC17K0177) awarded to me to undertake

this work. This work was also supported in part by the Army Research Office through grant number W911NF-15-1-0201.

TABLE OF CONTENTS

LIST OF TABLES

LIST OF FIGURES

ABSTRACT

Historically, hypergolic propellants have utilized fuels based on hydrazine and its derivatives due to their good performance and short ignition delays with the commonly used hypergolic oxidizers. However, these fuels are highly toxic and require special handling precautions for their use.

In recent years, amine-boranes have begun receiving attention as potential alternatives to these more conventional fuels. The simplest of these materials, ammonia borane (AB, NH_3BH_3) has been shown to be highly hypergolic with white fuming nitric acid (WFNA), with ignition delays as short as 0.6 milliseconds being observed under certain conditions. Additionally, thermochemical equilibrium calculations predict net gains in specific impulse when AB based fuels are used in place of the more conventional hydrazine-based fuels. As such, AB may serve as a relatively less hazardous alternative to the more standard hypergolic fuels.

Presented in this work are the results of five major research efforts that were undertaken with the objective of developing high performance fuels based on ammonia borane as well as characterizing their combustion behavior. The first of these efforts was intended to better characterize the ignition delay of ammonia borane with WFNA as well as investigate various fuel binders for use with ammonia borane. Through these efforts, it was determined that Sylgard-184 silicone elastomer produced properly curing fuel samples. Additionally, a particle size dependency was observed for the neat material, with the finer particles resulting in ignition delays as short as 0.6 milliseconds, some of the shortest ever reported for a hypergolic solid fuel with WFNA.

The objective of the second area of research was intended to adapt and demonstrate a temperature measurement technique known as phosphor thermography for use with burning solid propellants. Using this technique, the surface temperature of burning nitrocellulose (a

homogeneous solid propellant) was successfully measured through a propellant flame. During the steady burning period, average surface temperatures of 534 K were measured across the propellant surface. These measured values were in good agreement with surface temperature measurements obtained elsewhere with embedded thermocouples (T = 523 K). While not strictly related to ammonia borane, this work demonstrated the applicability of this technique for use in studying energetic materials, setting the groundwork for future efforts to adapt this technique further to studying the hypergolic ignition of ammonia borane.

The third research area undertaken was to develop a novel high-speed multi-spectral imaging diagnostic for use in studying the ignition dynamics and flame structure of ammonia borane. Using this technique, the spectral emissions from BO, BO_2, HBO_2, and the B-H stretch mode of ammonia borane (and its decomposition products) were selectively imaged and new insights offered into the combustion behavior and hypergolic ignition dynamics of ammonia borane. After the fuel and oxidizer came into contact, a gas evolution stage was observed to precede ignition. During this gas evolution stage, emissions from HBO_2 were observed, suggesting that the formation of HBO_2 at the AB-nitric acid interface may help drive the initial reactant decomposition and thermal runaway that eventually results in ignition. After the nitric acid was consumed/dispersed, the AB samples began burning with the ambient air, forming a quasi-steady state diffusion controlled flame. Emission intensity profiles measured as a function of height above the pellet revealed the BO/BO_2-based emissions to be strongest in the flame zone (corresponding to the highest gas temperatures). Within the inner fuel-rich region of the flame, the HBO_2 emission intensity peaked closer to the fuel surface after which it unexpectedly began to decrease across the flame zone. This is seemingly in contradiction to the current understanding that HBO_2 is a stable

product species and may suggest that for this system it is consumed to form BO_2 and other boron oxides.

The fourth area of research undertaken during this broader research effort investigated the use of ammonia borane and other amine borane additives on the ignition delay and predicted performance of novel hypergolic fuels based on tetramethylethylenediamine (TMEDA). Despite these materials being in some cases only sparingly soluble in TMEDA, solutions of ammonia borane, ethylenediamine bisborane, or tetramethylethylenediamine bisborane in TMEDA resulted in reductions of the mean ignition delays of 43-51%. These ignition delay reductions coupled with the significantly reduced toxicity of these fuels compared to the conventional hydrazine-based hypergolic fuels make them promising, safer alternatives to the more standard hypergolic fuels. Attempts were made to improve these ignition delays further by gelling the TMEDA, allowing for amine borane loadings beyond their respective solubility limits. Moving to these higher loadings had mixed results however, with the ignition delays of the AB/EDBB-based fuels increasing significantly with higher AB/EDBB loadings. The ignition delays of the TMEDABB-based fuels on the other hand decreased with increasing TMEDABB loadings, though the shortest were still comparable to those found with the saturated fuel solutions.

The final research area that was undertaken was focused on scaling up and developing fuel formulations based on ammonia borane for use in a small-scale hypergolic hybrid rocket motor. Characterization of the regression rate behavior of these fuels under motor conditions suggested the fuel mass flow rate was driven primarily by the thermal decomposition of the ammonia borane. This mechanism is fundamentally different from that which governs the regression rate of most conventional solid fuels used in hybrid rockets as well as that of ethylenediamine bisborane, a similar material in the amine borane family of fuels. Understanding this governing mechanism

further may allow for its exploitation to enable high, nearly constant fuel mass flow rates independent of oxidizer mass fluxes. If successful, this would enable further optimization of the design for rocket systems utilizing these fuels, resulting in levels of performance that rival that of the more conventional hydrazine-based fuels.

1. INTRODUCTION

1.1 Motivation

Since their discovery in the early 1930s, hypergolic propellants have been a mainstay of liquid rocket systems. This class of propellants consists of combinations of fuels and oxidizers that, upon contact, self-ignite through heat generated by chemical reactions between the fuel and oxidizer. This can simplify the overall complexity of rocket systems employing these propellants due to the elimination of a dedicated ignition source. While a wide range of fuel and oxidizer combinations exhibit this property, only a select few have offered the physical properties and performance necessary to make them viable in fielded rocket systems.

While these propellants can be reliable and improve the versatility of systems using them, they are generally toxic and highly hazardous to handle. As such, there remains a significant drive to develop novel fuels and oxidizer that offer comparable (or better) performance without the drawbacks of the standard hypergolic propellants. Unfortunately, few viable alternatives have been found due to the complexity of the reactions governing hypergolic ignition making it difficult to predict the hypergolic characteristics of fuels/oxidizers based on their physical/chemical properties.

1.2 Objectives

The primary objective of both the previously performed work and the proposed work discussed here is to develop and characterize high-performance ammonia borane based solid fuels for use in hypergolic hybrid rocket motors. This will be achieved by progressing from small scale hypergolic ignition experiments (to better characterize ammonia borane) to lab scale hybrid motor testing. The regression rate and surface combustion behavior of these fuels under typical motor conditions will also be characterized using an optically accessible hybrid motor configuration.

Additionally, as ammonia borane is the simplest fuel in the broader amine-borane family of fuels, better understanding its combustion behavior may provide additional insights into the behavior of amine-boranes in general. As such, an additional objective of this work is to develop/adapt various diagnostic techniques (e.g., phosphor thermometry, multi-spectral imaging, etc.) to offer novel insights into the combustion behavior and, more importantly, the hypergolic ignition dynamics of these fuels.

1.3 Organization

The remainder of this document has been broken up into several chapters to aid in organizing the major aspects of this work. Chapter 2 is a literature review covering the major topics relevant to the previously performed work and proposed future research efforts.

Chapters 3 through 7 cover the major research efforts that have been previously undertaken in the course of this work. Chapter 3 summarizes the initial efforts undertaken to further characterize the hypergolic behavior of ammonia borane in addition to investigating several different fuel binders for potential use with ammonia borane. The objectives of the work covered in chapter 4 was to investigate the feasibility of adapting phosphor thermography for use with homogeneous solid propellants. While not strictly relevant to the overall topic of this work, it served as an initial step towards further adapting this technique for use with hypergolic hybrid propellants. Chapter 5 covers a novel high-speed multi-spectral imaging technique used to investigate the ignition dynamics and flame structure of ammonia borane. Chapter 6 covers experimental efforts investigating the impacts of ammonia borane (and other amine borane additives) on the ignition delay and predicted performance of TMEDA (a less hazardous alternative to hydrazine). Chapter 7 discusses and presents efforts undertaken to scale up and test fuel grains based on ammonia borane in a hypergolic hybrid rocket motor operating with white

fuming nitric acid as the oxidizer. Finally, Chapter 8 provides a brief overview of the major conclusions obtained during this work as well as some suggestions for future research directions.

2. BACKGROUND

2.1 Hypergolic propellants

Unlike conventional liquid bi-propellant systems that require the use of a dedicated ignition system, hypergolic propellants are uniquely capable of self-ignition upon contact between the fuel and oxidizer. Not only does this capability reduce the overall complexity of any systems employing these propellants (by not requiring a separate ignition system), but it also makes these systems capable of reliable reignition for more complex flight profiles.

For most systems actively fielding hypergolic propellants, the oxidizers most commonly used are typically based on nitric acid, nitrogen tetroxide (NTO, N_2O_4), or some combination of the two. While concentrated hydrogen peroxide (i.e., high-test hydrogen peroxide) exhibits hypergolic ignition behavior with a number of different fuels, the self-decomposition it undergoes (forming oxygen and water) can introduce long-term storage concerns. On the fuel side, these systems typically utilize a fuel based on hydrazine or its derivatives (e.g., monomethyl hydrazine, unsymmetrical dimethylhydrazine). The non-cryogenic nature of these propellants makes them storable for long term use (i.e., maneuvering systems for satellites/spacecraft) or for missile systems that are kept in launch-ready status for extended durations. While these fuels and oxidizers offer good performance and have been well characterized, the health hazards associated with them has led to considerable research into potential alternatives that maintain (or improve) performance while being safer to handle. To date however, a limited understanding of the fundamental chemical kinetics that govern hypergolic ignition processes has hindered the development of viable alternatives [1, 2].

When evaluating the performance of novel hypergolic propellant combinations, one of the more pertinent parameters to consider is the ignition delay (i.e., how long it takes for ignition to

occur after the fuel and oxidizer come into contact). This parameter is particularly relevant for liquid bipropellant hypergolic propellants, as they begin mixing upon contact. If the ignition delay of a given propellant combination is too long, an excessive amount of fuel and oxidizer can accumulate and mix within a motor's combustion chamber. Once ignition does occur, the rapid ignition and combustion of the accumulated propellants results in a large pressure spike (commonly referred to as a "hard start"). Depending on the magnitude of this pressure spike, in some cases this can result in damage occurring to the combustion chamber or potentially even an explosion. While short ignition delays are generally ideal (particularly for reaction control systems used for attitude control), care must be taken to ensure that the fuels and oxidizers do not impinge/combust too close to the injector as this can result in damage to the injector assembly. This can often be mitigated through careful injector design, however.

2.2 Amine-boranes

Amine-boranes, as their name suggests, are a family of compounds that consist of a base amine that has been complexed with borane (BH_3) adducts [2, 3]. It has been demonstrated previously that the complexation of amines with borane adducts can result in dramatic improvements in the ignition delay of these materials compared to the base amine material [2]. For example, while ammonia is not hypergolic with white fuming nitric acid (WFNA), ammonia borane has been shown to be highly hypergolic with WFNA, with sub-millisecond ignition delays being reported in some cases [2-6]. Additionally, converting an amine to its corresponding amine-borane can help mitigate some of the safety hazards associated with them, as many amine boranes are air-stable solid materials compared to the base amines that are generally liquid/gaseous materials [2, 3, 7].

Amine-boranes were first considered for use as hypergolic fuels by Gao and Shreeve in 2012, where they evaluated ammonia borane, hydrazine borane, and hydrazine bisborane as additives for ionic liquid hypergolic fuels [8]. However, boranes (and other boron hydrides) have long been considered for use in propulsive applications, most notably during the 1940s and 1950s for potential high energy jet fuels [9]. Likewise, the hypergolic properties of amine-based materials (including hydrazine and other related materials) have been investigated extensively since the early years of liquid rocket propellant research [1, 2, 10]. Much of the amine-borane hypergolic propellant work that followed Gao and Shreeve's initial work has been performed at Purdue University. Ramachandran et al. and Pfeil Et al. investigated a number of different amines and their corresponding amine-boranes to better characterize the hypergolic nature of these fuels [2, 3]. Following this initial work, Pfeil et al. proceeded to further investigate ethylenediamine bisborane (EDBB) for use as a hypergolic solid fuel, eventually culminating a series of small scale motor tests being performed with WFNA as the oxidizer [7, 11]. Triethylamine borane (TEAB, a liquid amine borane) has also been shown considerable promise with ignition delays (with WFNA) comparable to MMH with RFNA [12-14] .

While it is the simplest compound in the amine-borane family of fuels, ammonia borane (NH_3BH_3) appears to be one of the more promising fuels for potential use in propulsion applications. First synthesized by Shore and Perry in 1955, ammonia borane has historically been studied primarily for its potential use as a solid-state hydrogen storage medium [15-18]. While only containing 19.6% hydrogen by mass, the higher density of ammonia borane (being a solid material) results in a higher hydrogen density than liquid hydrogen itself without requiring cryogenic storage systems.

Despite all the research related to ammonia borane since it was first synthesized, its hypergolic ignition behavior has only recently been reported. Initial ignition delay experiments performed by Gao and Shreeve reported ignition delays with WFNA on the order of 80 milliseconds [8]. However, Ramachandran et al. found consistent ignition delays of 2 milliseconds for AB when tested with WFNA [2]. Further studies of the ignition delay of AB with WFNA have been more consistent with the results reported by Ramachandran et al., with ignition delays as short as 0.6 milliseconds being observed in some cases [2-6].

One of the issues that has prevented additional studies of ammonia borane in solid and hybrid propellant systems is the fact that AB is incompatible with many of the fuel binders commonly in use. Lee et al. investigated using ammonia borane in a HTPB-AP composite propellant and found that adding AB prevented the propellant from curing properly [19]. Lee argued that the AB was likely reacting with the isocyanates and, as a result, preventing the full crosslinking of the HTPB. Considering this, Weismiller et al. incorporated ammonia borane into paraffin wax (a thermoplastic material) to successfully prepare fuel grains for use in a hybrid motor with gaseous oxygen [20]. While the addition of 10% AB (by mass) to the fuel grain improve the fuel's regression rate slightly, 20% and 50% AB loadings resulted in net decreases in the regression rate compared to the baseline paraffin grains [20]. Despite this however, the tests performed with these fuel grains resulted in high combustion efficiencies (e.g., greater than 90%) for all the tested loadings of AB.

2.3 Hybrid propellants

As their name suggests, hybrid propellants are a class of rocket propellants that occupy a sort of middle ground between conventional solid and liquid propellants. Unlike these more conventional propellants where the fuel and oxidizer exist in the same physical state, the fuel and

oxidizer for hybrid propellant systems are stored in separate physical states. For "classical" hybrid configurations (with a typical hybrid motor configuration shown in Figure 1, the fuel is typically a solid whereas the oxidizer is a liquid/gas. "Reverse" hybrids (i.e., a solid oxidizer and liquid/gaseous fuel) have been investigated, though work along these lines has been relatively limited.

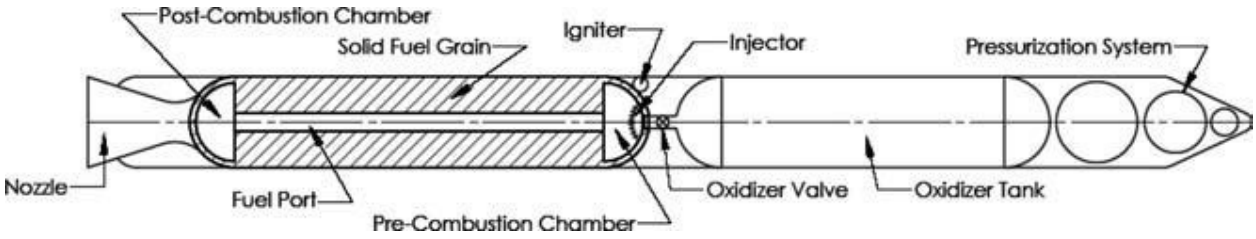

Figure 1: Typical hybrid rocket motor schematic [21]

The phase difference between the fuel and oxidizer makes hybrid systems inherently safer than solid/liquid systems as the fuel and oxidizer cannot mix intimately should a failure occur. Additionally, depending on the exact fuel composition used, the relatively inert nature of the solid fuels used for these systems greatly reduces the hazards associated with manufacturing/transporting the fuel grains. In comparison to liquid bi-propellant systems, hybrid systems are also simpler as only one flow system is required instead of the two required for liquid bi-propellants. Hybrid propellants can also offer improved versatility relative to solid propellants as the oxidizer can throttled as needed for more complex flight profiles and, in some cases, shut off entirely.

Hybrid propellants aren't without their drawbacks, however. While having the fuel and oxidizer in different physical states makes these systems safer, it does limit the rate at which the two can interact during normal operations. Additionally, the solid fuels used in hybrid systems generally suffer from relatively slow regression rates resulting in low fuel mass flow rates. Compensating for these low fuel regression rates generally requires complex multi-port grain

geometries (e.g., Figure 2), increasing the complexity of grain manufacturing. As these grains cannot be burned to completion due to the potential for fuel slivers being ejected from the grain and potentially clogging the nozzle, some fraction of the fuel mass is retained, effectively increasing the system inert mass. Depending on the required thrust profile, these complex multi-port grain designs may also have poor bulk densities due to the empty volume required for the initial fuel surface area.

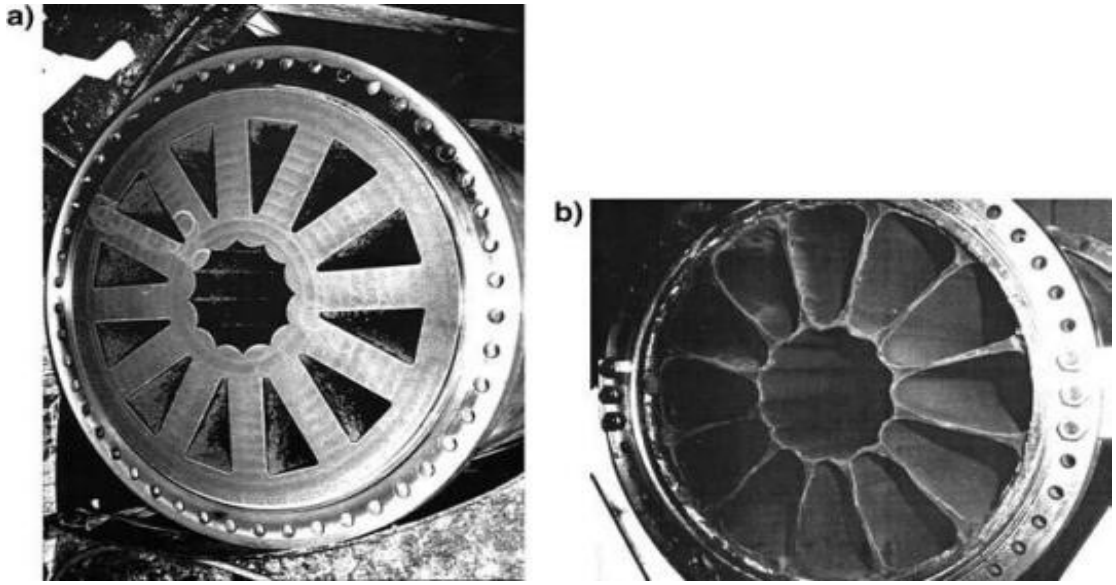

Figure 2: Example multiport hybrid fuel grain design before (A) and after (B) firing [22]

As the fuel and oxidizer are stored separately for hybrid motors, the mechanics that govern the regression rate are much different than those of solid propellants. The burning rate of solid propellants is primarily dependent on pressure (though other factors can play a role as well) as per the relation,

$$r = aP^n$$

where r is the burning rate, P is the chamber pressure, and a/n are empirically obtained coefficients for a given propellant formulation [23]. For hybrid propellants however, as the oxidizer is injected

into the combustion chamber separately from the fuel, the combustion behavior is largely diffusion controlled.

Early work by Marxman, Wooldridge, Muzzy, and others in the 1960's resulted in a boundary-layer heat-transfer-limited model for the flame structure/combustion behavior of hybrid propellants [24-27]. An illustration of the proposed combustion model can be found in Figure 3. Within the boundary layer, distinct oxidizer and fuel rich regions form in the upper and lower regions of the boundary layer respectively, with the flame zone being situated between the two. As the name suggests, the regression rate for the heat-transfer-limited model is strongly dependent on the rate at which heat is transferred to the solid fuel through convection [21, 24, 26, 27]. For hybrid propellants that do not exhibit significant thermal radiation, the regression rate for the heat-transfer-limited model was expressed by Marxman, Wooldridge, and Muzzy to be

$$\rho_f \dot{r} = 0.036 G^{0.8} \left(\frac{x}{\mu}\right)^{-0.2} B^{0.23}$$

where ρ_f is the solid fuel density, $\dot{r}$ is the regression rate, G is the local mass flux, x is the distance from the leading edge of the fuel grain, μ is the viscosity of the oxidizer gas flow, and B is the mass transfer number/blowing coefficient for the system. As the regression rate is largely dominated by the mass flux G, this relation is often simplified to the form

$$\dot{r} = aG^n$$

where a and n are empirical constants associated with a given propellant formulation/system configuration.

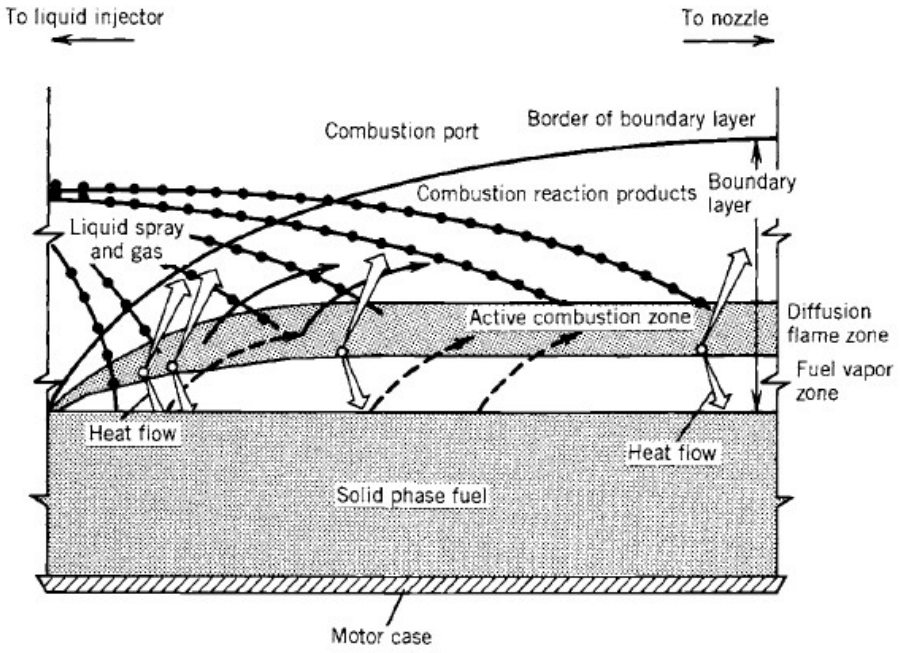

Figure 3: Hybrid propellant flame structure [23]

While Marxman's heat-transfer-limited model predicted regression rates that were in good agreement with experimental results for relatively simple systems, it did not account for the pressure dependencies observed for under certain experimental conditions [28]. Smoot and Price performed a series of slab burner hybrid experiments with a variety of fuel and oxidizer combinations as well as varying operating conditions [28-32]. Following a similar analysis as Marxman et al. and incorporating the effects of condensed species at the wall, Smoot and Price developed regression rate equations

$$\dot{r} = 0.03\left(\frac{G^{0.8}}{\rho_f \lambda}\right)\left(\frac{\mu}{x}\right)^{0.2} \ln\left[1 + \left(\frac{\lambda B}{Pr^{2/3}}\right)\right]$$

$$\dot{r} = 0.023\left(\frac{G^{0.8}}{\rho_f \lambda}\right)\left(\frac{\mu}{D}\right)^{0.2} \ln\left[1 + \left(\frac{\lambda B}{Pr^{2/3}}\right)\right]$$

for turbulent boundary layer and fully developed boundary layer cases respectively [21, 28, 29].

As with Marxman's results, Smoot and Price's regression rate equation predicted the regression rate to scale with mass flux to the 0.8th power. While this was in good agreement with experimental results for low mass fluxes, Smoot and Price found that for higher mass fluxes and low pressures, the regression rate behavior begins to diverge from the predicted $G^{0.8}$ behavior, becoming largely flux independent. Within this high mass flux regime, the regression rate was found to increase with pressure for a given mass flux until the value predicted by the $G^{0.8}$ relation is reached [28]. While the exact behavior varied depending on the fuel/oxidizer used, the trends observed by Smoot and Price were generally similar to the results shown in Figure 4. To better reflect this behavior, Smoot and Price suggested the empirical relation for the regression rate,

$$\dot{r} = \frac{abG^{0.8}P^n}{aG^{0.8} + bP^n}$$

where P is the motor chamber pressure and a/b/n are empirical constants corresponding to a particular fuel/oxidizer formulation.

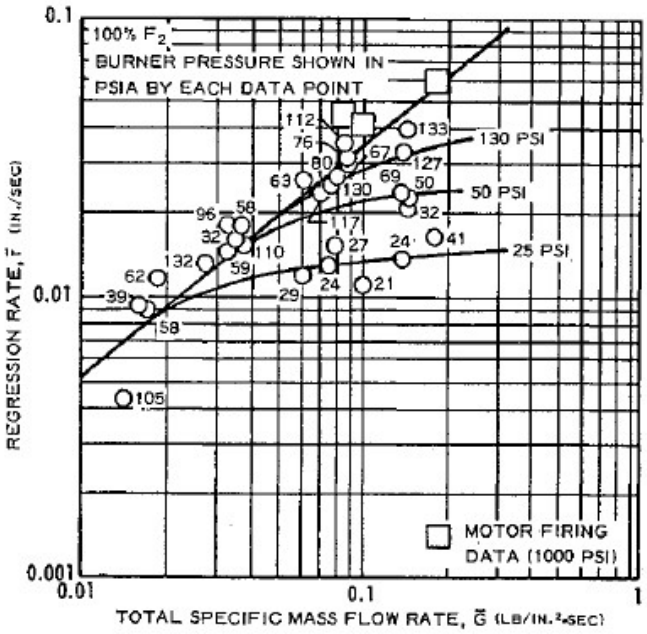

Figure 4: Regression rate behavior as a function of mass flux and burner pressure for butyl rubber grains with gaseous fluorine [28]

The exact cause for this pressure dependence at high mass fluxes has resulted in considerable debate within the hybrid propellant research community [21, 33]. While the explanations offered varied from system-to-system (and researcher to researcher), the cause of this pressure dependency is generally argued to fall into one of three categories: 1) heterogeneous surface reactions due to the oxidizer reaching the solid fuel, 2) gas phase chemical kinetics, and 3) some combination of 1) and 2) [21]. For hypergolic hybrid propellants, where liquid oxidizer often impinges directly on the fuel surface, the potential role of surface reactions on the fuel regression rate is particularly relevant. Experimental studies of hypergolic hybrid have shown to some extent evidence of heterogeneous surface oxidation, though direct observations of this behavior have yet to be made [7, 28, 29, 31, 34-36]. The pressure threshold below which the regression rate of solid fuels shows a pressure dependence varies considerably in the literature with mass flux and fuel/oxidizer composition [28-31, 33-37]. In practice however this pressure threshold is generally thought to be somewhere in the range of 150-250 psia [28, 29, 31, 37].

2.4 Phosphor Thermography

While embedded thermocouples have been historically used for measuring the surface temperature of burning solid propellants, they suffer from significant thermal lag, making them unsuitable for studying combustion phenomena requiring fast temporal responses. Additionally, by virtue of their physical size, thermocouples have an averaging effect which can introduce additional errors when investing thin reaction/combustion zones. While these effects can be mitigated to some extent by reducing the size of the thermocouple, doing so can result in material/reliability issues.

In more recent years, a technique known as phosphor thermography has been receiving increased attention as a potential alternative to other more established techniques. Phosphor

thermography is an optical temperature measurement technique that makes use of the temperature dependent emissions or decay time of excited thermographic phosphor particles. Generally, these materials consist of a ceramic host material (e.g. Al_2O_3, Y_2O_3, ZnO, etc.) that has been doped with rare-earth or transition metal activator ions (e.g. Cr^{+3}, Eu^{+3}, etc.) [38]. When these particles absorb energy from an excitation source (typically a laser), the rate at which the activator ions return to their ground state is controlled by competing radiative and non-radiative processes. As the name implies, the radiative energy transfer mechanism corresponds to the emission of a photon. For the non-radiative transfer mode, the absorbed energy is transferred between different energy modes, resulting in a net change in the particle's internal energy. This corresponds to a change in the populations of the vibrational levels for the ground and excited states which in turn affects the strength/position of the allowed spectral lines [39]. Like pyrometry and other optical temperature measurement techniques, phosphor thermography is a relatively less intrusive technique. As this technique requires adding phosphor particles to the system of interest, the concentration of phosphor particles used will determine how much the system is affected.

Most applications using phosphor thermography for performing temperature measurements use either the lifetime decay or intensity ratio methods. As its name suggests, the lifetime decay method makes use of the fact that the intensity of the phosphor emissions decays roughly exponentially according to,

$$I(t) = I_0 \exp\left(-\frac{t}{\tau}\right), \tag{1}$$

where I_0 is the initial emission intensity, I(t) is the time dependent intensity, t is the time, and τ is the decay time constant of the phosphor [40]. As the temperature of the phosphor particles increases, the lifetime of the phosphor emission decreases. By recording the decay at a number of different known temperatures, the exponential decay curves can be fit to a measured intensity

lifetime curve and provide the corresponding temperature. While this method is generally considered more accurate than the intensity ratio method, it is often limited to point measurements unless a detector system with adequate time resolution is utilized [40].

For the intensity ratio method, the intensity of two different spectral bands relevant to the emission spectrum of a given phosphor are measured after which the ratio of these intensities is taken [38]. The exact spectral bands (and corresponding optical filters) used will vary greatly depending on the type of phosphor used. As the emission spectrum of thermographic phosphor particles varies with temperature, the resulting ratio of the spectral band intensities will also be temperature dependent. By measuring the ratio of the intensities from these spectral bands at a variety of known temperatures, a calibration relationship can be obtained which can then be used to convert measured intensity ratios into temperature. The exact relationship between the intensity ratio and temperature as well as the useful temperature range for a given phosphor can be modified slightly for a given system by varying the spectral bands used.

Depending on the type of detector used, this technique can be used to perform zero, one, or two-dimensional temperature measurements [38]. When used for performing two-dimensional temperature measurements, a single camera or detector with a filter wheel can be used to record one image after the other if the test case is static, slowly varying, or repeatable. However, this approach is often inadequate for more dynamic test cases as slight changes in the surface temperature (and thus the phosphor emissions) between laser pulses/frame acquisitions can cause the measured temperature to vary from the actual temperature. As such, it's necessary to utilize a two-detector configuration to ensure that the two recorded images are captured at the same moment in time. Alternatively, a single detector equipped with a stereoscope or image doubling system can be used so the two filtered images are captured on a single detector at the same time [40].

Maintaining proper alignment between the acquired images is critical for obtaining useful results with this technique, particularly for systems with spatial temperature variations. If the phosphor emissions from different locations on the sample surface are used for obtaining the intensity ratio, the resulting temperature can differ greatly from the actual temperature.

Depending on the application and expected temperature range, the type of phosphor appropriate for obtaining temperature measurements will vary. For high temperature applications, it is often preferred that the phosphor used will emit at shorter/bluer wavelengths of light to reduce interference occurring from blackbody radiation [40]. Phosphors emitting at shorter wavelengths typically have shorter lifetimes as well, enabling them to be used in experiments requiring high temporal resolution. This also enables shorter exposure times to be used to reduce the influence of background emissions, for example from hot gases or particles above a surface, on the measured intensities [41]. Särner et al. investigated several different blue emitting phosphors of which zinc and gallium doped zinc oxide (ZnO:Zn and ZnO:Ga respectively) were shown to be highly temperature sensitive for temperatures between room temperature and 950 K [42]. ZnO:Ga was successfully utilized by Casey et al. to visualize hot spot formation and growth around non-reacting crystals of octahydro 1,3,5,7-tetranitro-1,3,5,7-tetrazocine (HMX) within a simplified plastic bonded explosive when subjected to ultrasonic excitation [43].

Phosphor thermography has been successfully demonstrated previously for use in measuring the surface temperatures of burning solid fuels. Goss et al. presented one of the earliest successful attempts to use this technique for this purpose with their work measuring the surface temperature of a plastic material as it decomposed via laser heating [44]. Later, Vander wal et al. used this approach to measure the surface temperature of the ash layer of a burning charcoal briquette as well as other thermally thin fuels (ashless filter paper, Kimwipes, etc.) [45]. More

recently, this technique has been adapted by Omrane et al. to measure the burning surface temperature of various construction materials (low-density fiberboard, poly(methyl methacrylate), etc.) [46-49].

3. CHARACTERIZATION OF THE HYPERGOLIC IGNITION DELAY OF AMMONIA BORANE

3.1 Introduction

Historically, hypergolic propellant systems have utilized fuels based on hydrazine and its derivatives (e.g. monomethyl hydrazine, unsymmetrical dimethyl hydrazine, etc.). While these fuels are well characterized and offer the performance generally required for these systems, they are highly toxic and hazardous to handle prior to use. As such, there is a strong motivation to develop alternative fuels that offer similar (or better) performance while being less hazardous than the fuels currently in use.

Hypergolic hybrid propellants using less toxic fuels have the potential to improve the safety, reliability, and versatility of rocket systems. Unlike conventional solid propellants, hybrid propellants can be throttled and, in some cases, quenched and reignited as required. This makes them suitable for applications requiring more complex mission or flight profiles. The fact that the fuel and oxidizer exist in different physical states makes hybrid systems inherently safer than liquid systems as the phase difference prevents rapid mixing in the event a failure should occur.

One fuel of interest as a hypergolic solid fuel is ammonia borane (NH_3BH_3) [2, 3, 8]. Under typical atmospheric conditions, ammonia borane is a stable solid material with 19.6 percent hydrogen by mass. Though much of the research related to ammonia borane has focused on its potential as a solid-state hydrogen storage medium [15, 17, 18], its high hydrogen density makes it an attractive fuel for use in rocket systems also. Though it was first synthesized by Shore and Parry in 1955 [16], the hypergolic behavior of ammonia borane has only recently been reported by Gao and Shreeve [8]. Initial results published by Gao and Shreeve suggested ignition delays on the order of 80 milliseconds when tested with white fuming nitric acid (WFNA). However, further

investigation by Ramachandran et al. found consistent ignition delays as short as 2 milliseconds when used with WFNA [2]. These are some of the shortest ever reported for solid hypergolic fuels and could enable ammonia borane to serve as a viable replacement for existing hypergolic liquid fuels.

In the time since it was first synthesized, new synthesis methods have been developed that have the potential to improve the yield of ammonia borane production while simultaneously helping to reduce the cost of synthesis. Ramachandran et al. recently published a water promoted synthesis procedure that produced high yields of ammonia borane with the potential for use in large scale production [50]. At the same time, this procedure is both more cost efficient and safer than previous synthesis methods. These recent developments make ammonia borane more feasible for use in hybrid propulsion systems. The objective of this work is to further characterize ammonia borane as a solid fuel for use in hypergolic hybrid propulsion systems, particularly the ammonia borane produced using this latest novel synthesis method. Efforts devoted to finding a fuel binder that successfully cures with AB as well as the resulting ignition delays with AB incorporated into this binder are also presented.

3.2 Experimental Methods

3.2.1 Fuels

Much of the ammonia borane used in this study was prepared at the H. C. Brown Center for Borane Research at Purdue University. For comparison, commercially available ammonia borane purchased from Sigma-Aldrich was tested also.

A number of different fuel binders were investigated for use with ammonia borane. Prior to the addition of ammonia borane, the different binder components were mixed together (aside from RTV silicone, which was supplied premixed). Polybutadiene acrylonitrile (PBAN) and

carboxyl terminated polybutadiene (CTPB) binders were mixed with Der-331 liquid epoxy resin and cured at 140ºF. Hydroxyl terminated polybutadiene (HTPB) polymer was mixed with isophorone diisocyanate (IPDI) and allowed to cure at room temperature. The commercially available epoxies (specifically Loctite brand 2-hr epoxy and Epoxies, etc. brand flexible epoxy) were mixed with equal parts resin and hardener. Sylgard®-184 silicone elastomer was prepared using a 10:1 base:curative ratio and cured at room temperature for 48 hours.

Ammonia borane composite fuel pellets were prepared by first mixing the Sylgard®-184 base and curative components in a 10:1 ratio by mass. After hand mixing the binder for several minutes, the ammonia borane was gradually added to the mixture and mixed again by hand. Once the ammonia borane was sufficiently wetted by the binder, the mixture was then mixed further on a Resodyn LabRAM resonant mixer for 3 minutes at 80G's acceleration. The mixture was then placed in a vacuum chamber operating at approximately 0.2 psi for 10 minutes to remove any entrained air in the mixture. When mixed at high solids loading (80% by mass), the Sylgard®-184-AB mixture was too dry to be cast-cured into molds. To enable ignition delay testing of high solids loading Sylgard®-184-AB pellets, the mixture was split into roughly 0.25-gram samples and pressed into near maximum density 1 cm diameter pellets for 3 minutes at 10000 psi output pressure using a hydraulic press and pellet press die. After pressing, the pellets were cured for several days at room temperature prior to testing.

3.2.2 Ignition Delay

White fuming nitric acid (WFNA) ignition delay testing was performed using the experimental set up shown in Figure 5. All tests were performed at ambient conditions in air. The 99% purity WFNA used in these tests was purchased from Sigma-Aldrich and was dropped using a 100µl gastight syringe positioned approximately 17.8 cm above the AB samples. AB samples

were placed either on a graphite burn plate or in a PTFE crucible and positioned under the tip of the syringe so that the WFNA droplet fell directly onto the AB. Upon completing a test, any residual AB and WFNA was cleaned from the plate/crucible using deionized water to prevent contamination of future tests. Drop tests were recorded using a color Phantom v7.3 camera and illuminated using a 3x4 array of Cree XLamp XP-G Star LEDs. The ignition delay was defined as the time that passed from when the oxidizer droplet first came into contact with the fuel to when the first visible light was observed as illustrated in Figure 6.

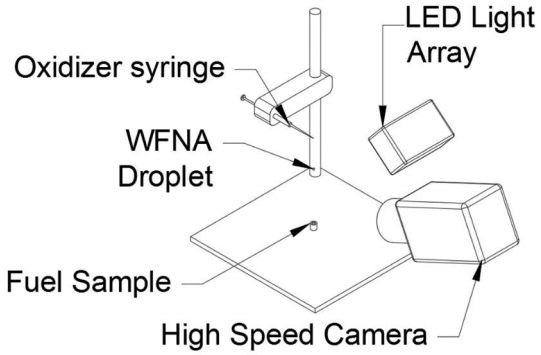

Figure 5: WFNA drop test experimental configuration

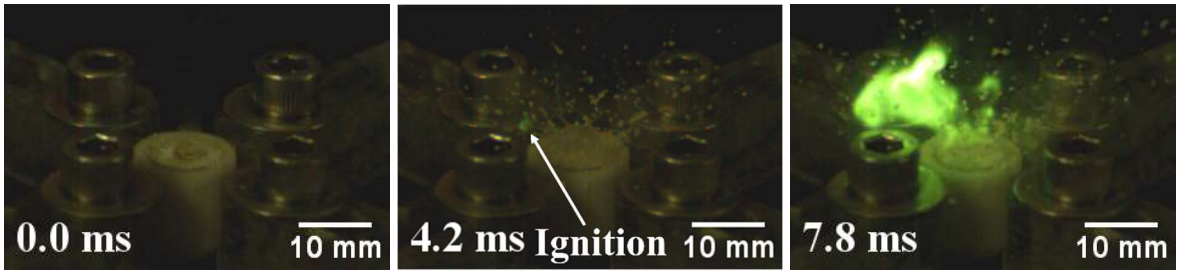

Figure 6: Initial contact between AB and oxidizer droplet (left), First visible light (center), Flame spreads to surrounding particles (right)

Nitrogen tetroxide (NTO) ignition delay tests were performed using a similar experimental set up. Gaseous NTO was allowed to flow into a custom Graham style condenser with cooling water flowing through the coolant jacket. After cooling and condensing the liquid NTO to

approximately 5 ºC, a small valve was opened, releasing a single drop of liquid NTO that then impacted the ammonia borane powder.

3.3 Results and Analysis

3.3.1 Effects of synthesis method on ignition delay

Much of the ammonia borane used later in this study was prepared using the novel water promoted synthesis method developed by Ramachandran et al. [50]. As such, it was necessary to characterize the ammonia borane produced using this method in comparison to other methods. Specifically, ammonia borane produced using the water promoted synthesis method was compared with an ammonia promoted synthesis method [51] as well as a conventional synthesis method [52]. To reduce the effects of varying particle size on ignition delay, the AB used for these initial tests was sieved into two particle size ranges: 45<D<150 μm, and D>150 μm. These particle size ranges were selected to provide a comparison with previously published work by Pfeil et al. [3]. To provide the most accurate comparison between the different synthesis methods, the primary focus of these initial tests was comparing the ammonia borane in the 45-150 μm particle size range. As the synthesis method used to produce it was unknown, the ammonia borane purchased from Sigma-Aldrich was used as provided to provide only a rough comparison with the other synthesis methods.

Ignition delay drop tests were performed using the experimental configuration shown in Figure 5. The results of these tests can be found summarized in Table 1. It was observed that the different synthesis methods produced ammonia borane with comparable ignition delays. However, surprisingly the commercially available AB had ignition delays consistently much shorter than the other synthesized AB.

At first glance, the Sigma-Aldrich AB appeared to be mostly larger particles. However, it was later observed that while there were some large particles in the Sigma-Aldrich supplied AB, many of these particles were aggregates of much finer particles. Representative images obtained using a Hirox KH-8700 optical microscope showing this contrast can be seen in Figure 7. For comparison, optical microscope images of the AB synthesized at Purdue can be seen in Figure 8. The number weighted particle size distributions were then obtained through use of ImageJ open-source image processing software. These size distributions (seen in Figure 9), show that the AB purchased from Sigma-Aldrich was heavily skewed towards particles much finer than the sieved AB tested while the Purdue synthesized AB had a wider distribution. The number weighted distributions were then converted to volume weighted distributions by assuming the AB particles to be roughly spherical. As there were a small number of relatively large particles in both samples, the volume weighted distributions tended to skew more towards larger particles even though most of the particles were smaller. In addition, as the optical microscope images show that the particles are irregular in shape, the spherical particle assumption likely overestimated the volume for the larger particles. In any case, as the different types of sieved AB synthesized at Purdue University produced similar ignition delays for particles within the same particle size range, this would indicate that the shorter ignition delays observed with the Sigma-Aldrich AB was potentially a result of the finer particles present in the tested samples.

Table 1 AB-WFNA ignition delay testing results

AB synthesis method	Particle size range (μm)	Mean ignition delay (ms)	Standard deviation (ms)	Number of tests
Ramachandran et al. [52]	45<d<150	8.00	2.18	3
	d>150	6.50	N/A*	1
Ramachandran et al. [51]	45<d<150	5.17	2.08	3
	d>150	15.00	N/A*	1
Ramachandran et al. [50]	45<d<150	6.50	1.32	3
	d>150	7.67	2.08	3
Sigma-Aldrich (commercial)	Unsieved	1.83	0.29	3

*As only a single test was successfully performed for these particle size ranges, the standard deviation could not be calculated
and the mean listed is the actual ignition delay for that particular test

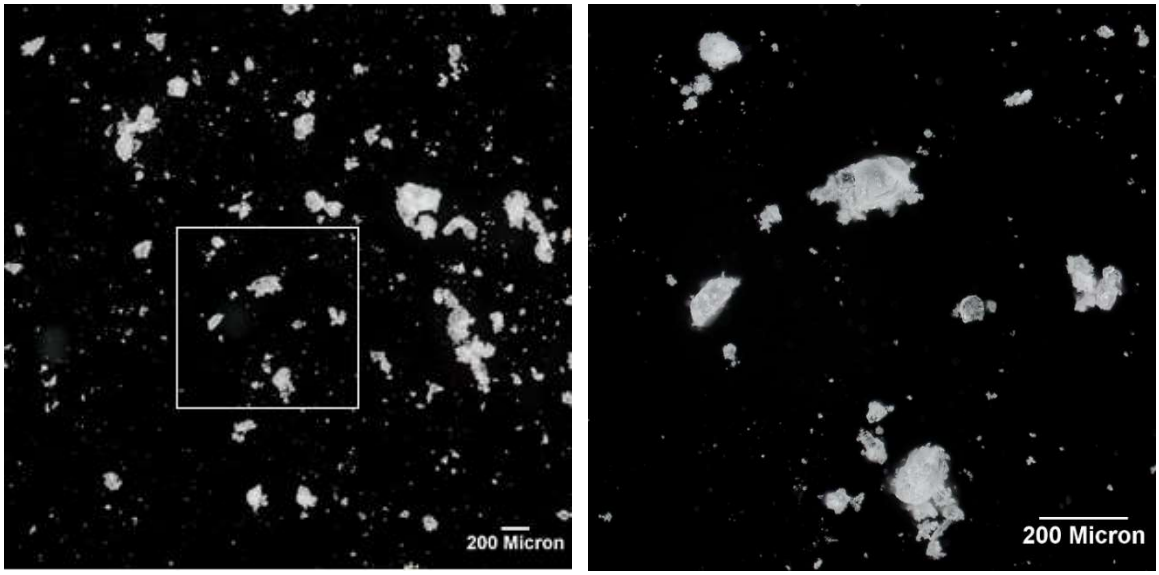

Figure 7: Optical microscope images of ammonia borane purchased from Sigma-Aldrich

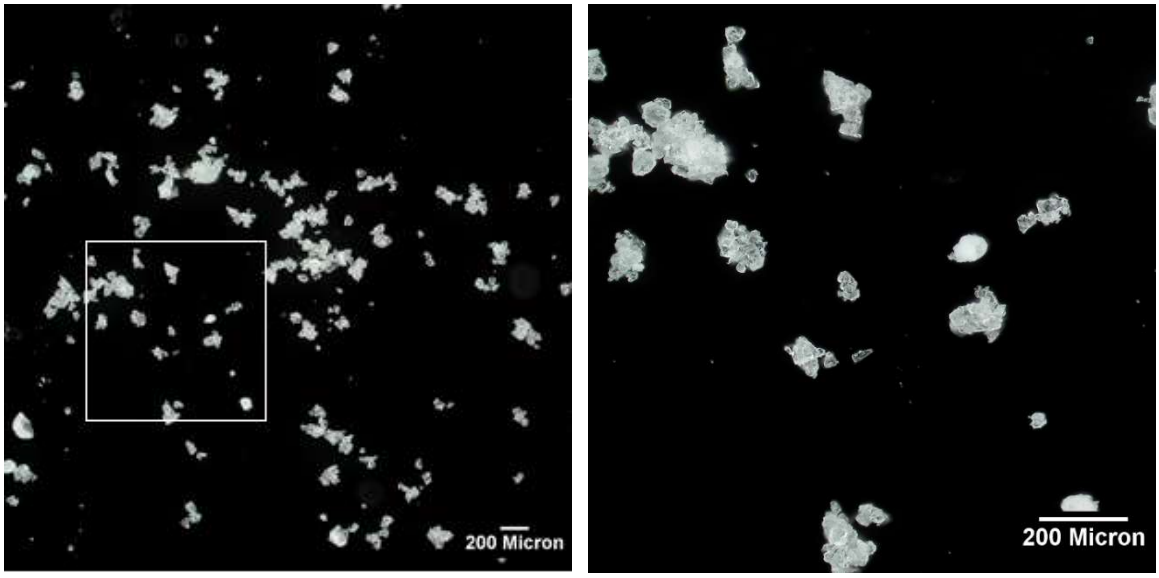

Figure 8: Optical microscope images of ammonia borane synthesized at Purdue University

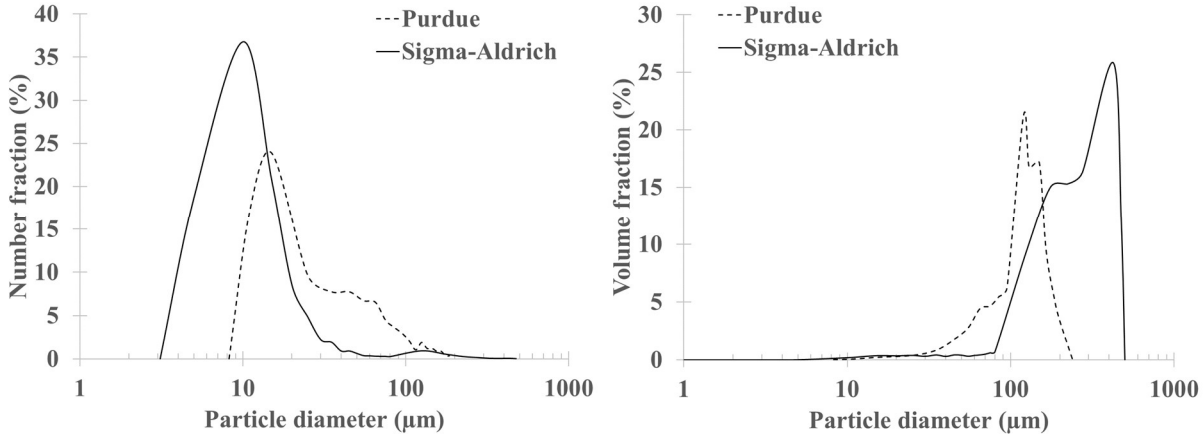

Figure 9: Number weighted particle size distributions (left), Volume weight particle size distributions (right)

3.3.2 Nitrogen tetroxide ignition delay testing

As nitrogen tetroxide (NTO) is one of the more commonly used hypergolic oxidizers, a set of ignition delay tests were performed with AB and condensed NTO. Prior to testing, the ammonia borane used for these tests was sieved into the same particle size ranges used for the WFNA ignition delay tests. The results of these tests are listed in Table 2. While there was significant

variation between tests, in general ignition delays were much longer when NTO was used in place of WFNA. One possible explanation for this trend may be that the reaction mechanism between AB and NTO is inherently slower than that of AB and WFNA. This would only be compounded by the fact that the NTO was chilled to 5°C to keep it condensed while the WFNA was tested at room temperature, possibly slowing the rate of the chemical reactions between the AB and NTO. In any case, the longer ignition delays resulting from the AB-NTO combination would increase the risk of hard starts if used in an actual rocket motor. As such, no further tests were performed using NTO.

Table 2 AB-NTO ignition delay testing results

AB synthesis method	Particle size range (μm)	Mean ignition delay (ms)	Standard deviation (ms)	Number of tests
Ramachandran et al. [50]	45<d<150	102.67	58.07	3
	d>150	57.59	49.97	3

3.3.3 Particle Size Dependency

Previous work published by Bernard et al. found that the ignition delay for single particle solid-liquid hypergolic systems was directly proportional to the square root of the initial particle diameter for the fuels tested (p-phenylenediamine and furfuraldazine) [53]. However, Ranjendran et al. observed an inconsistent trend for several different thiocarbohydrazone based fuels (e.g. Benzaldehyde thiocarbohydrazone, furfuraldehyde thiocarbohydrazone, p-hydroxybenzaldehyde thiocarbohydrazone, etc.) with some having ignition delays remaining roughly constant with changing particle size while others had increasing ignition delays for smaller particle sizes [54].

Additional ignition delay tests were performed to determine if the ignition delay of ammonia borane shows a similar dependency on particle size. Ammonia borane samples (both

synthesized at Purdue and purchased from Sigma-Aldrich) were sieved into the much more precise particle size ranges: D<45 μm (-325 mesh), 45<D<90 μm (-170 +325 mesh), 90<D<150 μm (-100 +170 mesh), 150<D<212 μm (-70 +100 mesh), and D>212 μm (+70 mesh). To ensure adequate amounts of the smaller particles were available for testing, some of the ammonia borane was ground using a mortar and pestle prior to sieving.

Ignition delay tests were again performed using the experimental configuration shown in Figure 5. To improve repeatability between tests as well as promote better contact between the ammonia borane and WFNA droplet, the AB was placed in a small PTFE crucible prior to each test. To help mitigate some of the effects of the WFNA absorbing moisture from the ambient air over time, the testing order for the different particle sizes was randomized. After performing a test for a given particle size range, a different size range was used for the following test until three tests were performed for each of the particle size ranges.

The results of the particle size dependency testing can be found summarized in Table 3 and representative ignition delay tests can be seen in Figure 10 and Figure 11. For AB from both sources, a general trend of ignition delays increasing with increasing particle size was observed. As the Purdue synthesized AB had a higher degree of variation between tests, this trend is more clearly observed with the Sigma-Aldrich AB which was more consistent. Sieving into similar size ranges helped to reduce the difference in ignition delay observed between the two types of AB during initial testing. However, the ignition delays of the commercial AB were generally still shorter than the Purdue synthesized AB, with some ignition delays being as short as 0.6 milliseconds for the D<45 μm particles. As the particle size distribution obtained for the Sigma-Aldrich AB (Figure 9) showed that much of the commercial AB was on the order of 5-20 μm, it's possible that the Purdue synthesized AB was simply not ground to the same extent prior to sieving. This would result in

the Purdue AB being relatively larger than the commercial AB while still passing the 325 mesh (45 μm) sieve.

For both types of AB tested, the most significant test-to-test variation was found to occur for the D>212 μm particles. This may have resulted from some smaller particles clumping into larger aggregates prior to sieving resulting in both large particles and aggregates of small particles in the samples tested. Regardless, almost all the samples ignite in less than 10 ms on average.

Table 3 AB-WFNA ignition delay particle size dependency results

AB synthesis method	Particle size range (μm)	Mean ignition delay (ms)	Standard deviation (ms)	Number of tests
Ramachandran et al. [50]	D<45	4.400	5.200	3
	45<D<90	4.133	1.419	3
	90<D<150	4.533	1.943	3
	150<D<212	8.133	4.496	3
	D>212	22.200	20.117	3
Sigma-Aldrich (Commercial)	D<45	0.733	0.231	3
	45<D<90	1.467	0.115	3
	90<D<150	3.000	1.562	3
	150<D<212	4.000	1.000	3
	D>212	6.133	2.686	3

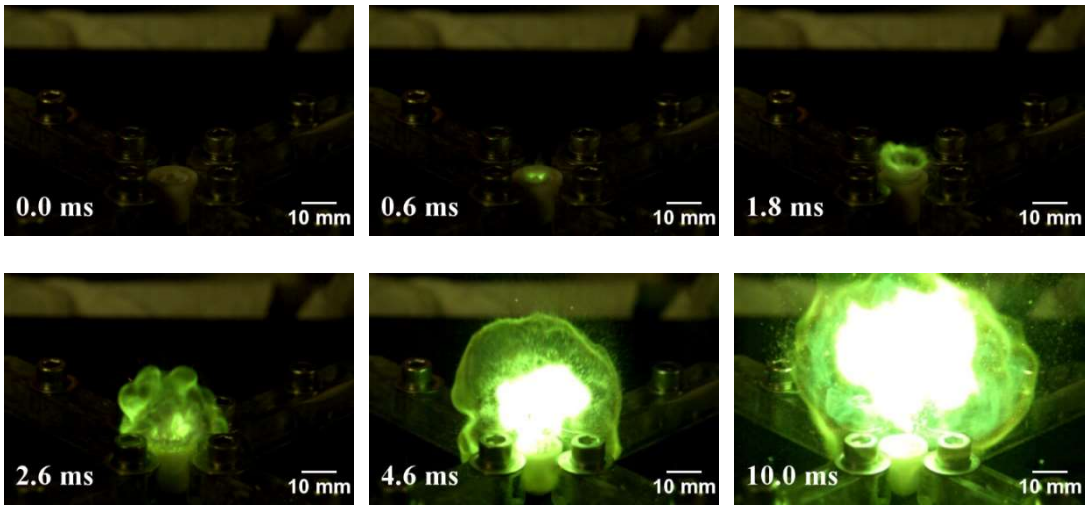

Figure 10: Image sequence of typical ignition delay test of AB powder with WFNA (Sigma-Aldrich, D<45 micron).

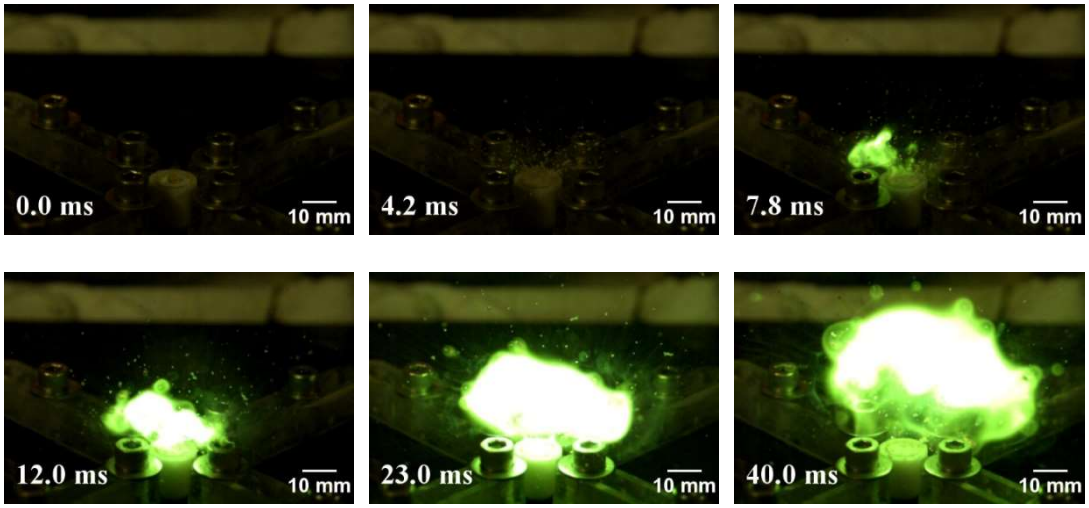

Figure 11: Image sequence of typical ignition delay test of AB powder with WFNA (Sigma-Aldrich, D>212 micron).

3.3.4 Fuel Binder Compatibility Testing

For ammonia borane to be used in a conventional hybrid propellant system, it must first be mixed with a fuel binder to create a fuel grain with adequate mechanical properties. One of the major issues that has prevented further study of ammonia borane in solid and hybrid propellant formulations is that ammonia borane is incompatible with many of the fuel binders commonly

used in propellant formulations [3]. Lee et al. investigated using ammonia borane in a typical HTPB-AP composite propellant and found that adding ammonia borane to the propellant formulation resulted in the propellants failing to cure [19]. Lee suggested that the ammonia borane interfered with the crosslinking process used to cure the HTPB. Weismiller et al. successfully performed small scale motor tests using paraffin wax as a binder for ammonia borane, though the mechanical properties of paraffin may make it less than ideal for use as a fuel binder [20].

In an attempt to find a more suitable binder for use with ammonia borane, a series of binder compatibility tests were performed with a number of different binders. A list of the different binders tested as well as the results of the tests can be found in Table 4. Initial compatibility tests were performed at relatively high solids loadings (i.e., above 50 percent). However, it was observed that for these higher solids loadings incompatibilities present were often obscured by the low amount of binder in the mixtures. When these same mixtures were tested at lower solids loadings (i.e., 10-20 percent), the incompatibilities became more obvious and thus all further compatibility testing was performed at low solids loadings.

Table 4 Binder compatibility testing results

Binder	Notes
HTPB, cured with IPDI	Did not cure
PBAN, cured with Der-331	Cured with small voids, foamed at low solids loading
CTPB, cured with Der-331	Cured with small voids, foamed at low solids loading
Epoxies, etc. black flexible epoxy	Cured with small voids, foamed at low solids loading
RTV	Cured with small voids
Loctite 2-hr epoxy	Cured
Sylgard®-184	Cured

One of the first compatible binders found was the commercially available Loctite brand 2-hour epoxy which produced properly curing fuel samples. However, the filler materials present in this epoxy (silica, calcium carbonate, etc.) would likely hurt performance of any hybrid motor using this formulation and thus alternatives were pursued. Further study revealed that Sylgard®-184 silicone elastomer cured properly with ammonia borane at low solids loadings when cured at room temperature. However, when elevated temperature cures were attempted at 140ºF, bubbles and voids were observed in the cured samples. Thus, all samples used in this study were cured at room temperature.

3.3.5 Fuel Pellet Ignition Delay Testing

Ignition delay tests performed on the prepared Sylgard®-184-AB pellets used the experimental configuration seen in Figure 5. The Sylgard-AB pellets were prepared using AB synthesized at Purdue University using the previously discussed water-promoted synthesis method [50].The AB particle size was varied for the Sylgard®-184-AB pellets to determine whether the previously observed particle size dependency on ignition delay persisted when the AB was mixed with a binder. The results of these tests can be found tabulated in Table 5. For comparison, several ignition delay tests were also performed on pressed 100% AB pellets. However, these pellets were difficult to ignite, with some requiring several drops of WFNA before ignition would occur. As this behavior made it difficult to obtain an accurate ignition delay, these results were not included here.

Table 5 Sylgard®-184-AB pellet ignition delay results

Sample type	AB particle size range (μm)	Mean ignition delay (ms)	Standard deviation (ms)	Number of tests
Sylgard®-184-AB (80% solids loading)	D<45	44	19.95	4
	150<D<212	33	26.06	3
	Unsieved*	35.4	37.22	5
		19	7.35	4

*The two numbers listed result from the inclusion (upper) and omission (lower) of a 101 ms ignition delay result for one of the unsieved AB pellets tested

Unlike the results observed for loose AB, the mean ignition delays of the Sylgard®-184-AB pellets did not show much of a trend between particle size and ignition delay, as might be expected. There was also a relatively high degree of variation in ignition delay between similar pellets, even those using AB sieved to specific particle size ranges. One possible cause for this behavior is varying amounts of binder on the surface of the different pellets. If there is less exposed AB on the surface due to there being excess Sylgard®-184 on the surface, the rate at which the reactions leading to ignition can occur would decrease.

For the Sylgard®-184-AB pellets tested, ignition was generally accompanied by an intense green flame from the borane oxidation as the pellet burns with the WFNA. After a short period (typically less than 1 second, though the exact duration varied from pellet to pellet), the flame intensity decreased significantly, likely corresponding to the pellet beginning to burn in the ambient air. A typical image sequence showing this transition is shown in Figure 12. A significant amount of condensed phase products accumulated on the surface of the pellets during the burns.

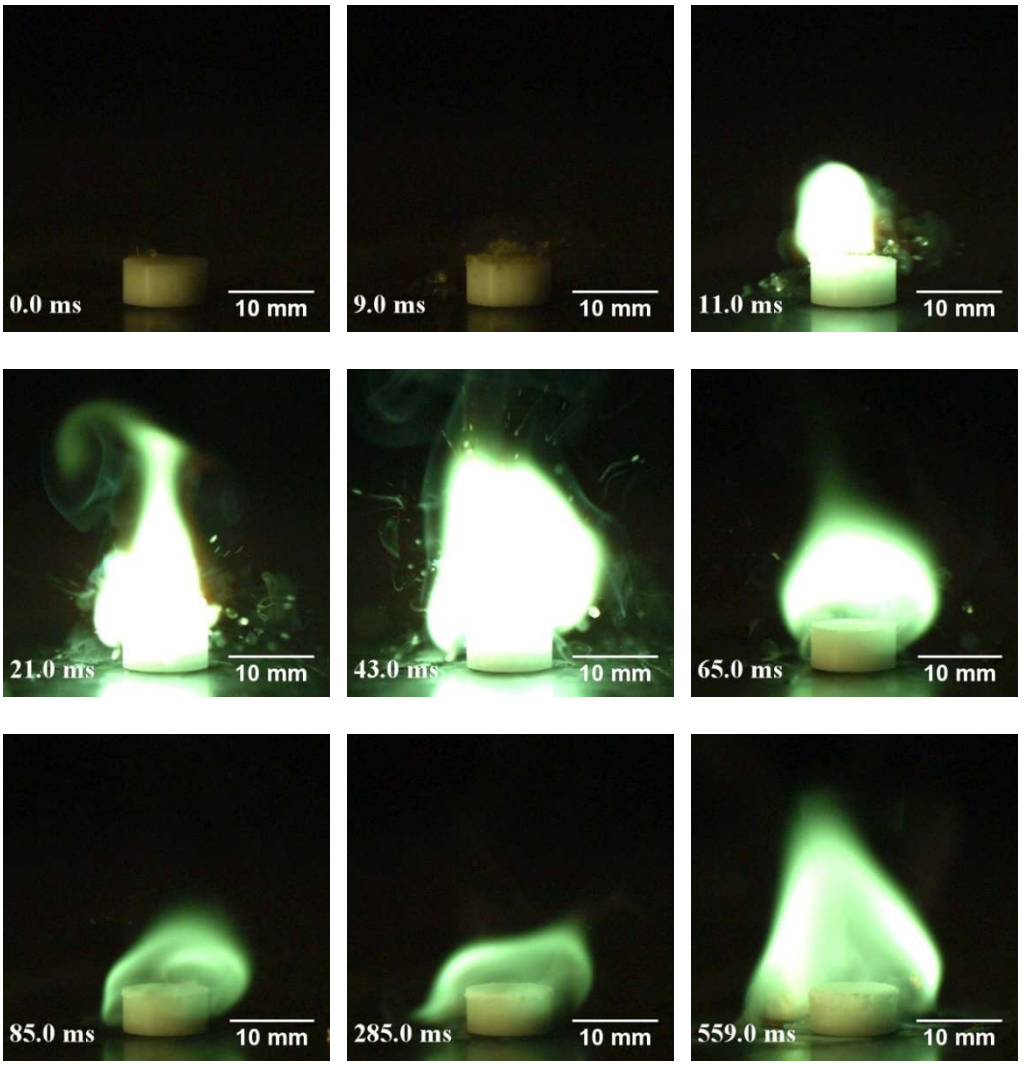

Figure 12: Image sequence of typical ignition delay test of Sylgard®-184-AB pellet with WFNA

When neat Sylgard®-184 and pressed AB pellets were burned in ambient air, both also showed condensed phase accumulation on the surface of the pellets. Given the high percentage of silicon in the Sylgard®-184 polymer, the condensed products produced on the burning Sylgard®-184 pellet is likely silicon dioxide (i.e., SiO_2, silica). In the case of the pressed AB pellets, thermochemical equilibrium calculations performed with AB and WFNA in CHEETAH 7.0 [55] thermochemical code predicted the formation of solid boron nitride (BN) which may not be adequately removed from the surface at lower pressures/oxidizer mass fluxes. This would imply

that the condensed phase products observed here was likely some combination of silica and other boron-nitrogen compounds. In a hybrid motor, this accumulation may result in reduced regression rates as the accumulated material may reduce the rate at which the oxidizer can react with fresh fuel. Earlier work published by Weismiller et al. reported high combustion efficiencies (> 90%) for paraffin-AB fuel grains tested in a small hybrid motor with gaseous oxygen for solid loadings as high as 50% [20]. However, the authors also reported condensed phase product accumulation similar to what was observed here which may have caused the reduced regression rates reported for higher AB loadings [20]. Further study would be required to determine if similar combustion efficiencies would be achievable for a Sylgard®-184-AB fuel grain (with 80% AB by mass) used in a motor configuration.

3.3.6 Theoretical Performance

The theoretical performance of ammonia borane and other commonly used hypergolic fuels with WFNA can be found in Figure 13. These results were obtained using CHEETAH 7.0 thermochemical code [55] assuming an initial chamber pressure of 68 atm and perfectly expanded to atmospheric pressure. These results assumed equilibrium conditions (i.e., the composition was allowed to change throughout the system instead of being "frozen" at a given state). As ammonia borane would require a fuel binder to be practical in a rocket system, also included is the predicted performance of an 80% ammonia borane, 20% Sylgard®-184 fuel mixture. The assumed properties of Sylgard®-184 and ammonia borane for these theoretical performance calculations can be found in Table 6. The properties for Sylgard®-184 were taken directly from the CHEETAH 7.0 library while the properties for AB were previously reported by Pfeil et al. [3].

Table 6: Intrinsic properties for fuel components used for theoretical performance calculations

Fuel component	Chemical formula	ΔH_f (cal/mol)
Sylgard®-184	$C_2H_6O_1Si_1$	-1.20E+05
Ammonia borane	NH_3BH_3	-1.60E+04

These results indicate that using ammonia borane in place of hydrazine and its derivatives in hypergolic systems could result in a net increase in specific impulse if used with WFNA. Another noteworthy trend observed here is the dual peak behavior of the ammonia borane-based fuels. Unlike the other fuels that have a single optimal oxidizer to fuel (O/F) ratio, the AB based fuels maintain high performance over a much wider range of operating conditions. Chemical equilibrium calculations performed using CHEETAH 7.0 indicate the lower O/F peak corresponds to the complete oxidation of boron leaving much of the hydrogen not oxidized, resulting in a lower average molecular weight in the exhaust products. Likewise, the higher O/F peak corresponds to the complete oxidation of both the boron and hydrogen, resulting in a higher chamber temperature. As the operating condition shifts towards higher O/F ratios, the increasing flame temperature helps to counteract the effects of the increasing average molecular weight. In the context of an actual rocket system, this could help to maintain high levels of performance during periods of varying oxidizer flow rate.

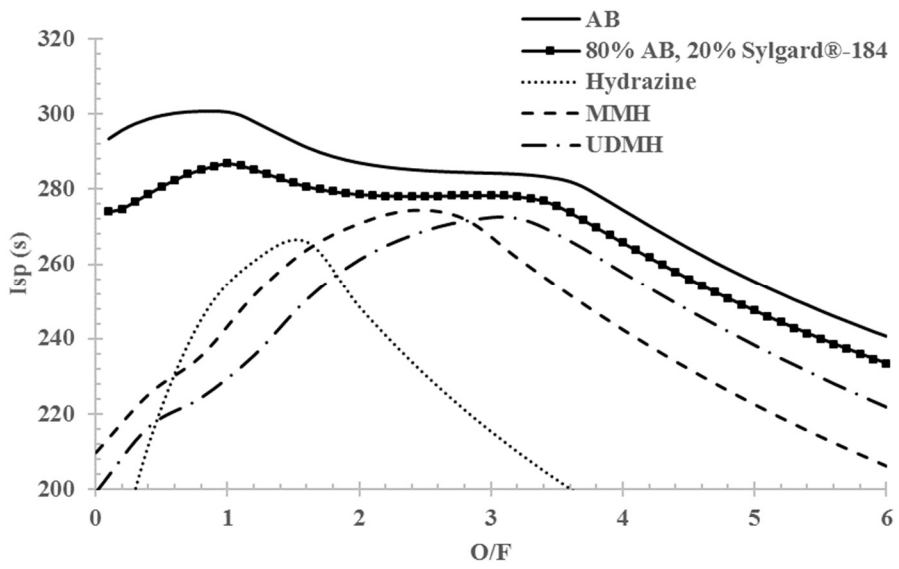

Figure 13: Theoretical performance of various hypergolic fuels with WFNA

While performing the theoretical performance calculations discussed previously, it was noted that for certain test cases (particularly the relatively fuel-rich ones), there was a relatively high percentage of condensed phase products predicted. While these products were treated the same as gaseous species when calculating the theoretical specific impulse, in a real system they would result in two-phase flow losses. As these losses cannot be estimated from thermochemical codes alone due to their non-equilibrium state, it is often necessary to obtain these estimates experimentally. The following relation was used to obtain a preliminary estimation of these losses

$$I_{sp,TPFL} = (1 - X) * I_{sp} \quad (1)$$

where $I_{sp,TPFL}$ is the estimated specific impulse when accounting for two-phase flow losses, X is the overall condensed product mass fraction, and I_{sp} is the ideal specific impulse [56].

The effects of including these losses for the 80% AB, 20% Sylgard case shown previously in Figure 13 can be seen in Figure 14. As one would expect, the condensed phase mass fractions are significant for the fuel-rich cases due to a lack of oxidizer leading to incomplete combustion. As a result, the specific impulse adjusted for two-phase flow losses decreases significantly in these regions. For the more stoichiometric and oxidizer-rich cases where the condensed phase mass fraction is lower, impact of two-phase flow losses is much less significant. In spite of this however, the performance of the AB-Sylgard system is still comparable to the other liquid hypergolic fuels (albeit for a smaller O/F range).

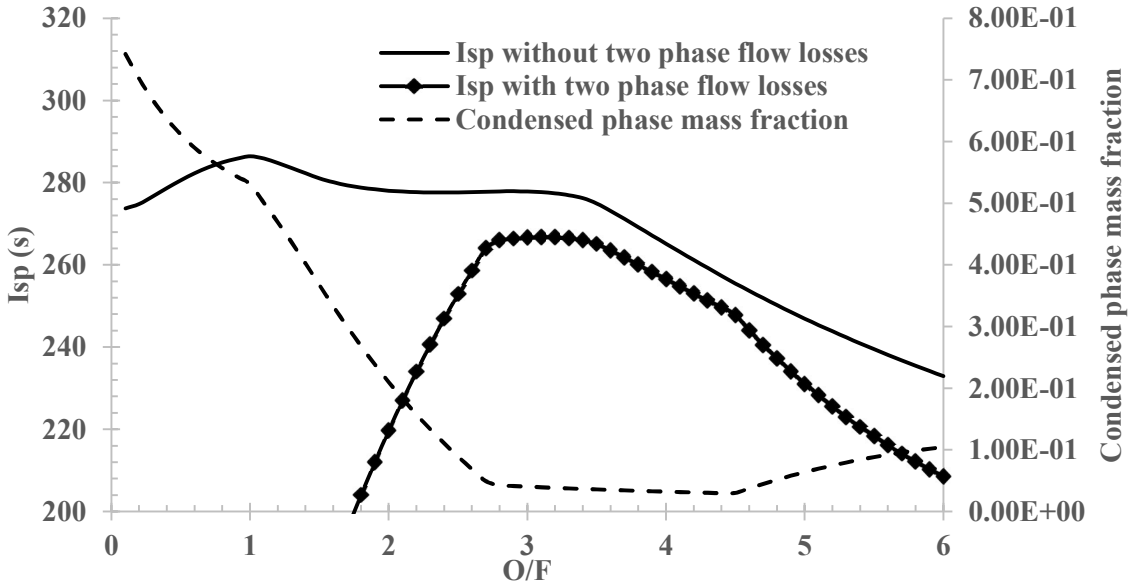

Figure 14: Estimated effects of two-phase flow losses on the theoretical performance of an 80% AB, 20% Sylgard®-184 fuel mixture with WFNA

As this approximation assumes that the condensed phase products contribute nothing to the specific impulse, it effectively serves as a worst-case estimate. In reality, the actual effects of two-phase flow losses are greatly dependent on the real-world behavior of the system in question. If any condensed agglomerates are relatively small and sufficiently accelerated by the

flow, they will contribute to the specific impulse of the rocket. Without a more informed understanding of how the AB-Sylgard fuel mixture behaves in a rocket motor, it is difficult to refine this estimate further.

3.4 Conclusions

The ignition delay of ammonia borane produced using a new high-yield scalable synthesis procedure was measured and compared with other established synthesis methods. Tests performed with WFNA resulted in comparable ignition delays for AB sieved into similar particle size ranges. Generally, the different types of ammonia borane tested all produced ignition delays shorter than 10 milliseconds with WFNA, making it potentially viable for use in hypergolic rocket systems. The development of newer, higher yield synthesis methods with the potential for larger scale production capabilities also makes AB more feasible to use in larger scale motor systems. When ignition delay tests were performed on ammonia borane powder with nitrogen tetroxide, ignition delays typically longer than 50 milliseconds were measured, likely indicating that NTO is not a suitable oxidizer for ammonia borane in a hypergolic hybrid system.

While comparing the ignition delays of ammonia borane produced using different synthesis methods, it was observed that AB purchased and used as provided by a commercial supplier produced ignition delays consistently shorter than the other AB tested. Further testing indicated that this was likely a result of a particle size dependency on the ignition delay for ammonia borane. When AB sieved into multiple particle size ranges was tested, a trend of ignition delays increasing with increasing AB particle size and vice versa was observed. For the finer AB particles tested, ignition delays as short as 0.6 milliseconds were measured, some of the shortest ever reported for a solid fuel hypergolic system.

Ignition delay tests of ammonia borane using Sylgard®-184 silicone elastomer as a fuel binder were also performed with WFNA. Unlike the earlier results obtained with loose AB powder, no clear trend was observed with respect to the ignition delay of pressed Sylgard®-184-AB pellets with different particle size ranges. These tests show that the Sylgard®-184-AB formulation may be viable for use in a hypergolic hybrid system as the mean ignition delays were less than 50 milliseconds. However, if the condensed phase product accumulation that was observed on the surface of the burning Sylgard®-184-AB samples tested here is still present when tested in a motor configuration, an alternative binder may need to be utilized in place of Sylgard®-184 to achieve high combustion efficiencies. In addition, for it to be practical for use in larger scale fuel grains at high solid loadings, the formulation must be modified to improve the mixture rheology sufficiently enough to enable cast-curing.

4. SURFACE TEMPERATURE MEASUREMENTS OF BURNING SOLID PROPELLANTS USING PHOSPHOR THERMOGRAPHY

4.1 Introduction

In the field of combustion research, there are few physical quantities as informative as temperature with regards to obtaining an improved understanding of the combustion behavior of a system. Besides being a state variable, it plays a major role in the thermochemical and heat transfer processes taking place. In the context of energetic materials (e.g., propellants, explosives, etc.), knowledge of the burning surface temperature for the material in question is often crucial in developing an understanding of its combustion behavior, including unsteady combustion. Heat feedback to the surface and thus the rate at which pyrolysis occurs is strongly influenced by the surface temperature (or, more specifically, the relationship between the surface and flame temperatures). In addition, obtaining accurate measurements for the surface temperature is often critical for validating and improving the results obtained from models for the deflagration of energetic materials, and yet these measurements are highly uncertain [57].

Surface temperature measurements are often performed using embedded thermocouples and through other less intrusive optical methods. Historically, thermocouples have been used to successfully measure the surface temperature of both homogeneous (e.g., single/double base propellants, HMX, RDX, etc.) and heterogeneous (e.g., ammonium perchlorate-based composite) propellants [58-61]. While they are often simple to implement, thermocouples are generally considered to be intrusive to the system of interest and suffer from large uncertainties, especially for surface measurements. Depending on the material used for the thermocouple, they can in some cases act as a catalyst for other unintended reactions to occur. Thermocouples are also subject to thermal lag, making them unsuitable for studying combustion phenomena where fast response

times are required. By virtue of their physical size, thermocouples have an averaging effect which can introduce additional error in situations involving thin reaction/combustion zones. Reducing the size of the thermocouple can help mitigate some of these issues, though this can introduce additional material and reliability issues.

As a less intrusive alternative to thermocouples, measurements of the infrared radiation emitted from the surface of a burning propellant can in some cases be used to optically measure surface temperatures [62-65]. From Planck's law, the spectral radiance emitted by a blackbody is dependent largely on the wavelength of light being considered as well as the temperature of the emitting body. By measuring the spectral radiance emitted in a finite wavelength range, the temperature can be obtained. For non-blackbody sources however, the spectral radiance is also dependent on the emissivity of the emitting surface, a quantity that itself is also dependent on both temperature and wavelength [66]. If information about the emissivity of the material of interest isn't available or can't be obtained experimentally, this technique cannot directly be used with confidence. If the emissivity is assumed to be relatively wavelength independent (i.e., the gray body assumption), the spectral radiance emitted then becomes roughly dependent on temperature only. For situations where this assumption is valid, the temperature of the emitting surface can be obtained by taking the ratio of the spectral radiance in two (or more) different spectral bands [66]. As the emissivity is assumed to be wavelength independent, taking the ratio of the spectral radiances will cause the emissivity terms to cancel, leaving a relation dependent on temperature only [66]. The validity of the gray body assumption typically varies with the surface conditions and material composition of the surface in question. As such, the technique can only be used to accurately measure surface temperatures with materials for which the gray body assumption is valid. In addition, infrared emission-based surface temperature measurement techniques in general

are highly susceptible to interference from soot and gas phase emissions in combustion environments [62]. If these effects aren't adequately mitigated (which may not always be possible), they can cause the measured temperature of the burning propellant surface to differ greatly from the actual temperature. This can sometimes be accomplished through careful selection of the spectral bands used for the ratio to ensure that there is not significant overlap with the higher temperature flame-based emissions.

More recently, a technique known as phosphor thermography has been receiving attention as a potential alternative to the other temperature measurement techniques commonly used when studying the combustion behavior of energetic materials. Based on the temperature-dependent luminescence properties of so-called thermographic phosphors, this technique has been well established as a semi-intrusive means to measure surface temperatures while lacking some of the shortcomings encountered with other optical techniques. The objective of this work is to apply and demonstrate phosphor thermography to measure the surface temperature of burning nitrocellulose (NC), a homogeneous solid propellant used extensively in single, double, and triple-base propellants.

4.2 Experimental Configuration

The overall experimental setup used in this study can be seen in Figure 15. For the experiments performed here, ZnO:Ga was used because of its good temperature sensitivity for the surface temperatures expected based on thermocouple data for nitrocellulose [58]. Phosphor particles were excited using the third harmonic (355nm) output of a Continuum Precision II Nd:YAG laser operating at 10 Hz. Before each test (and before each set of images recorded at each temperature during calibration), the laser power was monitored to ensure that the laser power did not vary significantly between tests. A pair of FLIR monochrome Blackfly (BFLY-U3-23S6M-C)

CMOS cameras was used to record the resulting phosphor emissions. For the working distances used here (approximately 21.6 cm), the spatial resolution of these cameras was approximately 26 μm per pixel. Syncing between the cameras and the laser system was achieved using a Stanford Research Systems model 535 delay generator. To improve the uniformity of the laser beam profile, an Edmund Optics 5-degree FWHM UV holographic diffuser was positioned as close as possible to the calibration/test sample without blocking the cameras' view of the sample.

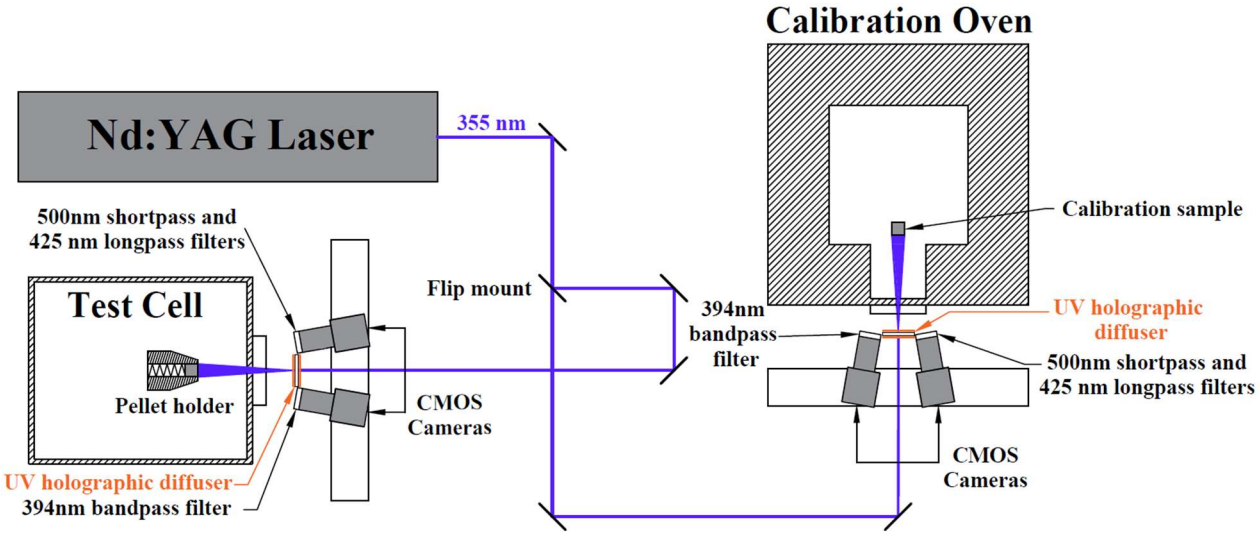

Figure 15: Experimental configuration

Following the earlier work on the zinc oxide based phosphors published by Särner et al., a 394 nm +/- 5 nm bandpass filter was used with a 425 nm longpass filter (both purchased from Edmund Optics) for the initial tests performed [42]. However, the technical limitations of the cameras used here (particularly the 50 μs minimum exposure times) caused this configuration to be susceptible to interference due to chemiluminescence from the propellant flame. As the emission lifetime of ZnO:Ga is below 1 ns, the cameras were capturing for several time durations orders of magnitude longer than necessary to capture the ZnO:Ga emission. While this did not noticeably affect the signals recorded in the 394 nm bandpass channel, the 425 nm longpass signal was affected significantly because of the excess chemiluminescence captured during the 50 μs

exposure time. The use of other cameras with better potential for time gating (i.e., intensified cameras) was not practical here due to both budgetary constraints and physical constraints associated with the test vessel used to contain the nitrocellulose combustion products. As the phosphor emissions were imaged through the same small window in the test vessel that the 355 nm laser enters, the form factor of the cameras had to be kept relatively small to prevent blocking the laser. Shifting the cameras further away from the sample (to allow larger form factor cameras to be used) would have negatively impacted the spatial resolution of the system.

Using an Ocean Optics USB2000 spectrometer, the emission spectrum of a burning 95% nitrocellulose, 5% ZnO:Ga (by mass) sample when excited with a 355 nm laser was recorded (Figure 16). As the flame emissions from the burning nitrocellulose are relatively weak below 500 nm, a 500 nm shortpass filter was added to the 425 nm longpass filter channel for subsequent experiments to filter out the majority of the chemiluminescence. As seen in Figure 17, the shortpass filter was positioned before the longpass filter to prevent the formation of an etalon due to reflections between the two filters (with regards to the chemiluminescence). With the addition of the 500 nm shortpass filter, the resulting interference due to chemiluminescence was mitigated to the point where the chemiluminescence signal was on par with the inherent camera noise.

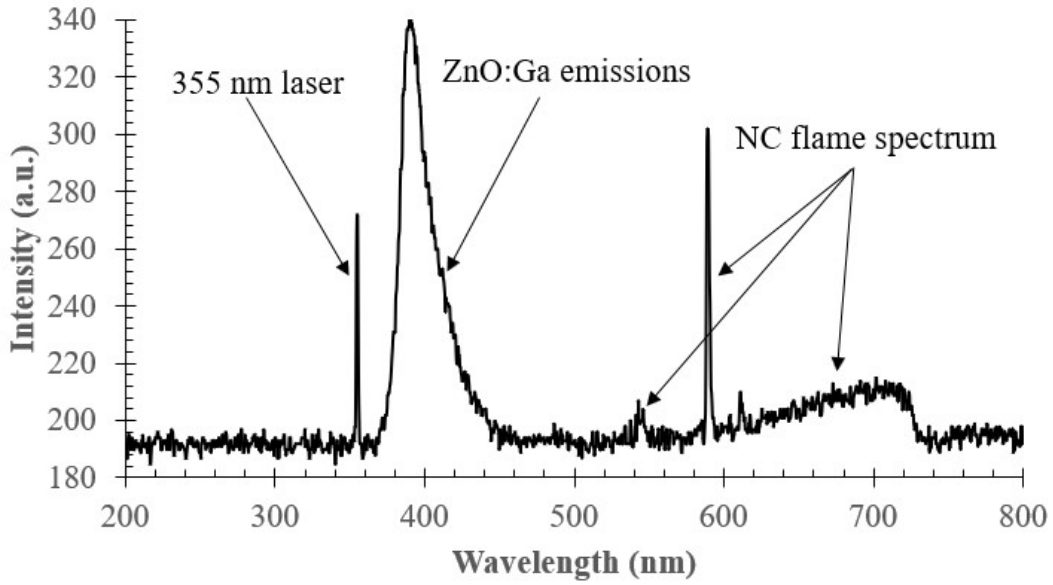

Figure 16: Emission spectrum of a 95% NC, 5% ZnO:Ga (by mass) pellet burning in nitrogen while excited by a 355 nm laser

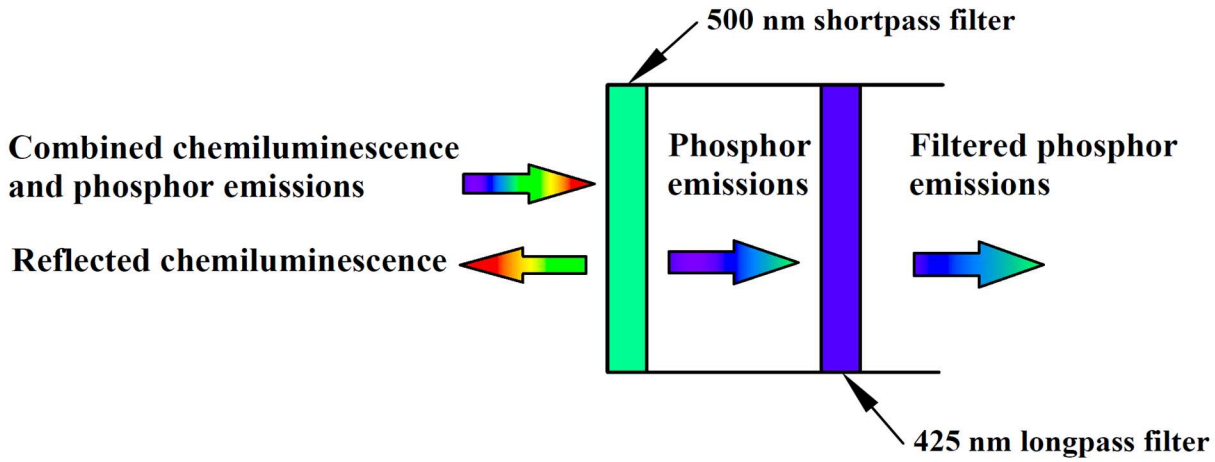

Figure 17: Arrangement of optical filters used to reduce chemiluminescence in 425 nm longpass channel

To reduce the effects of changing camera perspective and to help maintain alignment when transitioning from calibration to actual testing, the two cameras were mounted on an optics rail which was then moved between the two positions as one unit. The holographic diffuser was also mounted to this rail to make sure that the distance from the diffuser to the test sample (and thus the laser fluence) was consistent when transitioning from calibration to solid propellant testing.

After the cameras were aligned using a dot card target, minimal adjustments were made to the focus of the cameras so their object planes remained consistent. While this configuration does introduce some perspective effects (due to the different viewing angles of the cameras), the alignment of the cameras in the region of interest (i.e., the object plane/sample surface) is well maintained, reducing the impact of these effects on the resulting temperature measurements. As there was a slight difference in filter substrate thickness and index of refraction, final camera alignment was performed with the filters in place.

Post processing of the recorded images was performed using a Matlab script. The basic workflow used to convert recorded raw images to useful temperature measurements is illustrated in Figure 18. Prior to calculating the intensity ratio, a flat field correction was applied to the raw images to account for pixel-to-pixel variations on the camera sensors as well as any differences between the two cameras. The flat field correction used was,

$$\mathrm{C} = \frac{(\mathrm{R} - \mathrm{D}) * \mathrm{M}}{\mathrm{F} - \mathrm{D}}, \tag{2}$$

where R is raw image, C is the corrected image, D is a dark image (i.e., an image recorded with no light incident on the sensor), F is a flatfield image, and M is the average value of F-D for all pixels. The illumination for the flatfield image was provided using a Newport model 70677 integrating sphere that was illuminated with light in the range of 390-410nm. To account for camera noise and shot-to-shot variations, a series of approximately 500 dark and flatfield frames were recorded separately for both cameras. These frames were then averaged together to provide the dark and flatfield frames used for applying the flat field correction.

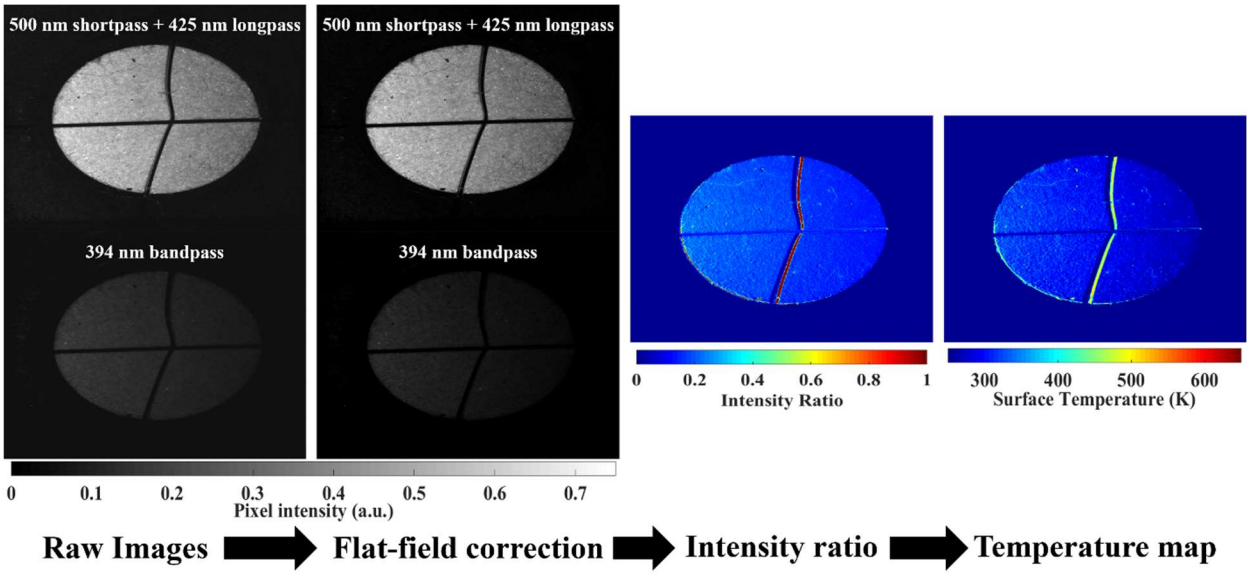

Figure 18: Post processing workflow used to convert raw images (left-most images) into useful temperature measurements (right-most image)

4.2.1 Calibration

Calibration samples were prepared using a 95% NaCl, 5% ZnO:Ga mixture and pressed into square 6x6 mm pellets using a pellet press die for 3 minutes at 10,000 psi. NaCl was used for the calibration samples instead of nitrocellulose due to safety concerns associated with the heat-sensitive nature of nitrocellulose. The surface temperature of burning nitrocellulose was estimated through embedded thermocouple measurements to be approximately 250˚C, though the NC will begin to rapidly degrade once heated to approximately 190˚C [58, 67]. As such, calibrating to 250˚C (and beyond) necessitated using an alternative calibration material better suited for the temperature range (NaCl in this case). A Mellen Microtherm box furnace with optical access ports was used to heat the calibration samples. The calibration sample was placed in the furnace and oriented so that the flat surface was perpendicular to the incoming 355nm laser and located the same distance away from the cameras as the dot card target used. For each temperature measurement, the furnace temperature was increased by approximately 15-25˚C and allowed to stabilize. After the furnace internal temperature had stabilized (as measured using an Omega

HH1384 thermocouple reader and a K-type probe thermocouple in contact with the sample), a sequence of at least 500 images were recorded using both cameras. An additional thermocouple probe identical to the one in contact with the sample was also installed in the furnace, both to compare with the sample thermocouple (to check for malfunctions) and to measure the furnace air temperature to help determine when thermal equilibrium had been reached. The calibration process continued until the recorded phosphor signal in the 394nm bandpass filter channel became too dim to measure without increasing the laser power or changing the camera settings. For the system used here, this generally occurred at approximately 635 K.

To account for changes in laser power over time, the laser power before each image set was measured and adjusted as necessary. For the tests performed here, the laser energy was held constant at 60 mJ per pulse (measured before the diffuser). After passing through the diffuser, this corresponds to a laser fluence of approximately 7.7-7.9 mJ/cm^2 at the sample located approximately 21.6 cm away from the diffuser. This laser power was chosen by systematically increasing the laser power until the room temperature phosphor signal was sufficiently strong even with the camera lens apertures closed sufficiently, to help suppress the flame chemiluminescence. It was demonstrated previously by Abram et al. that the intensity of zinc oxide based phosphors increases with laser fluence [68]. By closing the camera apertures and increasing the laser power to compensate, the interference from chemiluminescence encountered during the later solid propellant testing was reduced while keeping the recorded phosphor signal roughly constant. As Abram et al. reported that the emission spectrum and resulting intensity ratios of zinc oxide based phosphors are laser fluence dependent, this same fluence was used for both calibration and solid propellant testing [68].

The average intensity ratio for each temperature was obtained by first applying the appropriate flat field correction to the recorded raw images from each camera. The intensity ratio for each frame was then obtained by taking the ratio of the corrected combined 425 nm longpass-500 nm shortpass and 394 nm bandpass filter images (i.e., 425 nm longpass+500 nm shortpass / 394 nm bandpass). Each of the 500 frames were then averaged together to produce an average intensity ratio frame for each calibration temperature. The resulting average intensity ratio for each calibration temperature was then obtained by taking the spatial average across the surface of the calibration sample (excluding the edges where perspective effects reduced the quality of the alignment).

4.2.2 Solid propellant testing

For the testing performed here, high nitration percentage (approx. 13.3-13.5%) nitrocellulose (NC) was used. To match the phosphor concentration used during calibration, 0.75g mixtures with 95% NC, 5% ZnO:Ga by mass were prepared. These mixtures were then pressed for 3 minutes at approximately 10,000 psi to form cylindrical 1 cm diameter, 0.69 cm long pellets. Attempts to use lower concentrations of ZnO:Ga (i.e., 1% and below) resulted in non-uniform distributions of the ZnO:Ga particles throughout the pressed NC pellets as evidenced by spatial variations in the recorded phosphor emission intensity on the pellet surface. This was likely caused by poor mixing between the NC and ZnO:Ga due to the relatively low density of the NC (prior to pressing) making it difficult to adequately disperse the phosphor particles throughout the mixture. Increasing the phosphor concentration to 5% by mass resulted in greater uniformity of the recorded surface phosphor emissions. For comparison, the earlier work performed by Goss et al. (one of the few other reported instances of phosphor particles distributed volumetrically throughout a test sample) used phosphor concentrations of 12.5% by mass [44].

To keep the burning surface of the pellet stationary and in-focus relative to the cameras, a spring-loaded pellet holder was used. After loading the 1 cm diameter pellets into the pellet holder, a 30-gauge (0.254mm) tungsten wire was used to keep the front surface of the pellet flush with the front face of the pellet holder. Prior to each test, the small test cell used to contain the combustion products was filled with nitrogen to enable more direct comparisons with measurements obtained previously by Klein et al. with embedded thermocouples [58]. The pellets were ignited using a 32-gauge nichrome wire held in place on the surface using the tungsten wire and heated using an adjustable benchtop DC power supply.

4.3 Results

4.3.1 Calibration

Thermocouple data published previously by Klein et al. for 13.15% nitrated nitrocellulose plus 1 percent ethyl centralite showed surface temperatures of approximately 523 K for strands burned in nitrogen at ambient pressure [58]. Similarly, Aristora and Leipunskii reported surface temperatures of 525 +/- 48 K by estimating the amount of heat present in the surface layers of extinguished nitrocellulose [69]. In contrast, Powling and Smith reported an average surface temperature of 577 K for 12.2% nitrated NC by measuring the infrared emissions produced by the burning sample [62]. However, Powling and Smith also reported that the formation of carbonaceous products on the surface of the burning samples made it difficult to obtain surface temperature measurements for pure nitrocellulose [62]. These products may have interfered with the IR emissions produced by the burning NC, possibly resulting in the higher surface temperatures recorded.

The plot in Figure 19 shows the intensity ratio vs temperature trend obtained during the calibration process. For comparison (and to verify that the addition of the 500 nm shortpass filter

did not affect the measured intensity ratio), a second calibration was performed without the 500 nm shortpass filter. As expected, the intensity ratios with and without the 500 nm shortpass filter were almost identical until the upper limit of the calibrated temperature range (where the ZnO:Ga emissions beyond 500 nm become more significant) was reached. The relative sensitivity for this system (shown in Figure 19 as a function of temperature) was calculated from the following relation,

$$S_{rel} = \frac{1}{I_R}\frac{dI_R}{dT}, \tag{3}$$

where S_{rel} is the relative sensitivity, I_R is the measured intensity ratio, and T is temperature. The calibration data shows that for the configuration used here, the measured intensity ratio is relatively less sensitive to changes in temperature when close to room temperature (Srel=0.61 %/K). Once the temperature begins increasing however, the intensity ratio becomes increasingly sensitive to changes in temperature, with a peak sensitivity of 1.83 %/K occurring at T=523 K, after which the relative sensitivity begins decreasing. These results show that at the surface temperatures expected for burning nitrocellulose (approximately 523 K), the intensity ratio is most sensitive to changes in temperature (albeit marginally so) compared to the rest of the calibrated temperature range [58]. In any case, the reference thermocouple data for burning nitrocellulose shows that the temperature range used for calibration was appropriate.

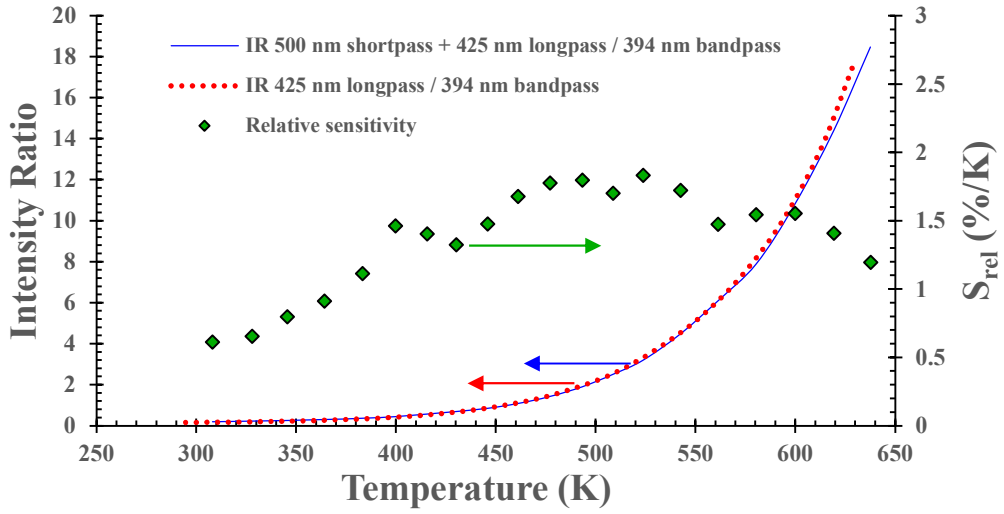

Figure 19: Intensity ratio and the relative sensitivity of the intensity ratio, during the calibration process, as a function of temperature

4.3.2 Solid propellant testing

A typical average surface temperature vs time plot obtained by taking the average surface temperature across most of the face of the pellets tested can be seen in Figure 20. The edges of the pellet were not included in these calculations as these values were more susceptible to perspective effects due to the geometry of the camera array. More specifically, the different viewing angles of the cameras caused a slight portion of the pellet side walls to be imaged. As these regions aren't imaged by both cameras, any resulting temperature measurements would be non-physical and as such were excluded. The regions near the horizontal tungsten hold-down wire and the vertical ignition wire were also not included. For the shown test, ignition occurred approximately two seconds after the ignition wire began heating the surface. Prior to this, no noticeable laser induced heating on the pellet surface was observed. Before the sample was heated by the wire, the average temperature measured across the pellet surface was approximately 296 K. This is in good agreement with the ambient room temperature at the time of testing and suggests that the intensity ratio vs temperature relation obtained during calibration was applicable despite NaCl being used

in place of NC during calibration. The initial surface heating during the pre-ignition phase due to the ignition wire can be observed by the initial increase in surface temperature prior to ignition. An image sequence corresponding to this test can be found in **Figure 21**.

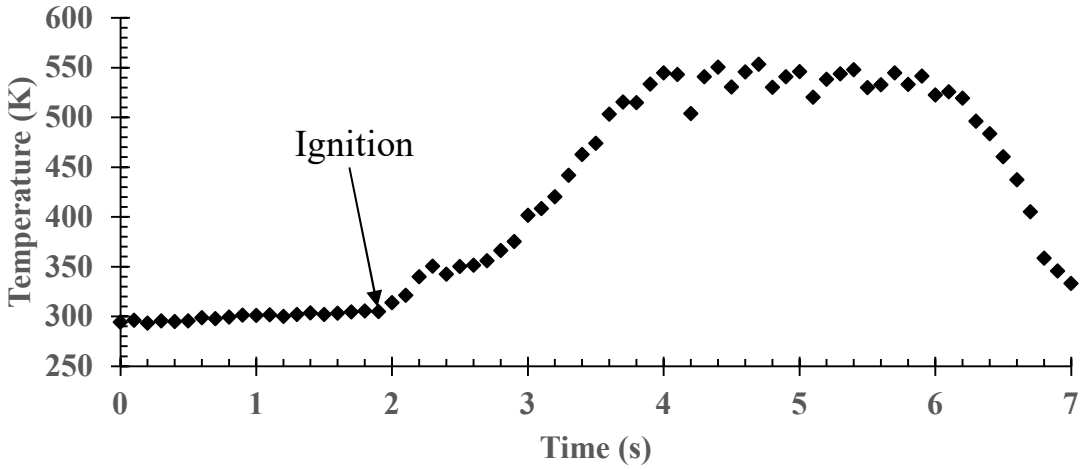

Figure 20: Average surface temperature across the entire pellet surface for representative NC pellet burning in nitrogen obtained using phosphor thermography.

By taking the time average of the previously obtained spatially averaged surface temperatures for the duration where the pellet surface is fully burning (e.g., approx. 3.7 to 6.2 seconds for the pellet shown in Figure 20), the average burning surface temperature was found to be approximately 534 K. This is in good agreement with the values expected based on thermocouple data (523 K) [58]. The slightly higher surface temperature measured here could potentially be a result of the slightly higher nitration percentage of the NC used (13.3-13.5%) in comparison to the reference data (13.15%), or errors in the thermocouple measurements in the previous work due to heat loss. As the flame temperature of nitrocellulose increases with increasing nitration percentage, one would expect the corresponding heat feedback to the surface (and thus the surface temperature) to increase as well [70]. As the pyrolysis/burning rate is

dependent on temperature, this is consistent with the higher burning rates associated with higher NC nitration percentages [57, 70].

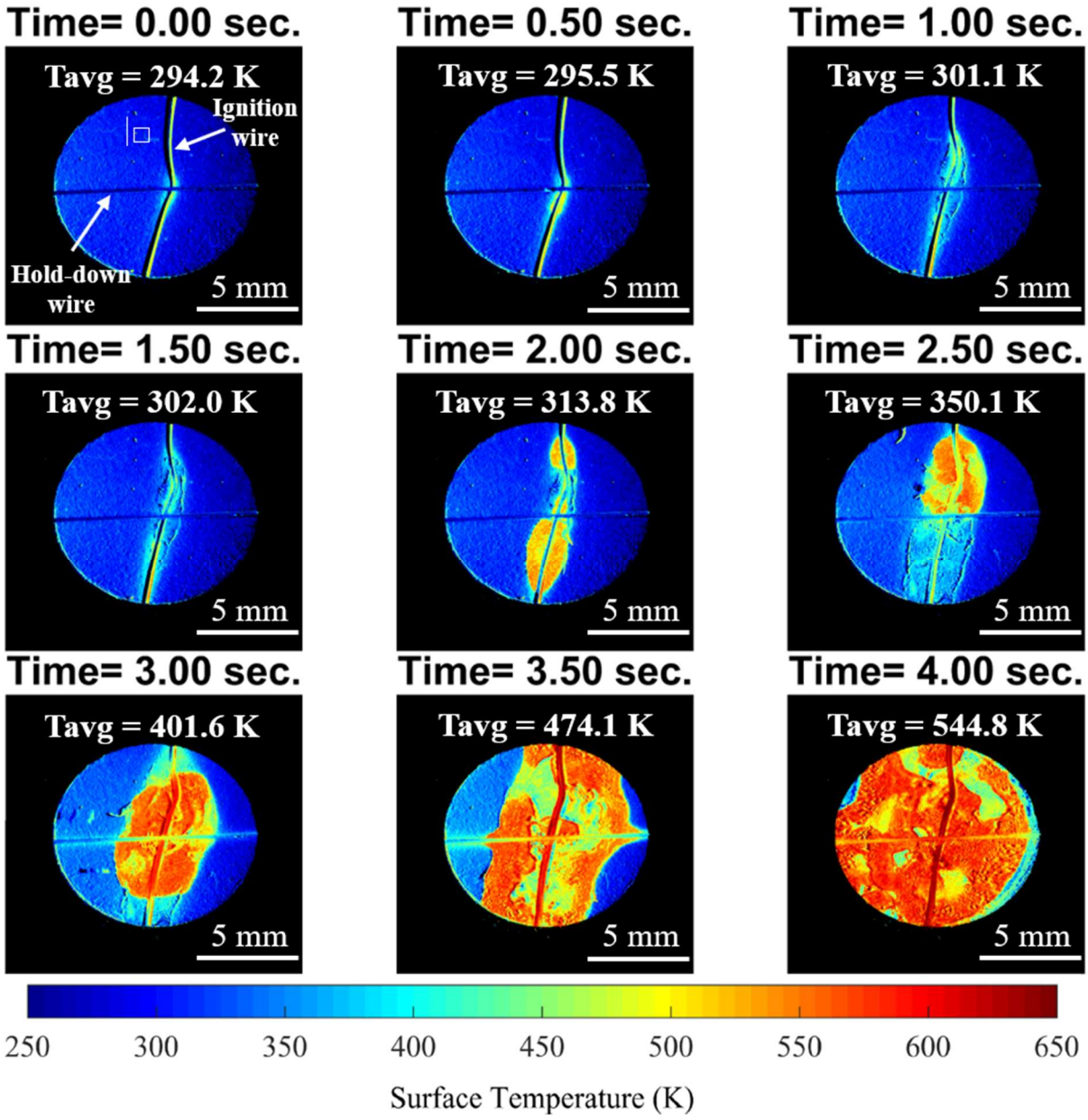

Figure 21: Image sequence showing the surface temperature of a representative nitrocellulose pellet burning in nitrogen

The NC pellets tested here exhibited locally unsteady burning behavior over the course of the pellet burns. The NC on the surface of the pellets burned off in layers, exposing the fresh

material beneath it. This behavior can be seen in Figure 21, where there are regions of relatively low surface temperatures on the surface of the fully ignited pellet corresponding to the freshly exposed material. This is likely the cause of the oscillatory behavior observed in the average surface temperature time history seen in Figure 20. This is further supported by the plot shown in Figure 22 showing the average surface temperature of a smaller region (30 x 30 pixels) on the pellet surface, specifically during the time period after ignition has occurred. This region is indicated by the white box shown in the first (time=0sec.) image in Figure 21. The error bars in this plot represent the standard deviation for the pixels within the 30x30 pixel region. As the surface temperature is averaged across a much smaller area compared to Figure 21, the degree to which the surface temperature fluctuates can be more readily estimated. When these results were compared to the raw images recording during this test, it was observed that the largest standard deviations (e.g., time=3.1 sec. in Figure 22) occur when the pellet was burning non-uniformly in the region of interest. When the pellet was burning more uniformly (e.g., time =5.1 sec. in Figure 22) in the 30x30 region, the standard deviation is much lower. The contour plot of the temperature history of a vertical strip of 50 pixels seen in Figure 23 shows this oscillatory trend more generally. The 50 pixels used for this plot are indicated by the vertical white line shown in the first image in Figure 21. As the system used here was only operating at 10 Hz, it is difficult to accurately determine the frequency of oscillation. However, the results seen in Figure 20, Figure 22, and Figure 23 seem to suggest a frequency of about 3-5 Hz. As the nitrocellulose used here had a cotton like consistency (as opposed to a granulated powder), the arrangement of the NC fibers likely varied throughout a given pellet. This would presumably affect the rate at which the different parts of the pellet burned and help explain the unsteady nature seen here.

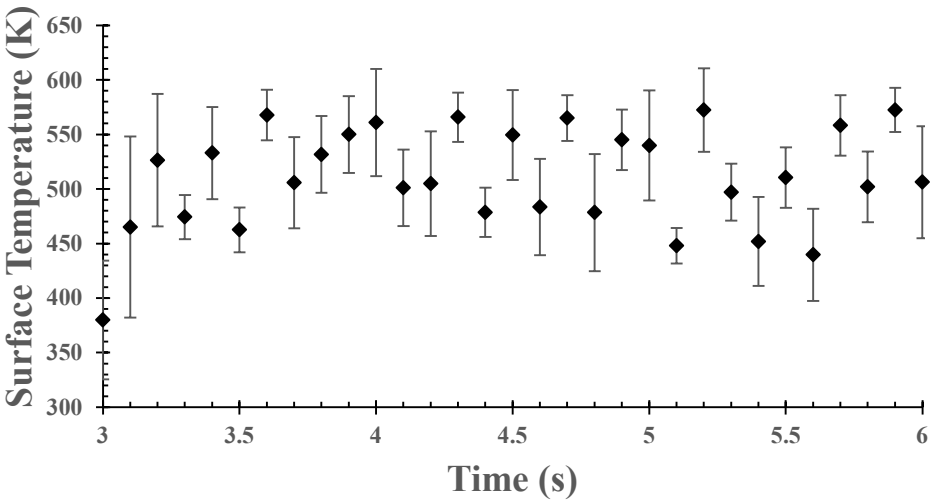

Figure 22: Average surface temperature of a region of 30x30 pixels for a burning NC pellet

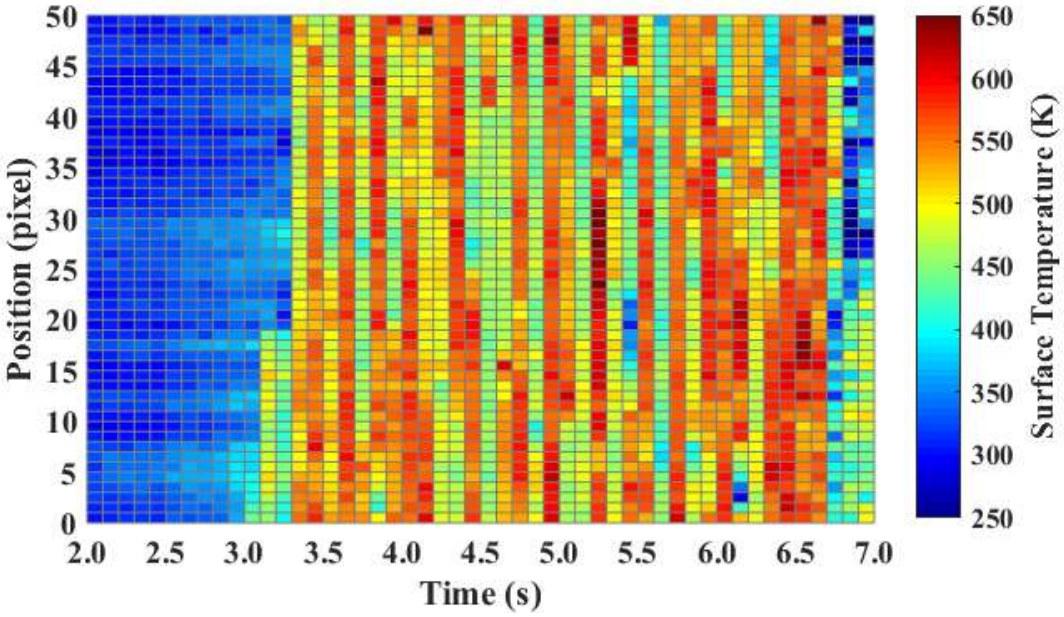

Figure 23: Temperature profile plot along a vertical line of pixels on pellet surface as shown in Figure 21

The unsteady burning observed here may also simply be a result of self-oscillatory behavior commonly observed with burning solid propellants [71]. This type of behavior has been previously reported with a variety of different types of propellants including (but not limited to) HMX, double-base propellant, and AP composite propellants [72-76]. Unlike acoustic instabilities which

are generally higher frequency in nature, self-oscillatory burning generally results in lower frequency oscillations and is directly related to the intrinsic properties of the propellant of interest [73, 76]. Following basic QSHOD (Quasi-Steady, Homogeneous, One-Dimensional) theory for solid propellant combustion, it can be shown that the characteristic frequency of a propellant surface (f_s) can be estimated from,

$$f_s = \left(\frac{E_s}{RT_s}\right)\frac{{r_b}^2}{\alpha_c} \tag{4}$$

where E_s is the activation energy of the condensed phase, R is the universal gas constant, T_s is the propellant surface temperature, r_b is the propellant burning rate, and α_c is the propellant's thermal diffusivity [77]. Using the parameters listed in Table 7 and the previous relations, the surface characteristic frequency was calculated to be 0.68 Hz. The likely cause for this relatively low frequency (compared to the 3-5 Hz observed here) is that the burning rate listed in Table 7 was an average burning rate estimated from the initial pellet length and approximate burn duration. As the pellets were relatively short in length (approx. 0.69 cm in length), there may not have been sufficient time for the burning rate to reach steady state, resulting in an inaccurate average burning rate estimate. As the characteristic surface frequency scales with the square of the burning rate, any errors in this measurement will significantly affect the calculated frequency. In any case, this calculated frequency is still on the same order of magnitude as the oscillations observed here.

Table 7: Properties used to estimate characteristic frequency of condensed phase and surface zones

Parameter	Value	Source
α_c (cm^2/s)	1.79	[78]
E_s (kcal/mol)	46.5	[79]
T_s (K)	534	Measured
r_b(mm/s)	1.67	Measured

4.3.3 Uncertainty analysis

The accuracy of the results obtained here is highly dependent on several factors including (but not limited to) the inherent accuracy of the reference thermocouples used to monitor the temperature within the calibration oven and the variations in laser fluence from pulse-to-pulse. For the standard K-type thermocouples used here, the uncertainty is within ±2.2 K or ±0.75% (whichever is greater) of the actual temperature. For the upper temperature limit of the calibration performed here (approximately 635 K), the max uncertainty due to the reference thermocouple would be approximately ±4.76 K. As discussed previously, the emissions of the various zinc oxide based phosphors are dependent on the incident laser fluence used to excite them [68]. While a consistent average laser fluence was used for both the calibration and the solid propellant testing performed, fluctuations in laser pulse energy will lead to some inherent degree of uncertainty in the temperature measurements. These effects were estimated through consideration of the measured temperature fluctuations for a sample at a steady temperature. As seen in Figure 24, for a sample at room temperature (i.e., approx. 296 K), these fluctuations were approximately ±3-4 K about the mean temperature measured across the entire sample surface during this duration. At the upper temperature limit for the performed calibration (i.e., 635 K), these fluctuations were closer to ±2 K. Taking the root sum of the squares for the uncertainties at the lower and upper limits of

the calibrated temperature range yields overall uncertainties on the accuracy of ±4.6 K and ±5.2 K respectively.

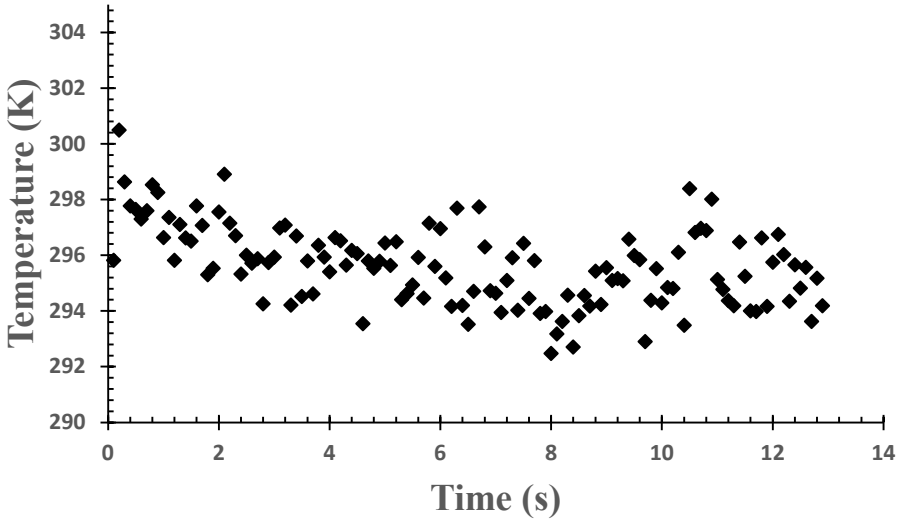

Figure 24: Surface temperature fluctuations due to pulse-to-pulse laser energy fluctuations

The precision of the system used here was estimated by determining the standard deviation in 10 arbitrarily selected regions of 5x5 pixels where the temperature was relatively uniform during a representative pellet burn. This was done both for regions close to room temperature and for those at elevated temperatures (approximately 575 K). For regions close to room temperature, the standard deviation was approximately ±5.4 K whereas for hotter regions it was approximately ±13.4 K.

4.4 Conclusion

Using a system operating at 10 Hz, the surface temperature of a burning nitrocellulose pellet was successfully measured using phosphor thermography. This is the first reported instance of phosphor thermography being used to measure the surface temperature of a burning energetic material. ZnO:Ga was selected for the work performed here as it offered good temperature

sensitivity in the temperature range of interest while also emitting at shorter wavelengths. Average surface temperatures were measured to be approximately 534 K which is in good agreement with previously published thermocouple data (approximately 523 K) [58]. The slightly higher temperatures seen here may be a result of the slightly higher nitration percentage of the nitrocellulose used (approx. 13.3-13.5%) in contrast with the 13.15% NC used for the reference thermocouple data, or from errors in the thermocouple measurements.

Preliminary efforts in using this technique were met with difficulties due to the technical limitations of the detector system used here. The flame chemiluminescence produced by the burning propellant samples caused interference with the recorded phosphor signal in the 425 nm longpass channel due to the relatively long exposure times (compared to the lifetime of ZnO:Ga). Combining a 500 nm shortpass filter with the 425 nm longpass filter previously in use was found to reduce the flame interference on the recorded phosphor emissions to the point that it was on par with the random camera noise. This enabled surface temperature measurements to be made successfully despite the low cost of the cameras used here (relative to much more expensive intensified cameras). As expected, the addition of the 500 nm shortpass filter did not noticeably affect the measured intensity ratios due to the lack of ZnO:Ga emissions at wavelengths longer than 500 nm for the temperature range considered here. These results demonstrate the importance of mitigating the effects of chemiluminescence when using phosphor thermography to measure surface temperatures through a flame, be it through time gating or through careful phosphor/filter selection.

5. HIGH-SPEED MULTI-SPECTRAL IMAGING OF THE HYPERGOLIC IGNITION OF AMMONIA BORANE

5.1 Introduction

Unlike more conventional liquid propellant combinations (e.g., liquid oxygen (LOX)-RP-1, LOX-liquid hydrogen, etc.) that require a dedicated ignition system, hypergolic propellants are uniquely capable of self-ignition upon contact between the fuel and oxidizer. Typically, systems employing these propellants will utilize a hydrazine-based fuel (e.g., monomethyl hydrazine, unsymmetrical dimethylhydrazine, etc.) with an oxidizer based on nitric acid (e.g., white/red fuming nitric acid) or nitrogen tetroxide (NTO). These commonly used hypergolic propellants have the added benefit of being easily storable without the use of cryogenic systems. Unfortunately, the more commonly used propellants are also highly toxic and require additional safety precautions for their safe handling. Considering this, there remains a strong motivation to develop alternative fuels and oxidizers for these systems to reduce the hazards associated with handling these propellants while maintaining (or improving) system performance. To date, however, few potentially viable alternatives have been developed due to a fundamental lack of understanding of the chemical kinetics and molecular structure that govern hypergolic reactions [1, 80].

First synthesized by Shore and Parry in 1955, ammonia borane (NH_3BH_3, AB) is a solid material that is stable for typical atmospheric conditions [16]. Given its relatively high hydrogen density (19.6% by mass), it has received considerable attention as a potential solid-state hydrogen storage medium [15, 17, 18]. More recently, however, AB and other amine-borane fuels (e.g., ethylenediamine bisborane, triethylamine borane, etc.) have begun receiving increased attention for potential use as alternatives to existing hypergolic fuels [3, 11, 14, 80]. AB has been shown to

be highly hypergolic with white fuming nitric acid (WFNA), with ignition delays of approximately 2-10 milliseconds being commonly reported for the neat material [3-6, 80]. Even with the addition of a fuel binder to improve the mechanical properties of prepared fuel samples, ignition delays less than 50 milliseconds are typical with WFNA (though delays in the range of 10-20 milliseconds are not uncommon) [4, 5]. Theoretical performance calculations comparing AB with the more common hydrazine-based fuels (with WFNA as the oxidizer) also predict a net gain in specific impulse across a wide range of operating conditions [3, 4]. Considering that AB is also less hazardous to handle (compared to the other hypergolic fuels commonly in use), it could potentially serve as a viable alternative to the more conventional hydrazine-based fuels. Better quantification and imaging of AB combustion is needed to understand the dynamics of the hypergolic ignition of this fuel.

To date, much of the prior work regarding AB's use as a fuel in rocket applications has primarily involved characterizing its hypergolic characteristics and, to a lesser extent, its more general use as a fuel in various propellant formulations [3-6, 8, 19, 20, 80]. However, little to no work has been published in the open literature regarding the fundamental combustion behavior of AB. As AB is the simplest fuel in the amine-borane family of fuels, obtaining a more detailed understanding of its combustion behavior would be beneficial for understanding the behavior of these fuels in general and potentially help inform future fuel formulation/synthesis efforts.

While mostly qualitative in nature, chemical/spectral imaging (i.e., imaging of specific spectral bands corresponding to emission from a known chemical species) can help provide a general understanding of assorted combustion processes. Advancements in camera technology (particularly with respect to infrared cameras) have significantly improved the temporal capabilities of this technique enabling its use for studying more dynamic combustion phenomena.

To date, this technique has been successfully utilized for studying general hydrocarbon combustion with an emphasis on internal combustion engines, but it has not been applied to study boron combustion previously [81-86]. Studies of the combustion behavior of boron particles has provided some quantitative information regarding the emission bands of boron compounds though few spectroscopic studies in the gas phase and at high temperatures have been conducted. A list of some select emission bands reported for various boron oxides can be found in Table 8. Spectroscopic studies of AB have also reported several bands occurring at 8562 nm, 4348 nm, and 3058 nm, corresponding to B-N, B-H, and N-H stretch vibrational modes respectively [87, 88]. The simplicity of AB from a molecular standpoint (containing only boron, nitrogen, and hydrogen atoms) leads to a relatively small set of major product species. Thermochemical equilibrium calculations performed for AB burning with air predict primarily N_2, H_2O (or H_2O and H_2 for more fuel rich cases) and an assortment of boron oxides, the most prominent of which being HBO_2.

Table 8: Selected boron oxides and reported emission/absorbance bands

Species	Lines (nm)	Sources
BO	367.9, 384.9, 403.7, 436.3, 461.2	[89, 90]
BO_2	452, 471, 494.1, 519.6, 545.7, 579.1	[89-91]
B_2O_2	5291.01	[92]
B_2O_3	7142.86	[93]
HBO	3510, 5503.58, 13262.60	[94, 95]
HBO_2	2702.70, 4878.05	[93, 96]

The objective of this work is to utilize simultaneous visible and mid-infrared spectral imaging to study the combustion behavior of AB for the first time. This technique was used to help characterize the behavior of AB during a hypergolic ignition process with reagent grade nitric acid,

as well as the quasi-steady case of AB burning with air. For these two cases, multi-spectral imaging of BO, BO_2, HBO_2, and the B-H stretch mode of AB was performed.

5.2 Experimental methods

5.2.1 Spectral imaging

To determine if there were any interfering species emitting in the spectral ranges used for the spectral imaging tests, the emission spectra emanating from a pressed AB pellet burning in air was measured in both the visible and mid-infrared spectral ranges. Measurements in the visible wavelength range were performed using an Ocean Optics USB2000 spectrometer. The emission spectra in the mid-infrared was obtained using an Andor Shamrock 500i-A-R-SIL spectrograph coupled to a Telops FAST M2k high-speed mid-infrared camera. For the configuration used during these tests, a diffraction grating yielding a spectral bandwidth of 1068 nm and resolution of 5.8 nm was used.

Simultaneous visible and infrared spectral imaging was performed using the camera arrangement shown in Figure 25. Imaging of HBO_2 and the B-H stretch mode emissions of AB (and potentially its decomposition products) was performed using a Telops FAST M2k high-speed camera with a 4850 nm (100 nm FWHM) and 4275 nm (75 nm FWHM) bandpass filter, respectively. For BO and BO_2, which exhibit strong emission bands in the visible wavelength range, a monochrome Phantom V2012 high speed camera was used. Selective imaging of BO and BO_2 emission was achieved using a 436 nm (10 nm FWHM) and 546 nm (10 nm FWHM) bandpass filter, respectively. An unfiltered Phantom V5.1 color camera was used to provide a point of reference to the two filtered cameras in use. Temporal syncing between the cameras was achieved using a Stanford Research Systems model 535 delay generator. To enable proper spatial alignment of the visible and infrared cameras, a custom alignment target consisting of a polished steel plate

with an array of holes drilled and filled with furnace cement was used. The relatively high emissivity of the furnace cement compared to the polished steel plate provided adequate contrast between the two for the hole pattern to be distinctly visible in the infrared after briefly heating it with a propane torch.

5.2.2 Hypergolic ignition experimental configuration

For the tests performed here, neat AB pellets prepared by pressing bulk AB powder at approximately 10,000 psi for 3 minutes in a 1 cm pellet press die were used. The AB used for this work was prepared at Purdue University using a water-promoted synthesis method [97]. A fuel binder was not used for these samples to prevent the formation of carbon containing gaseous species (as AB does not contain carbon) whose emission might interfere with the species of interest here. This was particularly important for imaging the mid-infrared emission from HBO_2 and the B-H stretch mode of AB, as the wavelengths of their emission bands overlap with those of CO and CO_2, respectively.

The hypergolic ignition drop tests were performed using the experimental configuration shown in Figure 25. For these tests, a 100 µl gastight syringe was used to dispense individual droplets of reagent grade nitric acid (70% concentration) onto an AB pellet positioned directly beneath the syringe tip. The syringe height was kept at a constant 7.62 cm for the tests performed. Attempts to use higher concentration nitric acid (i.e., WFNA) were unsuccessful due to the rapid heat release by the interactions between the AB and WFNA causing film boiling of the WFNA. This resulted in an insulating vapor layer that prevented further reactions between the oxidizer droplet and fuel surface in addition to causing the droplet to be ejected from the surface. While it is less representative of what would be used in a typical hypergolic system, the reduced reactivity of the 70% nitric acid (relative to WFNA) sufficiently slowed the rate of heat

release/gas production to enable consistent pellet ignition. A halogen work light was used to provide additional illumination of the oxidizer droplet prior to it impacting the pellet surface. A photoresistor was used with a Melles Griot HeNe laser as a break-beam sensor to trigger the cameras to begin recording when the oxidizer droplet was approximately 4.3 cm above the pellet surface.

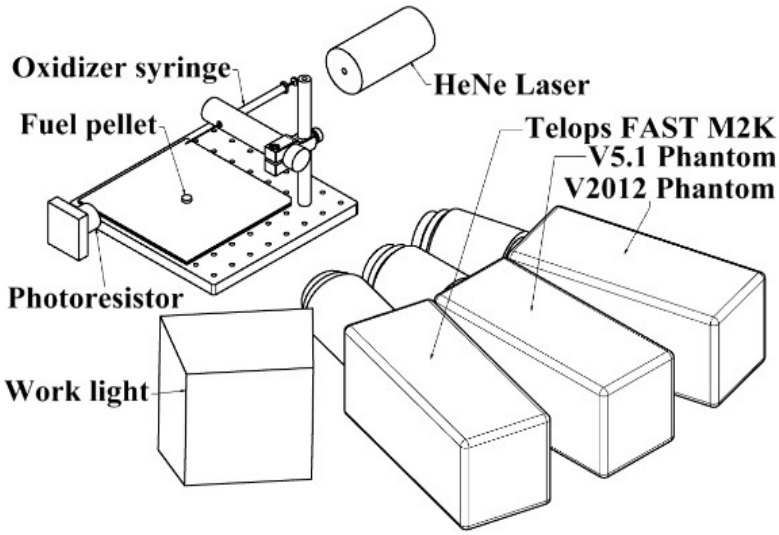

Figure 25: Experimental configuration for studying hypergolic ignition and combustion behavior of AB.

5.3 Results

The measured visible and an excerpt of the infrared emission spectra measured are shown in Figure 26. The emission recorded in the visible wavelength range consisted of several emission bands, the most prominent of which occurring at approximately 493, 518, 548, and 579 nm. These bands are consistent with what has been reported previously for studies of burning boron particles and are commonly attributed to BO_2 [89, 90]. Additionally, two relatively weak emission bands at approximately 405 and 436 nm were observed, corresponding to bands previously reported for BO [89, 90]. The 405 nm emission may also be due in part to the B-X electronic system of BO_2, however [98]. The grating used to obtain the IR emission spectra yielded a spectral bandwidth of

1068 nm, thus the flame spectra had to be obtained in intervals of 1068 nm. The spectra shown in Figure 26 was obtained with the spectrograph centered on approximately 5000 nm, roughly corresponding to the previously reported B=O stretch band of HBO_2 [93, 96]. The emission spectra in this spectral range was dominated by a strong emission feature with a peak wavelength of approximately 5000 nm. To enable comparison with the absorbance spectra of HBO_2 reported previously by Hanst et al., the emission spectra measured here and the previously reported absorbance spectra were normalized with respect to their peak emission intensity/absorbance [93]. After normalizing these results, the overall shape of the respective spectra is in good agreement, with the most significant deviation occurring at wavelengths towards the upper end of the spectral range considered (i.e., 5400+ nm). As the most sensitive spectral range of the Telops FAST M2k infrared camera used for these tests is 1.5-5.4 μm, this deviation is likely due to the decreased response of the camera at these wavelengths. In any case, these results suggest that the emission in the 4750-4950 nm wavelength range (used later in the spectral imaging tests) is produced by HBO_2. Attempts to record emission from the B-H and N-H stretch bands of AB with this configuration were unsuccessful due to absorbance by CO_2 in the ambient air and weak emission signals, respectively.

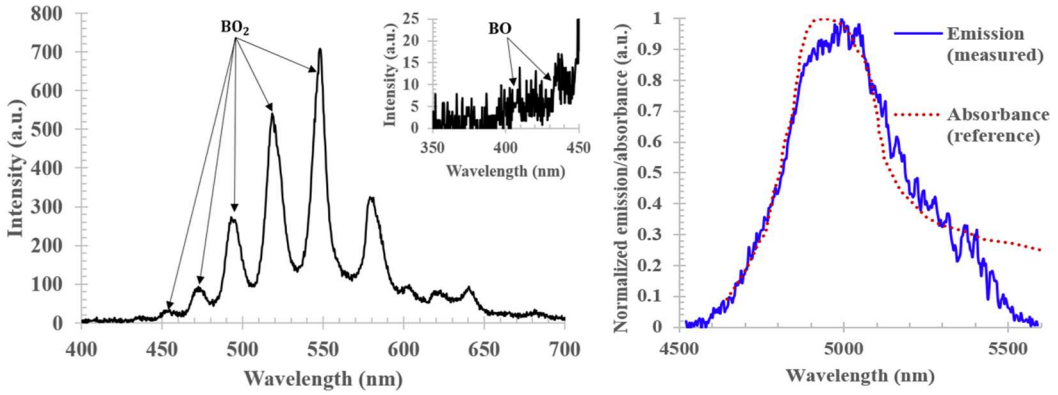

Figure 26: Measured visible (left) and infrared (right) emission spectra emanating from an AB-air diffusion flame.

During the hypergolic ignition tests, a similar ignition sequence was observed for the samples tested with a representative image sequence shown in Figure 27. After the droplet impacted and spread across the pellet surface, gas evolution was typically observed within 10-20 milliseconds of contact between the pellet surface and the nitric acid droplet. The reddish-brown gas observed at this point suggests some degree of nitric acid decomposition may be occurring as part of this process, likely through the following global reaction,

$$4\,HNO_3 \rightarrow 2H_2O + 4NO_2 + O_2, \quad (1)$$

as evidenced by the reddish-brown gas produced (NO_2). The onset of gas evolution generally resulted in most of the remaining liquid nitric acid being dispersed from the pellet surface. Ignition generally followed the onset of gas evolution within 5-8 milliseconds, with the initial ignition kernel being located on/near the pellet surface. Supplementing the visible imaging with the infrared imaging of HBO_2 (see Figure 28) demonstrates this more clearly, with distinct ignition zones being observed. Despite the reduced reactivity of the 70% nitric acid used here (compared to WFNA), the ignition delays observed were still typically in the range of 17-26 milliseconds. The ignition kernel then rapidly propagated through the gas phase, resulting in an intense (though short-lived) flame extending several centimeters beyond the pellet surface. After the excess oxidizer from the nitric acid droplet was consumed, the fuel pellets began burning with the ambient air, forming a diffusion-controlled flame.

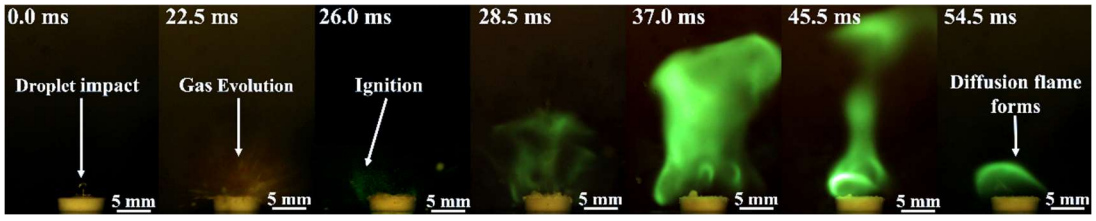

Figure 27: Representative image sequence of the hypergolic ignition of AB with reagent grade nitric acid.

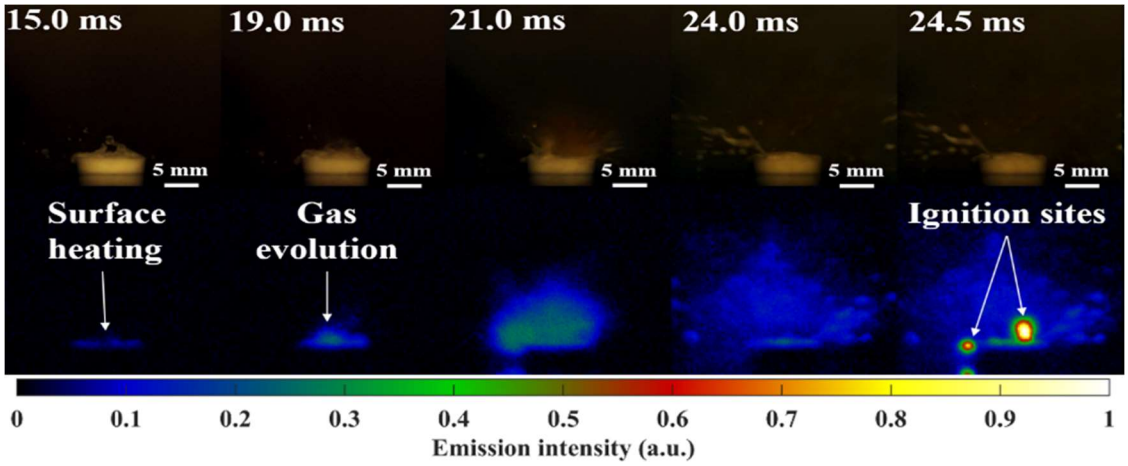

Figure 28: Simultaneous visible (unfiltered) imaging (top) and infrared imaging of HBO_2 (bottom) during the hypergolic ignition of AB.

Representative image sequence sets comparing the simultaneous emission of BO_2/HBO_2 and AB/BO during the initial ignition period can be found in Figure 29. The first image set in each sequence corresponds to the first frame with visible flame emission (i.e., "first light") recorded by the unfiltered high-speed camera. As seen in Figure 28 and Figure 29, HBO_2 emission can be observed prior to the first observed visible flame emission, with a localized rapid increase in the HBO_2 emission intensity occurring at the eventual ignition site. However, faint HBO_2 emission was observed as early as the onset of gas evolution. Studies related to boron combustion have suggested that at lower temperatures, HBO_2 will form preferentially instead of the more fully oxidized B_2O_3 [99-101]. These results may suggest that part of the heat generated by the initial reactions between the nitric acid and AB prior to ignition is due to the formation of HBO_2 at the AB-nitric acid interface. This localized heat release would then contribute to further decomposition of the AB/nitric acid, leading to the eventual evolution of gas. Once ignition has occurred and the flame begins propagating, the emission from BO and BO_2 are observed throughout the flame, with peak emission intensities occurring in the propagating flame front. The location of the peak HBO_2

emission intensity observed during this time period appears to lag slightly behind the flame front (i.e., closer to the pellet surface).

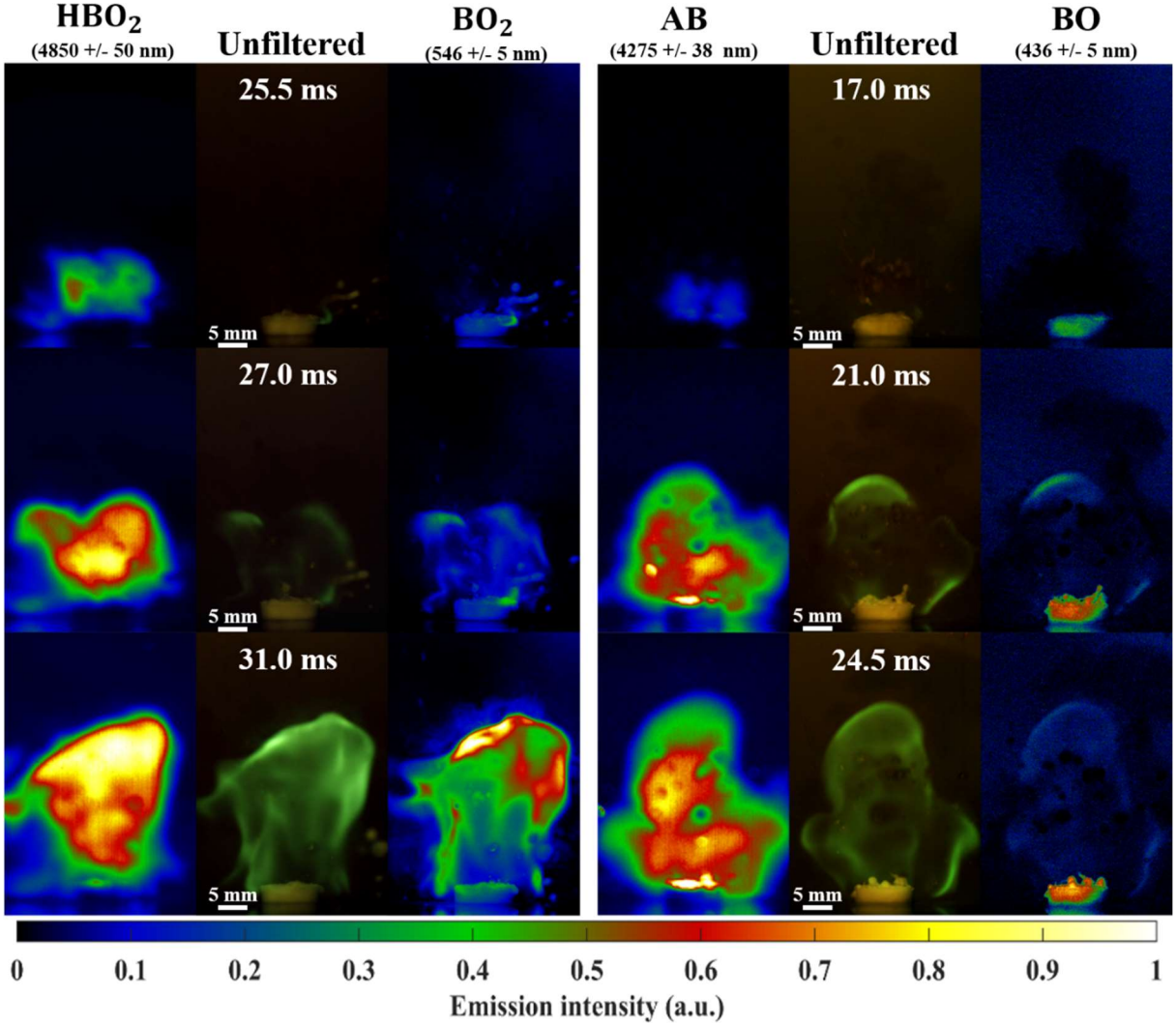

Figure 29: Representative image sequences comparing the emission intensity from HBO_2 and BO_2 (Left) and AB and BO (Right) during the hypergolic ignition of AB.

The plots shown in Figure 30 were obtained by taking the average pixel count of 5 horizontally adjacent pixels at each vertical position along the pellet center line for the filtered cameras. Since only a single filter could be used for each camera for a given test, the data shown in the plots was taken from multiple tests once the excess oxidizer had been consumed/dispersed and a relatively steady diffusion flame was observed. For the data shown in the plot, images of

BO_2 and HBO_2 emission were obtained simultaneously. This is also the case for the images of AB and BO emission. Once the flame transitioned into a diffusion-controlled flame, a thin flame front formed approximately 3-4 mm above the pellet surface with the BO/BO_2 emission being strongest within this region. As the BO band considered here is weak compared to the BO_2 band, the measured BO emission was generally of similar magnitude to the recorded background emission. Following basic diffusion flame theory, it can be assumed that the location of the flame front corresponds to the location of the maximum flame temperature/peak heat release, where the local conditions are roughly stoichiometric [102]. This may suggest that BO/BO_2 are formed primarily at higher temperatures, though further study is required to determine if the behavior observed here is simply due to the strong temperature dependence of the electronic transitions responsible for emission.

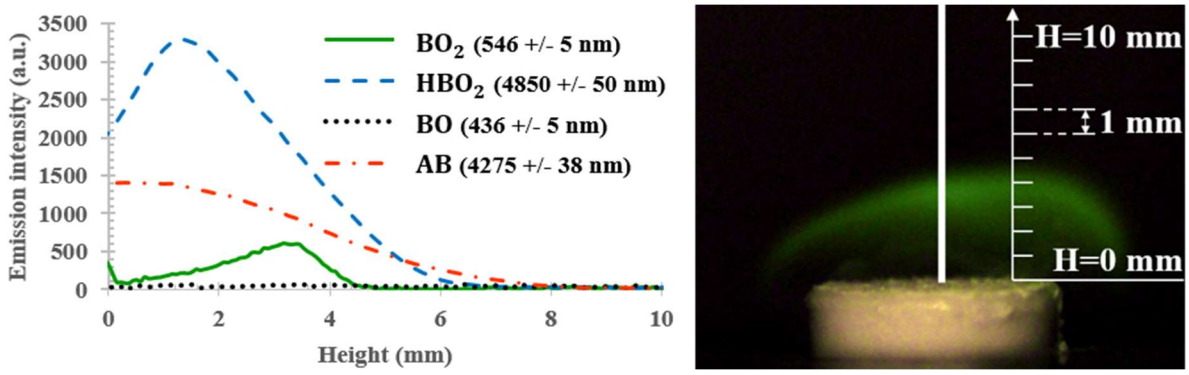

Figure 30: BO_2, HBO_2, BO, and AB emission intensities as a function of height for an AB pellet burning with air (left) and a representative image of an AB-air diffusion flame (right) with the white line representing the pixels used for the intensity profile.

The emission intensity from HBO_2 is strongest within the inner flame zone of the AB-air diffusion flame, with the peak emission intensity occurring 1-2 mm lower than the peak visible flame emissions (i.e., BO_2). The HBO_2 emission intensity then drops off gradually across the flame front until becoming too weak to measure approximately 6 mm above the pellet surface. While the decrease in emission intensity outside of the flame envelope is expected (due to the lower

temperatures within this region), the decrease prior to reaching the flame front is unexpected. Prior studies of the combustion behavior of boron (and boron-based fuels) have suggested that HBO_2 is a relatively stable combustion product, often acting as an energy trap by preventing the full energy release associated with complete oxidation of boron to B_2O_3 [99-101]. Assuming the HBO_2 produced in the inner flame zone was stable, the emission intensity would be expected to increase within the flame front, where the local gas temperature is highest. As the opposite trend is observed, this may suggest that the HBO_2 produced in the inner flame zone is being consumed to some extent, possibly to form BO_2 and other boron oxides, such as B_2O_3. This may indicate that boron combustion via boranes may proceed to more complete combustion than is typical for more conventional boron fuels. Alternatively, this may suggest the mole fraction of HBO_2 simply overshoots its equilibrium concentration initially, after which it decays to its equilibrium concentration. In any case, further study of both the flame temperature profile and the other boron oxides not considered here (e.g., B_2O_2, B_2O_3, etc.) is necessary before these explanations can be stated conclusively.

5.4 Conclusion

High speed multi-spectral imaging was successfully utilized for studying the combustion behavior of AB during a hypergolic ignition process with reagent grade nitric acid. This is the first time this technique has been applied to study boron combustion, and also it is unique in that both visible and IR multi-spectral imaging were employed together. Assorted optical filters were used to selectively image the emissions from BO, BO_2, HBO_2, and the B-H stretch mode of AB (and potentially its decomposition products). Visible imaging demonstrated that the ignition process consisted of a separate gas evolution step preceding ignition by several milliseconds. HBO_2 emission was observed as early as this initial gas evolution step, suggesting the rapid formation of

HBO_2 even at lower pre-ignition temperatures. The heat release associated with the formation of HBO_2 by the initial reactions between the AB and nitric acid may provide the energy necessary for the further decomposition of the AB and nitric acid. Once ignition occurred, the flame was observed to propagate as a seemingly premixed flame, with BO and BO_2 emissions being strongest in the propagating flame front.

Following the consumption/dissipation of the nitric acid, the flame emission intensity decreased substantially, corresponding to the AB pellets beginning to burn with the ambient air. At this point, a thin flame front formed 3-4 millimeters above the pellet surface, with the BO/BO_2 emissions occurring primarily in this narrow region. The peak HBO_2 emission occurred between the pellet surface and visible flame front, with the peak intensity occurring 1-2 millimeters below the flame front. The drop off in HBO_2 emission intensity observed within the flame zone potentially suggests some degree of conversion from HBO_2 to BO_2 and other boron oxides. This observation seems contradictory to the common understanding that HBO_2 is a stable product species, preventing the full heat release achieved through the full oxidation of boron to B_2O_3. This may indicate that boron combustion via boranes may proceed to more complete combustion than is typical for more conventional boron fuels.

6. PERFORMANCE ENHANCEMENT AND IGNITION DELAY SUPPRESSION OF TMEDA USING AMINE-BORANE ADDITIVES

6.1 Introduction

Unlike more conventional liquid propellants that require a dedicated ignition source, hypergolic propellants are uniquely capable of self-ignition upon contact between the fuel and oxidizer. Besides reducing system complexity by eliminating the need for an ignition system, these propellants can also enable reliable reignition for more complex mission profiles. Historically, most liquid rocket systems utilizing hypergolic propellants have used fuels based on hydrazine and its derivatives (e.g., monomethyl hydrazine, unsymmetrical dimethylhydrazine, etc.). While these fuels have been well characterized and offer high specific impulses, they are toxic and require special handling precautions. As such, there remains a strong motivation to develop alternative fuels that are less hazardous without sacrificing system performance. However, a lack of understanding with regards to the chemical kinetics that govern hypergolic ignition has resulted in few viable alternatives [1, 2].

Tetramethylethylenediamine (TMEDA) has been investigated as a less hazardous hypergolic fuel. Ignition delays of 15-20 milliseconds have been commonly reported for TMEDA with white fuming nitric acid (WFNA) [103-105]. Likewise, 2-N,N-dimethylaminoethylazide (DMAZ), a liquid organic azide fuel, was developed specifically to serve as a hypergolic fuel with performance characteristics comparable to monomethylhydrazine and other hydrazine-based fuels. While the predicted specific impulse for this fuel with the common hypergolic oxidizers is comparable to the more conventional fuels, the ignition delay of DMAZ with nitric acid based hypergolic oxidizers was unfortunately too long to be viable [104, 106].. While the performance of these fuels individually are insufficient to serve as viable replacements for the conventional

fuels, it has been shown that blends of TMEDA and DMAZ can result in ignition delays shorter than those found with either fuel separately [103, 104, 106]. Stevenson et al. found that fuels blend of approximately 20-40% DMAZ to 80-60% TMEDA by weight resulted in ignition delays of 9 milliseconds with WFNA, compared to 14 and 26 milliseconds for TMEDA and DMAZ alone [104].

In more recent years, amine-boranes (i.e. amine materials that have been complexed with borane adducts) have been receiving increased attention for use in propulsion applications [2, 7]. Besides their high hydrogen densities, these materials have been shown to be highly hypergolic with WFNA [2-4, 7, 11, 13, 107, 108]. Various researchers have investigated the ignition delays of a number of different amine-borane materials with WFNA to better characterize the general hypergolic behavior of this class of materials [2, 3, 7]. The authors found that for all of the 16 different amine/amine-borane materials studied, the complexation of the amine materials with the borane adducts resulted in substantial improvements in the ignition delays [2]. This is illustrated most clearly with ammonia borane (AB, the simplest amine-borane material), where the base amine (ammonia) is not hypergolic while the corresponding amine-borane showed ignition delays of 2.0 milliseconds [2, 7]. When added to ionic liquid hypergolic fuel candidates (e.g. 1-butyl-3-methylimidazolium dicyanamide (bmimDCA), 1-butyl-1-methyl pyrrolidinium dicyanamide ($Pyrr_{14}DCA$), etc.), ammonia borane, hydrazine borane, and hydrazine bisborane were shown to greatly reduce the ignition delays relative to that of the base ionic liquid [107]. Additionally, Li et al. demonstrated that the addition of triethylamine borane (TEB, a liquid amine-borane) to bmimDCA could result in ignition delays of 3-4 milliseconds with TEB mass fractions as low as 20% [109]. The objective of this work is to investigate the effects that amine-borane additives have on the ignition delay of TMEDA based fuel mixtures when tested with WFNA.

6.2 Experimental Methods

6.2.1 Fuels

For this work, the amine-boranes of interest were ammonia borane, ethylenediamine bisborane (EDBB), tetramethylethylenediamine bisborane (TMEDABB), and triethylamine borane. The AB, EDBB, and TMEDABB used here were prepared using the synthesis methods described previously [7, 11, 50]. The triethylamine borane (assay 97%), TMEDA (assay 99%), and fumed silica (0.2-0.3 μm average aggregate size) used here were purchased from Sigma-Aldrich.

For the tests performed here, the fuel formulations of interest each fell into one of three categories: 1) saturated solutions with solid amine-boranes, 2) physical mixtures of TMEDA and TEB (the only liquid amine-borane under consideration), and 3) gelled TMEDA-based fuel mixtures with excess solid amine-boranes (i.e., beyond the saturation limit). The preparation method varied slightly depending on the fuel type. In general, the assorted fuel mixtures used here were prepared by first massing out the respective assorted fuel components into 20 ml glass vials, after which the mixtures were briefly mixed by hand. Following this initial hand mix, the fuel mixtures were mixed further using a Fisher Scientific analog vortex mixer (model no. 02-215-365) for approximately 1 minute to disperse any additives (e.g., amine-boranes, fumed silica, etc.) within the TMEDA. For the physical mixtures of TMEDA and TEB, no further action was necessary to prepare the fuel blends.

For the saturated fuel mixtures, after the solid amine-boranes were adequately dispersed throughout the TMEDA, these fuel mixtures were set aside for approximately 12 hours to allow the amine-boranes to dissolve. If the solid particulates fully dissolved during this time, further amounts of the amine-boranes were added. This process was repeated until excess solid

particulates remained after several hours. At this time, the mixtures were then filtered through a 0.45 μm syringe filter to remove any remaining solid particulates, resulting in clear, particulate-free solutions.

For the gelled fuels, after mixing and dispersing the solid additives within the TMEDA, the fuel mixtures were gelled by partially submerging the fuel vials in a Cole-Parmer 8890 ultrasonic cleaning bath for 5 minutes. For the solid amine-boranes under consideration, gelled fuel mixtures with 5%, 10%, and 15% amine-borane loadings (by weight) were prepared according to the formulations listed in Table 9. Additive loadings beyond 15% were impractical for use due to the mixtures being too viscous to mix properly using the method used here. Additionally, a baseline TMEDA gel (i.e., with no added amine-borane materials) was also tested to help determine what effects (if any) the gelling process has on the ignition delays. To help maintain relatively consistent gel properties as solid loading increased, the TMEDA-fumed silica ratio was maintained at 19:1 for each of the gel mixtures. Representative samples of the baseline TMEDA gel as well as a representative example of the various gelled fuels with solid amine-borane additives are shown in Figure 31. As seen in Figure 31, the consistency of these fuels once fully set was that of a stiff gel when not subjected to an external stimulus, enabling the suspension of solid particles. When subjected to a shearing force, the gelled fuel mixtures became relatively free flowing, demonstrating the shear-thinning behavior of these materials.

Table 9: Fuel formulations used to prepare the TMEDA-based gelled fuels with solid amine-borane additives.

Fuel component	Weight percentages (%)		
TMEDA	90.25	85.5	80.75
Fumed silica	4.75	4.5	4.25
Additive	5	10	15

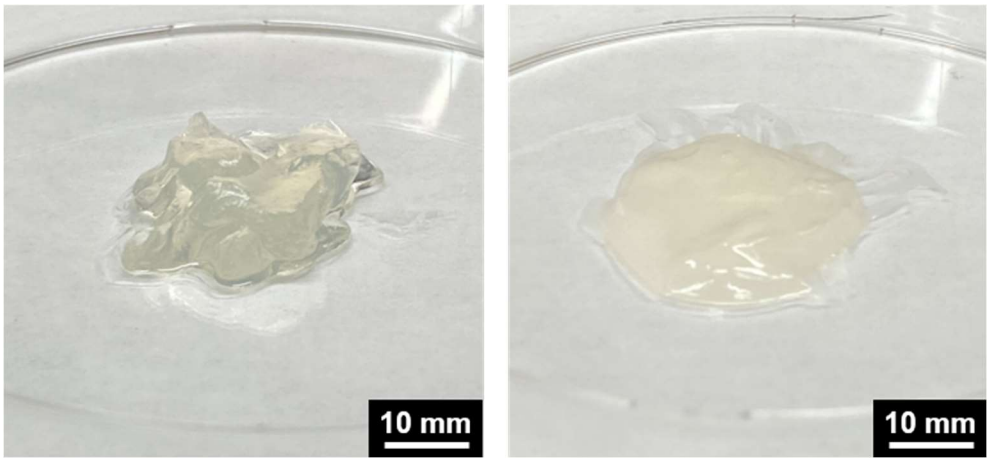

Figure 31: Representative baseline TMEDA gel sample (left) and gelled fuel sample with 15% TMEDABB by mass (right).

6.2.2 Ignition delay

The ignition delay of the fuel mixtures of interest was investigated using the hypergolic ignition drop test apparatus shown in Figure 32. Prior to each test, the fuel mixtures were loaded into square (12.7 mm by 12.7 mm) acrylic cuvettes and the sample mass recorded to improve the test-to-test consistency. The 99% WFNA used for these tests was purchased from Sigma-Aldrich and dispensed using a gastight 100 μL syringe positioned horizontally approximately 12.7 cm above the fuel. The purity of the WFNA was maintained for each set of tests by transferring the WFNA from its original container into smaller glass vials under an argon environment, with each vial being used for a single set of tests [108]. The ignition delay tests were recorded using a high-

speed V5 color phantom camera operating at 2500 frames per second. A pair of halogen work-lights was used to provide additional illumination of the falling oxidizer droplet prior to it impacting the fuel sample. The ignition delay for each test was defined as the amount of time that passed between the initial contact between the fuel and oxidizer to the first visible flame emissions. This is illustrated for a representative ignition delay test with triethylamine borane and WFNA in Figure 33.

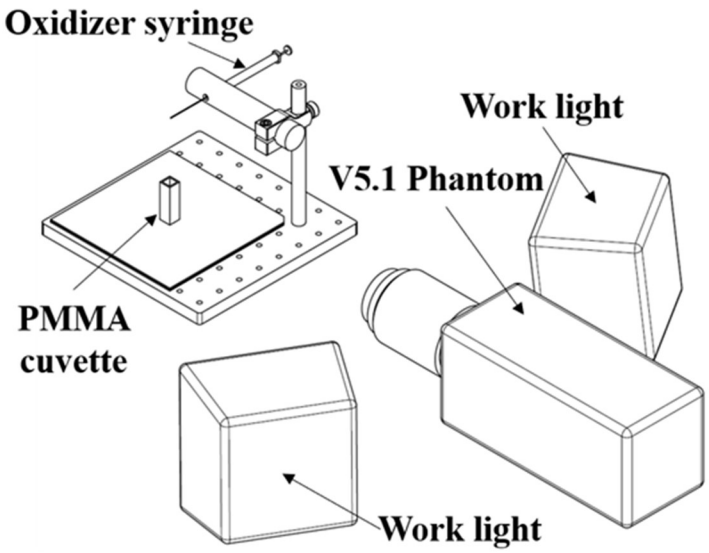

Figure 32: Hypergolic ignition drop test experimental configuration

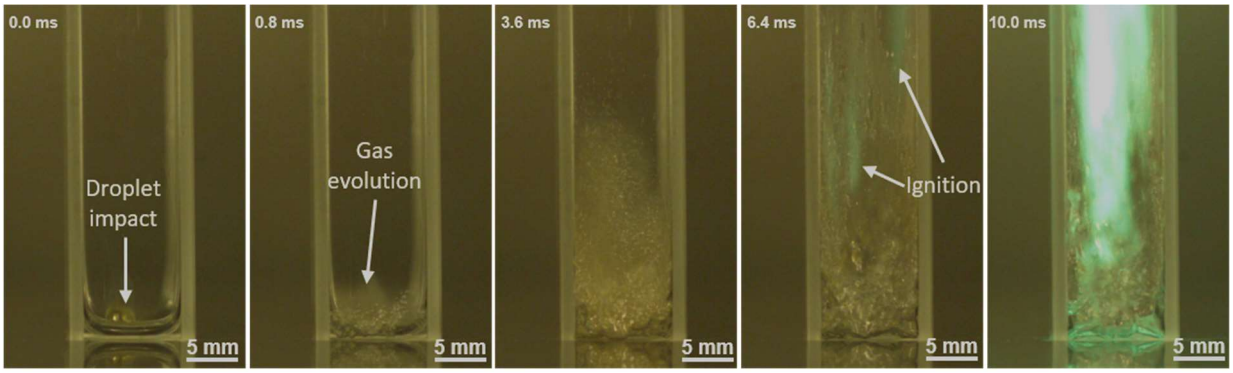

Figure 33: Representative ignition delay test between triethylamine borane and WFNA

6.3 Results and analysis

6.3.1 Saturated fuel solutions

Given the increased complexity inherent to a gelled fuel formulation (with regards to propellant processing/loading/feed systems), a series of ignition delay tests was performed with saturated solutions of AB, EDBB, and TMEDABB in TMEDA. If the impacts of these fuels on the ignition delay are significant even at low dissolved mass fractions, these saturated solutions could be used directly in conventional liquid bipropellant systems.

The results of the hypergolic ignition delay experiments with the TMEDA-based saturated fuel solutions are listed in Table 10. Also included are the approximate solubility limits for each of the three additives in TMEDA. For these fuel mixtures, the addition of the AB, EDBB, and TMEDABB resulted in the ignition delay for these mixtures decreasing significantly relatively to TMEDA. The addition of these materials in general also seemed to increase the overall flame intensity following ignition as shown in Figure 34. Of the three materials tested, TMEDABB and AB resulted in the largest improvements to the mean ignition delays (51.2% and 50.8% reduction respectively) while EDBB was slightly less beneficial (43% reduction). This similarity in mean ignition delays is particularly noteworthy given that the typical ignition delays that have been reported previously for AB and EDBB (approximately 2.0 and 2.9 ms respectively) are much shorter than have been reported for TMEDABB (approximately 26.2 ms) [3, 4, 11].

Table 10: Estimated additive solubility limits (weight percentages) and ignition delay results for saturated solutions with dissolved solid amine boranes in TMEDA.

Fuel type	Estimated solubility limits (wt. %)	Mean ignition delay (ms)	Standard deviation (ms)	Number of tests
TMEDA	N/A	20.34	4.24	7
TMEDA-TMEDABB	10-12	9.93	1.72	6
TMEDA-AB	1-3	10.00	1.57	4
TMEDA-EDBB	1-3	11.60	1.99	4

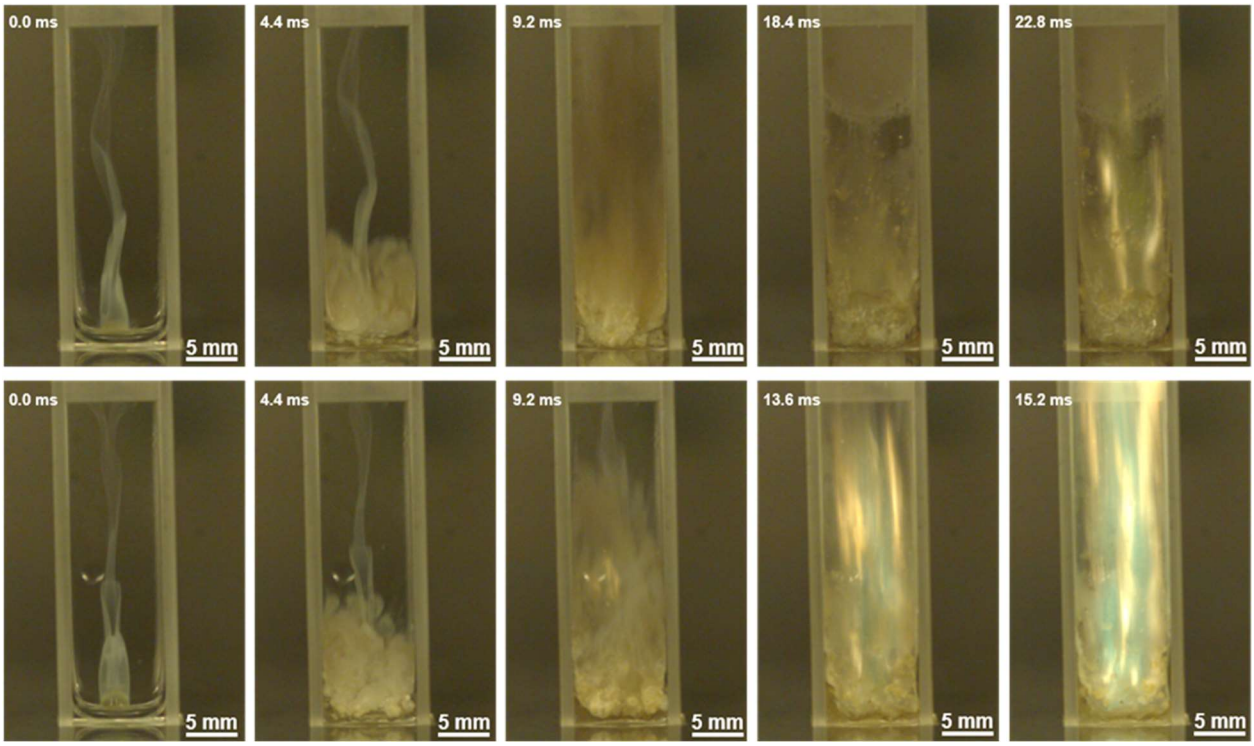

Figure 34: Representative image sequences comparing hypergolic ignition of TMEDA (top) with the saturated TMEDA-AB fuel solution (bottom) with WFNA.

6.3.2 TMEDA-TEB fuel blends

Unlike AB, EDBB, and TMEDABB, which are solid amine-boranes, TEB is a liquid amine-borane material. Earlier studies of the hypergolic nature of TEB with WFNA have reported

ignition delays rivaling that of the more conventional hydrazine-based fuels, with ignition delays of approximately 3-4 milliseconds being typical [13, 109]. As discussed previously, fuel mixtures of TMEDA and DMAZ (both liquid hypergolic fuels) have been shown to result in ignition delays shorter than either fuel individually [104]. As both TMEDA and TEB are liquid fuels, they could potentially be used in a wide variety of relative weight ratios without encountering the rheological issues inherent to the gelled fuels with high solid wt. fractions. This would potentially enable the hypergolic performance of these fuel mixtures to be optimized for a given application.

The ignition delay results for TMEDA-TEB based fuel blends as a function of the relative fuel weight fractions are shown in Figure 35. In addition to neat fuel samples of TMEDA and TEB, fuel blends of 80-20, 60-40, 40-60, and 20-80 TMEDA-TEB (by mass) were tested. As shown in the plot, the addition of 20% TEB by mass resulted in the mean ignition delay decreasing by approximately 6-7 milliseconds. Beyond this weight percentage however, the ignition delay appeared to be relatively insensitive to the addition of further TEB until the 60% TEB weight percentage is achieved. At this point, a further decrease in ignition delay was observed, with the mean ignition delays for the 20-80 TMEDA-TEB fuel mixture being shorter than that of TEB itself. This behavior is roughly consistent with the earlier results reported by Stevenson et al. for fuel blends of TMEDA and DMAZ, where the ignition delay of particular fuel mixtures could result in ignition delays shorter than expected for either of the individual fuel constituents [104].

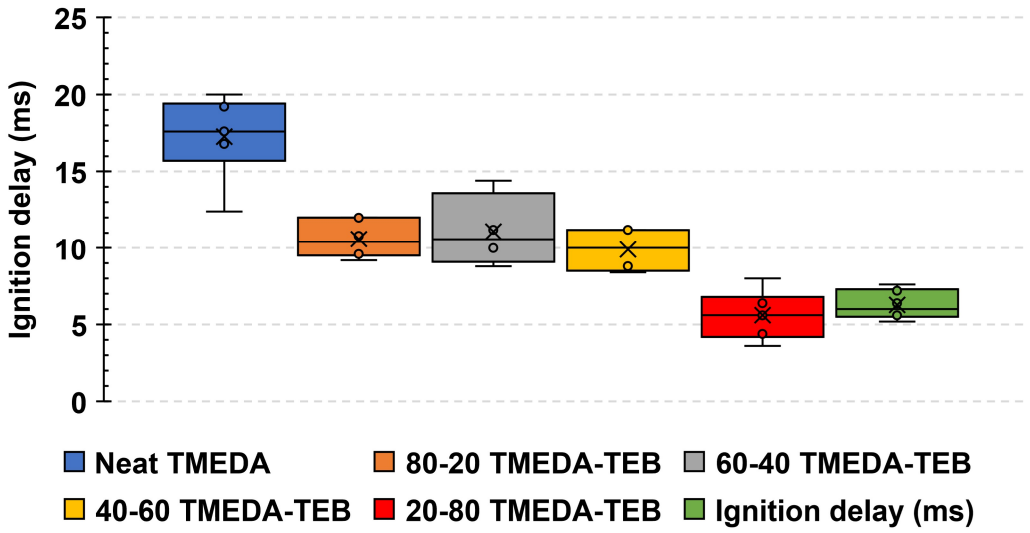

Figure 35: Ignition delay results for varying weight ratios of TMEDA-TEB with WFNA.

While performing the ignition delay experiments with the TMEDA-TEB based fuel mixtures, it was observed that over time, the color and consistency of the mixtures transitioned from a colorless/pale yellow liquid to an opaque/cloudy white slurry like consistency. This behavior was most prominent for mixtures with roughly 1:1 TMEDA:TEB by mass (e.g., 60-40 and 40-60 TMEDA-TEB), where in some cases the mixtures would crystalize within 30 minutes of mixing. Gently stirring the crystalized mixtures with a stainless-steel spatula in some cases would return the material to a more fluid state though this was generally short-lived. For relatively TMEDA/TEB rich mixtures, the onset of this behavior was more delayed, with these mixtures remaining free flowing for several hours after mixing.

Briefly heating the fuel mixtures to approximately 60-70 °C caused the remaining liquid constituents to evaporate, leaving behind a white solid material. Hydrogen, carbon, and boron NMR analysis of this solid material resulted in the shifts listed in Table 11. Comparing the obtained NMR spectra to previously published results published previously by Chitsaz et al. suggested that

the white solid formed was most likely TMEDABB [110]. This indicates that a trans-borylation reaction occurred between the TMEDA and TEB, resulting in TMEDABB and triethylamine. As such, while the hypergolic performance of the TMEDA-TEB mixtures was competitive with the more conventional hydrazine-based hypergolic fuels, the ready formation of TMEDABB suggests that TMEDA and TEB based fuel blends are likely unsuitable for practical use.

Table 11: NMR spectral shifts measured during analysis of white solid produced by reaction between TMEDA and TEB.

	Shifts (ppm)		
1H NMR	**0.97-2.14 (1.52)**	**2.65 (2.59)**	**3.16 (3.11)**
13C NMR	**52.89 (53.2)**	**58.91 (59.3)**	
11B NMR	**-11.06 (-10.0)**		

Values listed in ( ) are reference values published previously by Chitsaz et al. [110] for TMEDABB

6.3.3 TMEDA-based gelled fuel mixtures

The results obtained for the ignition delay testing performed with the assorted TMEDA based gels are summarized in entries A, B, and C of Figure 37 with the mean ignition delays for each mixture summarized in entry D. Included for reference in these plots are the ignition delay results obtained for neat TMEDA as well as the saturated TMEDA solution for each additive. In general, compared to the neat TMEDA and saturated TMEDA solutions, the gelled fuels showed a higher degree of test-to-test variation in ignition delays. This is most likely due to the fuel pool and oxidizer droplet mixing less readily/consistently due to the increased viscosity of the gelled fuels. This behavior is illustrated in Figure 36, comparing the mixing behavior of TMEDA and gelled TMEDA upon contact with the WFNA droplet. As the drop test experimental configuration

does not fully reflect the injection/mixing dynamics present in actual liquid bipropellant rockets however, these mixing issues would likely be less prominent in a more realistic system.

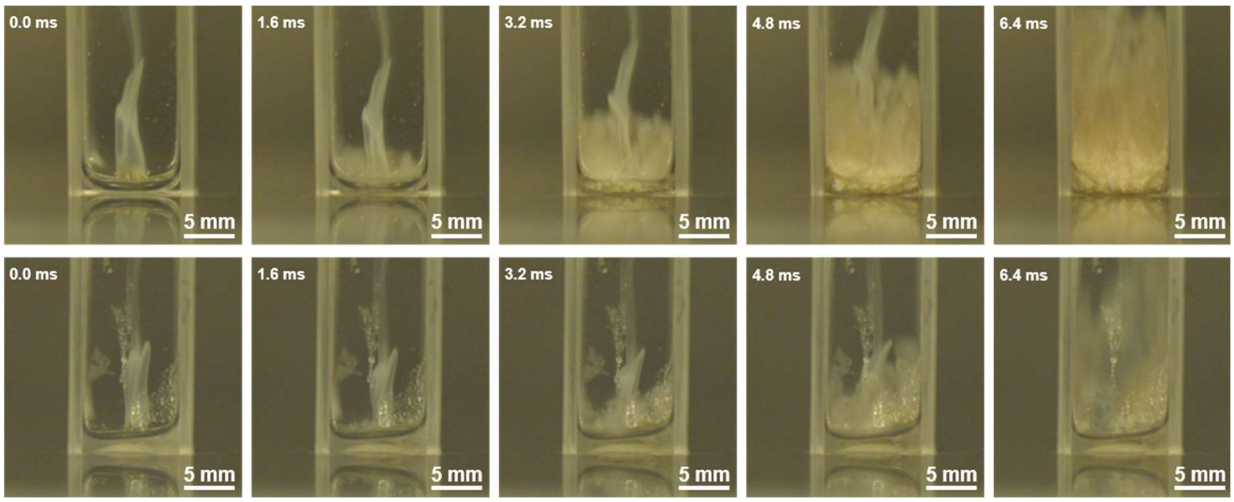

Figure 36: Representative image sequences demonstrating the differences in mixing behavior between the WFNA droplet and TMEDA (top) and gelled TMEDA (bottom)

For the gelled fuel mixtures with AB and EDBB, the shortest mean ignition delays were obtained for the 5% additive wt. percentage samples. Beyond this weight loading however, the mean ignition delays began to increase, with the ignition delays for the 15% wt. percentage samples in some cases being significantly longer than that of TMEDA itself. The TMEDABB fuels seemed to contradict this behavior however, with the longest ignition delays occurring for the 5% wt. percentage case. Increasing the TMEDABB weight percentage to 10% and 15% improved the ignition delays further, with the ignition delay for certain samples being shorter than those of the saturated fuel solutions discussed previously. Given the higher solubility limit for TMEDABB in TMEDA compared to AB and EDBB, this may suggest that the addition of these materials reduces the ignition delays until the solubility limit is reached. If the excess (i.e., non-dissolved) solid particles do not react sufficiently on the relevant time-scales, they may serve as thermal sinks, effectively slowing the rate at which the system temperature increases and, consequently, slowing

the rate at which ignition occurs. These effects would likely be further exacerbated by the mixing issues resulting from the higher fuel viscosities inherent to these gelled fuels.

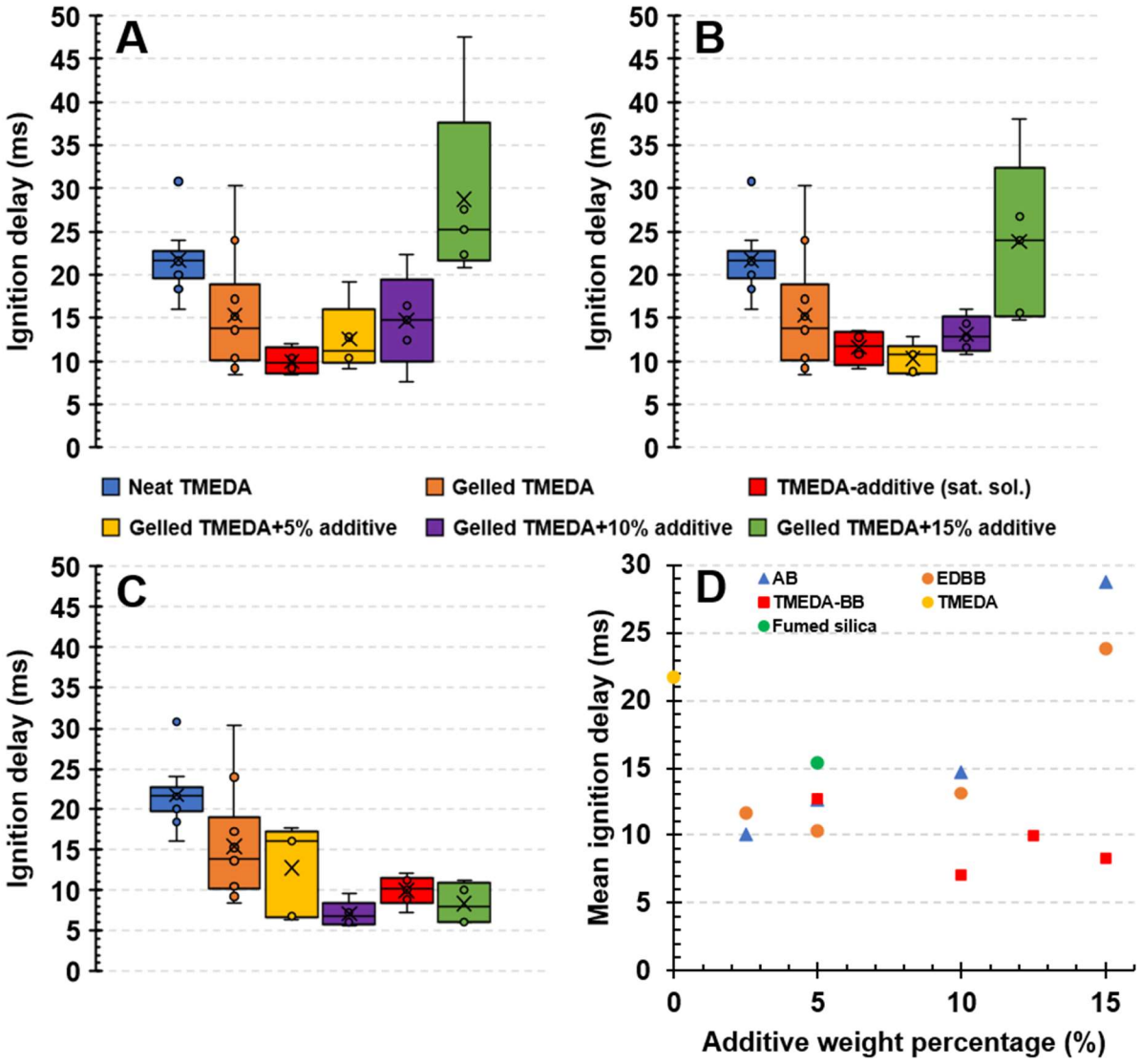

Figure 37: Ignition delay results for gelled TMEDA fuel mixtures with AB (A), EDBB (B), and TMEDABB (C) additives. The mean ignition delays for each of the gelled fuel mixtures are summarized in entry D.

6.3.4 Theoretical performance

The theoretical performance for some of the fuels/fuel blends of interest with WFNA were investigated using NASA CEA thermochemical code [111, 112]. For these calculations, a chamber pressure of 68 atm with perfect expansion to atmospheric pressure and "equilibrium" conditions were assumed. The relevant intrinsic properties for the various fuels considered here can be found in Table 12.

Table 12: Intrinsic properties of reactants used for thermochemical equilibrium calculations

Material	Density (g/cc)	ΔH_f (kJ/mol)	Chemical formula	Source
Tetramethylethylenediamine (TMEDA)	0.775	2.5104	$C_6H_{16}N_2$	[113]
Ammonia borane (AB)	0.7799	-66.9	$N_1B_1H_6$	[3]
Ethylenediamine bisborane (EDBB)	0.8317	-145.9	$C_2H_{14}B_2N_2$	[3]
Tetramethylethylenediamine bisborane (TMEDABB)	0.930	-100.0	$C_6H_{22}B_2N_2$	[106]
Triethylamine borane (TEB)	0.777	-198.6	$C_6H_{18}B_1N_1$	[109]
Fumed Silica (FS)	2.2	-910.69	SiO_2	[6]
White Fuming Nitric Acid (WFNA)	1.503	-173.013	HNO_3	[111, 112]

The predicted specific impulse as a function of oxidizer-to-fuel ratios (O/F) for some of the amine-boranes under consideration here in comparison to TMEDA and the more conventional hydrazine-based hypergolic fuels with is shown in Figure 38. Unlike more conventional fuels, which typically have a single peak with respect to specific impulse (as a function of O/F ratio), amine-borane fuels (particularly those with high boron weight percentages) commonly exhibit dual peak behaviors [3, 4, 11]. This behavior is illustrated most clearly with AB (as seen in Figure 38), with peaks occurring at O/F ratios of approximately 1 and 3.5. These peaks correspond to the

complete oxidation of boron for the lower O/F peak and the complete oxidation of the boron and hydrogen for the higher O/F peak [4, 7]. In contrast, TEB and TMEDABB (with lower boron weight percentages of 9.4% and 15.03% respectively compared to AB's 35.02%) exhibit a single broader peak. The wide range of O/F ratios offering high levels of performance inherent to these fuels could help maintain high levels of performance during throttling periods. This potential benefit is particularly relevant for maneuvering and attitude control systems characterized by highly transient operation.

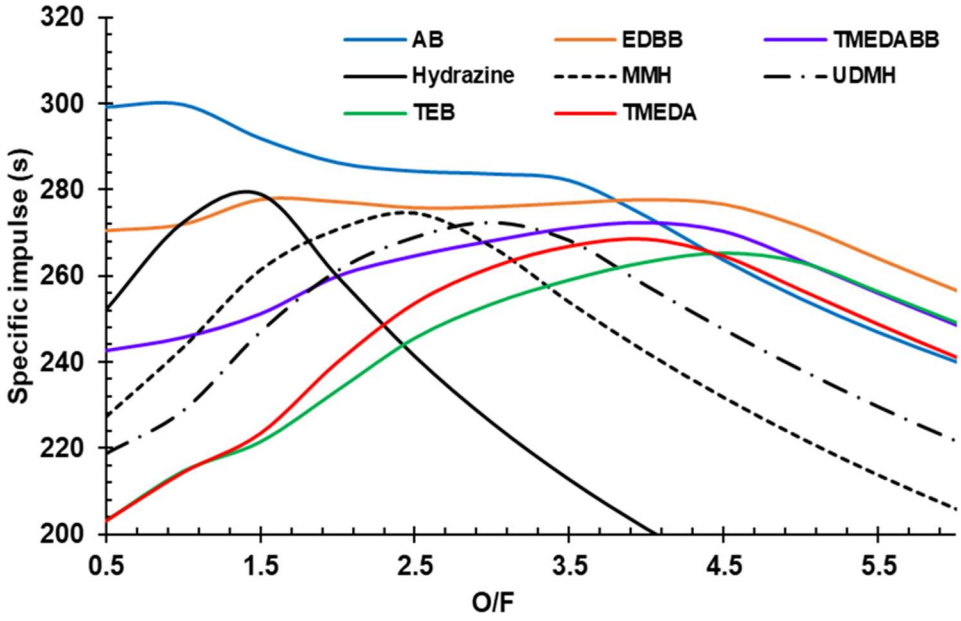

Figure 38: Theoretical performance for TMEDA and the amine-borane fuels under investigation in comparison to the more conventional hydrazine-based fuels.

Theoretical performance calculations were also performed for some of the saturated fuel solutions and gelled fuel mixtures discussed previously. For each of these fuel mixtures, the peak specific impulse (I_{sp}) and density specific impulse (ρI_{sp}) was calculated and tabulated in Table 13. Given the long-term stability concerns associated with the TMEDA-TEB fuel mixtures, these fuel mixtures were not included in these calculations. For the saturated TMEDA fuel solutions, the

"lower limit" and "upper limit" entries correspond to the lower and upper estimates for the solubility of AB/EDBB/TMEDABB in TMEDA. Given the relatively low solubility limits of AB and EDBB in TMEDA, these fuel solutions offer only a marginal improvement in specific impulse in comparison to TMEDA. The slightly higher solubility limit for TMEDABB resulted in the specific impulse of this solution surpassing that of the AB/EDBB solutions. While the specific impulse of these fuels with WFNA is not sufficient to make them competitive with the more standard monomethylhydrazine-nitrogen tetroxide (NTO) combination (I_{sp} = 289 s), the density specific impulse of these fuels is much more competitive (ρI_{sp} = 344 g-s/cm^3 for MMH-NTO) [6, 23]. This suggests that these fuels may be best suited for volume-limited applications. However, if these fuels are similarly hypergolic with the more energy dense hypergolic oxidizers (e.g., red fuming nitric acid, NTO, etc.), the specific impulse of these fuels (compared to MMH) would be much more competitive.

Table 13: Predicted performance of TMEDA-based fuel mixtures with WFNA

	AB		EDBB		TMEDABB	
Fuel type	**I_{sp} (s)**	**ρI_{sp} (g-s/cm^3)**	**I_{sp} (s)**	**ρI_{sp} (g-s/cm^3)**	**I_{sp} (s)**	**ρI_{sp} (g-s/cm^3)**
TMEDA (no additives)	**268.5**	**339.8**	**268.5**	**339.8**	**268.5**	**339.8**
Saturated solution (lower limit)	**268.7**	**339.9**	**268.6**	**339.9**	**268.9**	**342.2**
Saturated solution (upper limit)	**268.9**	**340.2**	**268.7**	**340.2**	**269.0**	**342.6**
5% additive wt. % gel	**267.3**	**339.0**	**266.9**	**338.9**	**266.8**	**339.3**
10% additive wt. % gel	**268.0**	**339.8**	**267.3**	**339.5**	**267.1**	**340.5**
15% additive wt. % gel	**268.8**	**340.6**	**267.6**	**340.2**	**267.4**	**341.7**

For the gelled fuels, the inclusion of the inert fumed silica offsets the gains in specific impulse that could be achieved through higher additive loadings. While the I_{sp} of the 15% AB gelled fuel slightly surpasses that of the TMEDA for similar conditions, the remaining gelled fuels all underperform TMEDA by 1-2 seconds of I_{sp}. Further improvements to the specific impulse would likely necessitate switching to an alternative, non-inert gelling agent (e.g., hydroxypropyl cellulose (HPC)) [114, 115]. Additionally, further optimization of the gel rheology by varying the gellant loading as well as the additive particle size could potentially enable higher additive loadings, improving the overall energy density of the fuel. It has also been shown that reactive nanoscale particles can also act as pseudo-gellants in some cases, reducing the need for inert gelling agents [116-118]. Gelling the fuels increased the density specific impulse slightly at the 15% additive loadings, though the increased ignition delays for the AB/EDBB gels would likely make these formulations impractical for use. These marginal increases in density specific impulse are likely too small however to warrant the added complexity of the gelled fuels, particularly when compared to the much simpler TMEDA fuel solutions offering similar benefits.

6.4 Conclusions

The impacts of adding assorted amine-borane materials to TMEDA were investigated and characterized. For TMEDA-based saturated fuel solutions, the addition of AB/EDBB/TMEDABB resulted in the measured ignition delays decreasing by approximately 43-51% relative to that of TMEDA itself. While all three materials resulted in comparable mean ignition delays, the lower solubility limits of AB and EDBB in TMEDA (compared to TMEDABB) suggests that these materials are more effective at improving the ignition delays, particularly at lower weight fractions.

The addition of triethylamine borane to TMEDA resulted in some of the most significant improvements in ignition delay for the assorted amine-boranes investigated here. However, the stability of the TMEDA-TEB fuel mixtures appears questionable, given the ready formation of a white solid material even at room temperature. NMR analysis of this material suggests that it is likely tetramethylethylenediamine bisborane, formed through a trans-borylation reaction between the TMEDA and TEB. Consequently, triethylamine borane is likely unsuitable for use as an additive in fuel formulations with TMEDA and other amine compounds.

In general, the minimum ignition delays measured for the gelled TMEDA fuels with the three solid amine-boranes was at best comparable to those measured for the saturated (i.e. non-gelled) TMEDA solutions. Increasing the amine-borane weight fraction beyond their respective solubility limits offered diminishing returns with regards to decreasing the ignitions delays and, for the AB/EDBB mixtures, increased the ignition delay. This may suggest that the solid particles are not reacting fully on the relevant time scales and potentially acting as heat sinks, slowing the rate at which the system temperature increases. Additionally, the increased viscosity of the gelled fuel mixtures (compared to the non-gelled fuels) likely prevented the oxidizer droplet from readily mixing with the fuel, further slowing the rate of reaction. However, as the drop test experimental configuration used here does not reflect the injection and mixing dynamics present in liquid rocket engines, these mixing issues would likely be less prominent in a more realistic configuration.

Theoretical performance calculations suggest that for volume-limited applications (where density specific impulse becomes more relevant), the TMEDA-based fuel mixtures investigated here are competitive with the more standard MMH-NTO combination. Given the inert nature of the fumed silica used to prepare the gelled fuels, these fuels offered little to no benefit in specific impulse compared to TMEDA itself. Switching to an alternative, non-inert gelling agent would

likely improve the predicted performance of these materials. In addition, switching to nanoscale reactive particles for these additives could reduce the inert gelling agent weight fraction necessary to gel these fuels, further improving the energy density of these fuels. Considering their relative simplicity and consistently short ignition delays, the saturated TMEDA fuel solutions appear to be the most promising fuels investigated in this work. If these fuels result in similar ignition delays with other hypergolic oxidizers (e.g., RFNA, NTO, etc.), their predicted specific impulse would be much closer to MMH-NTO. If this is indeed the case, these fuels could potentially serve as much safer, drop-in replacements for the highly toxic hydrazine-based fuels, greatly reducing the health hazards associated with handling these fuels.

7. PERFORMANCE OF AMMONIA BORANE-BASED FUELS IN HYPERGOLIC HYBRID ROCKET MOTORS

7.1 Introduction

While they offer high specific impulse values and short ignition delays when used in hypergolic propellant systems, hydrazine and other hydrazine derivatives (e.g., monomethyl hydrazine, unsymmetrical dimethyl hydrazine, etc.) are highly toxic. Despite the strong motivation to find a less toxic alternative, few viable alternatives have been developed due to a lack of understanding of the fundamental chemical kinetics governing the hypergolic behavior of these propellants [1, 2].

Recently, amine-boranes have begun receiving increased attention as potential alternatives to the more conventional hydrazine-based fuels [2-4, 11]. One amine-borane of interest for use as a solid fuel in hypergolic hybrid systems is ammonia borane (AB). The high hydrogen density of ammonia borane (19.6 percent hydrogen by mass) makes it a particularly attractive fuel candidate due to hydrogen's low molecular weight. More importantly, ammonia borane has been shown to be highly hypergolic with white fuming nitric acid (WFNA) with ignition delays as short as 1-2 milliseconds [2-4, 107]. In addition, thermochemical equilibrium calculations performed with CHEETAH 7.0 thermochemical code predict higher specific impulse values when ammonia borane-based fuels are used with WFNA in place of the typical hydrazine-based fuels [55]. As seen in Figure 39, ammonia borane also shows a dual-peak behavior which would allow for high specific impulse values across a wide range of O/F ratios.

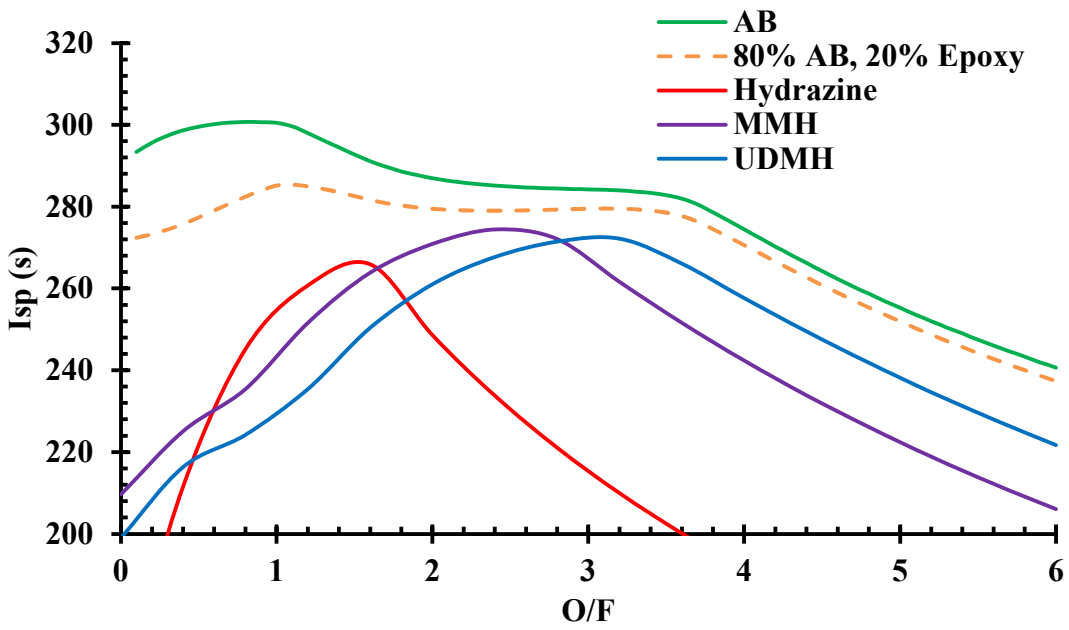

Figure 39: Theoretical performance of a variety of hypergolic fuels with WFNA assuming chamber pressures of 68 atm and perfectly expanded to atmospheric pressure

To date, ammonia borane has yet to be tested in a hybrid rocket motor with any of the commonly used hypergolic oxidizers in the open literature. Much of the prior work investigating ammonia borane for use in solid and hybrid propellant formulations has been hindered by compatibility issues with many of the binders commonly used in propellant formulations [3, 4]. Lee et al. reported that the addition of AB to a HTPB-AP composite propellant resulted in the binder failing to cure due to the AB interfering with the HTPB crosslinking process [19]. Similar compatibility issues were also present when AB was mixed with polybutadiene acrylonitrile (PBAN) and carboxyl terminated polybutadiene (CTPB) binders (though these issues were less obvious at higher solids loadings) [4]. As an alternative to these more conventional binders, Weismiller et al. made use of paraffin wax to successfully prepare fuel grains loaded with ammonia borane [20]. When tested in a small scale hybrid motor with gaseous oxygen, combustion efficiencies upwards of 90% were reported for AB loadings of up to 50% by mass [20]. The objective of this work is to further investigate the performance of ammonia borane-based fuels

when used in hybrid rocket motors, particularly when used with hypergolic oxidizers like white fuming nitric acid.

7.2 Experimental Methods

7.2.1 Fuel Grain Preparation

The ammonia borane used here was synthesized at Purdue University at the H.C. Brown Center for Borane Research using a water promoted synthesis method described previously [50]. To improve the mechanical properties of the prepared fuel grains, EnviroTex Lite® epoxy was used as a fuel binder. This epoxy-based binder was shown previously by Clements et al. result in properly curing samples at high AB solids loadings [5, 108]. An 80% AB solids loading (by weight) was used for these fuel grains as this AB loading was also shown previously by Clements et al. to offer the lowest mean ignition delays while still offering predicted performance that surpasses that of the standard hydrazine-based fuels [5, 108]. The Ammonia borane-based fuel grains were prepared by first mixing the EnviroTex Lite® resin and hardener components in a 1:1 ratio by mass. This epoxy mixture was then mixed by hand for several minutes after which the AB was gradually added and mixed by hand. Once all the AB was added and sufficiently wetted by the binder, a Resodyn LabRam resonant mixture was used to mix the mixture further for 5 minutes at 80 G's acceleration.

As the AB-epoxy mixture was too dry to be cast-cured into molds at the high solids loadings used here, the mixture was pressed into 12.7 mm ID, 25.4 mm OD fuel grain segments using a hydraulic press and custom press die. The press die was loaded with enough of the AB-epoxy mixture to result in fuel segments approximately 50.8 mm long. These segments were pressed in two 5-minute-long intervals at approximately 4000 psia applied pressure, with half of the total segment mass being added before each interval to help minimize density gradients along

the segment length. After pressing, these segments were cured for several days at room temperature. Examples of typical pressed fuel grain segments can be found in Figure 40. Once the segments were cured, the fuel grains were assembled by first aligning the segments end-to-end on a 12.7 mm acetal mandrel with a thin layer of epoxy applied between each layer. A light layer of epoxy was then applied to the outer surface of the segments to secure them in a 25.4 mm ID, 50.8 mm OD phenolic tube liner. The front face of the head-end fuel grain segment recessed 6.35 mm from the head-end of the phenolic tube liner so that this face is in line with the face of the injector. This process was used to prepare both 152.4 and 304.8 mm long fuel grains. Before each test, the inner port of each fuel grain was sanded to remove any excess epoxy on the fuel surface.

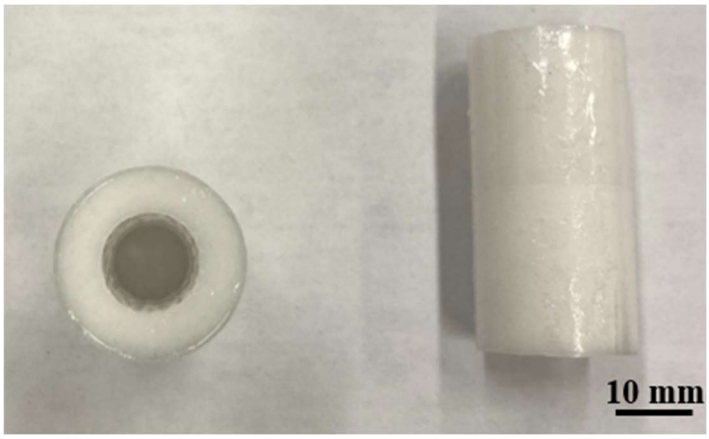

Figure 40: Representative pressed AB-epoxy fuel grain segment

7.2.2 Hybrid Rocket Combustor

The hybrid rocket motor used for this study (shown in Figure 41) is comprised of several modular stainless-steel sections. This allows the same post combustion chamber and nozzle assembly to be used for both the 152.4 and 304.8 mm-long fuel grains that will be tested. Graphite nozzles with 45° half angle converging sections and varying throat diameters were used for this system. The throat diameter of the graphite nozzles used for each test was set based on the target chamber pressure and expected fuel/oxidizer flow rates. To improve the flow characteristics and

help prevent the nozzle from clogging due to any potential condensed phase products, a small diverging section (not pictured in Figure 41) was added to each of the nozzles used.

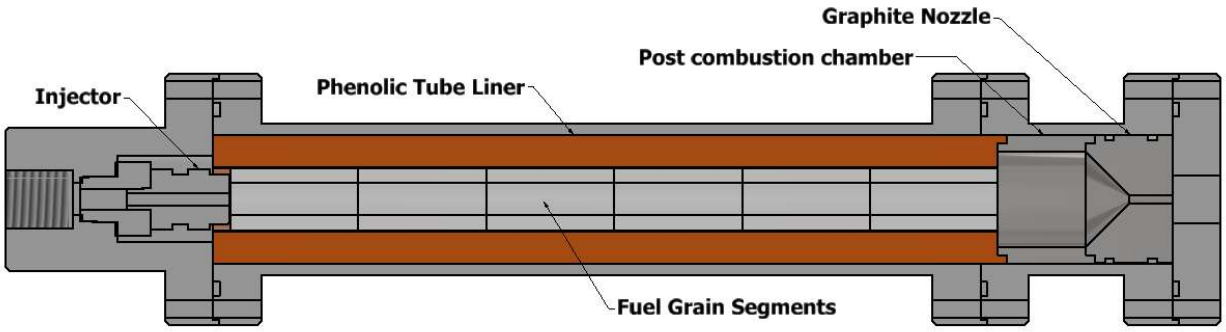

Figure 41: Hybrid rocket motor used for investigating the performance of ammonia borane-based fuel grains

The WFNA used for these tests was supplied to the motor using a simple pressure-fed flow system as shown in Figure 42. Bulk nitrogen gas was used to pressurize the WFNA prior to testing. To provide a stable oxidizer flowrate to the motor, a stainless-steel cavitating venturi was used (throat diameter 0.4318 mm). This had the added benefit of helping to isolate the flow system upstream of the venturi from any significant pressure fluctuations that may result during these tests (particularly during ignition transients). The upstream/supply pressure was varied using a Tescom ER-3000 electronic regulator to allow for different WFNA flowrates (and as a result oxidizer-to-fuel ratios) to be achieved. For these tests, a Spraying Systems Co. 1/8GG-316SS1 FullJet cone spray nozzle installed in the head end of the combustion chamber was used as an injector.

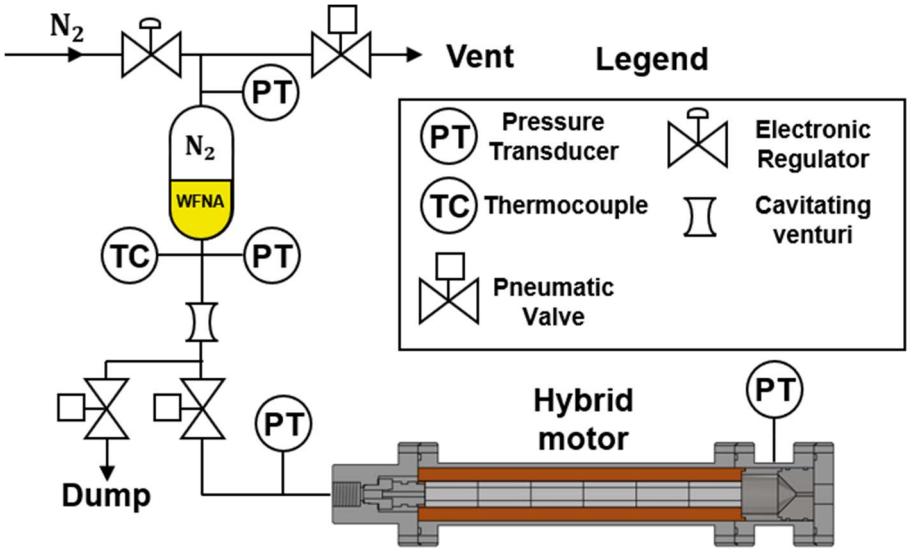

Figure 42: Simplified plumbing and instrumentation diagram (P&ID) for flow system used to supply WFNA to hybrid motor

During each test, the motor chamber pressure was monitored using a GE UNIK 5000 pressure transducer. In addition, a Druck PMP1260 pressure transducer installed upstream of the cavitating venturi was used to monitor the WFNA pressure. The oxidizer mass flow rate ($\dot{m}_{ox}$) for each test was determined from the relation,

$$\dot{m}_{ox} = A_{venturi} C_{d,venturi} \sqrt{2 g \rho_{WFNA} (P_{venturi} - P_v)}$$

where $A_{venturi}$ is the venturi throat area, $C_{d,venturi}$ is the discharge coefficient of the venturi, g is gravitational acceleration, ρ_{WFNA} is the density of WFNA, $P_{venturi}$ is the venturi upstream pressure, and P_v is the vapor pressure of WFNA.

The overall test matrix completed over the course of this work is outlined in Table 14. A total of 5 tests were completed here, with the first test intended to verify the hypergolic ignition of the fuel in this motor configuration. To reduce the risk of over pressurization, the nozzle throat diameter for this test was intentionally oversized. To date, there has been no regression rate data published in the open literature for the AB-based fuel formulation used here. To provide an initial estimate of this parameter, the regression rate data obtained previously with this same hybrid motor

for fuel grains based on ethylenediamine bisborane (EDBB) with WFNA was used [7]. After completing the first full duration hot fire test (test no. 2), the regression rate estimates were revised based on the regression rate measured during this test. The objective of the tests that followed (test no.'s 3-5) were then intended to investigate the influence of the oxidizer mass flux on the fuel regression rate for a target steady state operating pressure of 250 psia.

Table 14: Test matrix for hybrid motor tests

Test no.	Test duration (s)	Fuel grain length (in)	WFNA tank pressure (psia)	WFNA Flow rate (g/s)	WFNA volume (ml)	Initial oxidizer mass flux $(\mathrm{kg/m^2s})$	Target steady state chamber pressure (psia)	Nozzle throat diameter (in)	Test objective
1	3	6	400	11.65	25	92	14.7	11/32	Verify ignition of fuel grain in motor configuration with oversized nozzle throat
2	7	12	400	11.65	57	92	100	5/32	Compare estimated regression rates to measured (average) regression rate, refine estimates for future tests
3	7	12	600	14.27	70	113	250	13/64	Measure chamber conditions/fuel regression rate for given oxidizer flow rate and nozzle throat diameter (based on estimated fuel regression rates)
4	7	12	800	16.48	81	130	250	7/32	
5	7	12	400	11.65	57	92	250	3/16	

7.3 Results and Analysis

For each of the motor tests performed, the experimental characteristic velocity (C*) was determined based on the following relation,

$$C^* = \frac{A_{th}P_C}{\dot{m}_f + \dot{m}_{ox}} = \frac{A_{th}}{m_f + m_{ox}} \int_0^{t_b} P_c(t)dt$$

where A_{th} is the nozzle throat area, m_f/m_{ox} are the total amounts of fuel/oxidizer consumed during each test, $P_c(t)$ is the chamber pressure as a function of time, and t_b is the test duration [56]. The integral in this equation was numerically integrated using the trapezoidal rule based on the

measured chamber pressures and the time between each successive data point. The test/burn duration was estimated from videos taken during each test based on the amount of time that passed from when the first visible smoke/flame/etc. was observed from the motor to when the motor/fuel grain quenched. For the chamber pressure data, the "start" of the burn was defined as the time when the chamber pressure reaches 10 percent of the peak chamber pressure achieved. The fuel mass consumed during each test was obtained by measuring the mass of the fuel grain before and after each test. Using the average chamber pressure and the oxidizer/fuel flow rates, the theoretical/ideal C* was obtained from NASA CEA [111, 112]. The delivered C* efficiency (η_{C^*}) was then determined from the relation,

$$\eta_{C^*} = \frac{{C^*}_{exp}}{{C^*}_{th}}$$

where ${C^*}_{exp}$ is the experimentally determined C* value and ${C^*}_{th}$ is the theoretical C* value obtained from NASA CEA for the experimental operating conditions.

The results for each of the tests performed during this test campaign are outlined in

Table 15. For each test case listed in the table, two separate average chamber pressure entries are listed, corresponding to the average chamber pressure during the full burn duration ($\overline{\boldsymbol{P_{c,tb}}}$) and the peak/steady state conditions ($\overline{\boldsymbol{P_{c,ss}}}$). The difference in these time frames is illustrated for test 2 in Figure 43.

Table 15: Summary of motor performance parameters for each of the motor tests performed

Test number	1	2	3	4	5
Fuel grain length (cm)	15.24	31.15	30.40	30.40	30.25
$\dot{m}_{ox}$(g/s)	11.65	11.65	14.27	16.48	11.65
G_{ox} (kg/m^2s)	91.96	91.96	112.67	130.12	91.96
t_{burn} (s)	-	10.41	10.31	10.95	10.50
ρ_{fuel} (g/cm^3)	0.7716	0.7574	0.7693	0.7674	0.7724
Fuel mass consumed (g)	21.30	49.83	47.95	47.83	46.90
Percentage of fuel mass consumed (%)	51.20	59.76	57.22	57.29	56.00
$\dot{m}_{fuel}$ (g/s)	-	4.79	4.65	4.37	4.47
$\dot{r}_{avg}$ (mm/s)	-	0.39	0.38	0.36	0.37
O/F	-	2.43	3.07	3.77	2.61
$\overline{P_{c,t_b}}$ (psia)	-	197.38	118.65	116.53	120.30
$\overline{P_{c,ss}}$ (psia)	-	339.25	252.02	220.75	277.10
$C^*_{exp.}$ (m/s)	-	1265.57	1106.56	1193.94	1267.06
η_{C^*}	-	0.75	0.66	0.74	0.75
$\overline{Thrust_{ss}}$ (lbf)	-	8.95	8.50	9.55	7.22

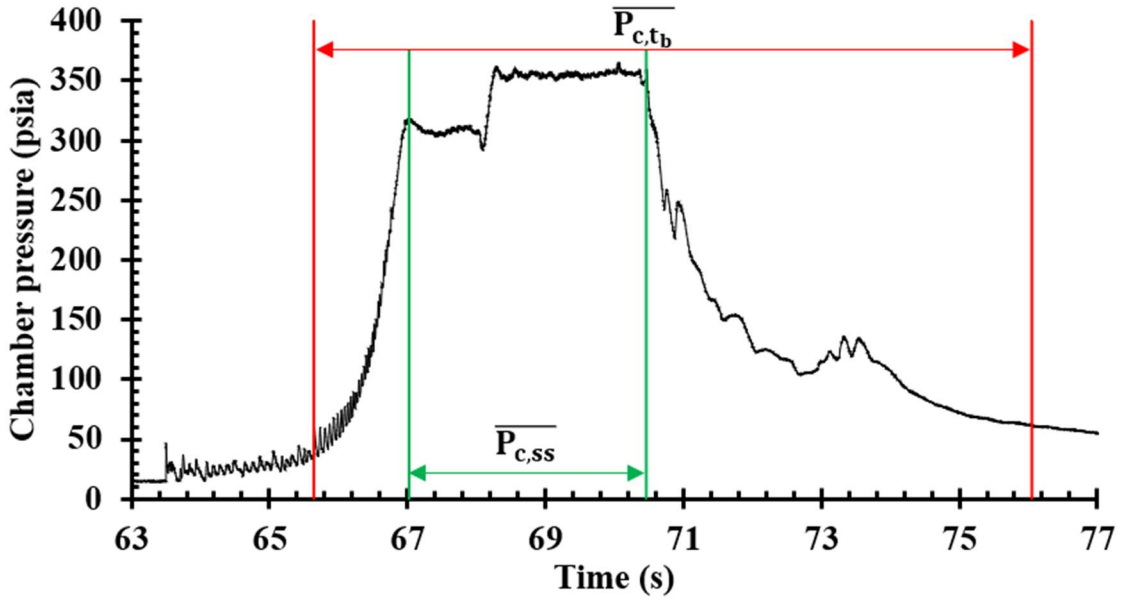

Figure 43: Representative chamber pressure time history showing difference between the full burn average pressure ($\overline{P_{c,tb}}$) and the peak/steady state operating pressure ($\overline{P_{c,ss}}$)

For the five tests performed, hypergolic ignition of the fuel grains was successfully achieved in all test cases. As shown in Figure 44, the initial ignition corresponded to a spike in the chamber pressure, after which the chamber pressure gradually increased to its steady state/operating pressure over the course of 3-4 seconds. During this period, the chamber pressure exhibited small scale (i.e., 2-5 psia) pressure oscillations with an oscillatory frequency that typically ranged from 20-35 Hz before eventually dampening out as the motor reached its operating pressure. High speed video recorded during this period showed the exhaust plume varying in intensity, with the motor appearing to quench and reignite periodically until the motor reached its operating pressure. At this time, the exhaust plumes stabilized, and well-defined shock diamonds were observed. Examples of the exhaust plume structure during the transient and steady-state phase can be found in Figure 45.

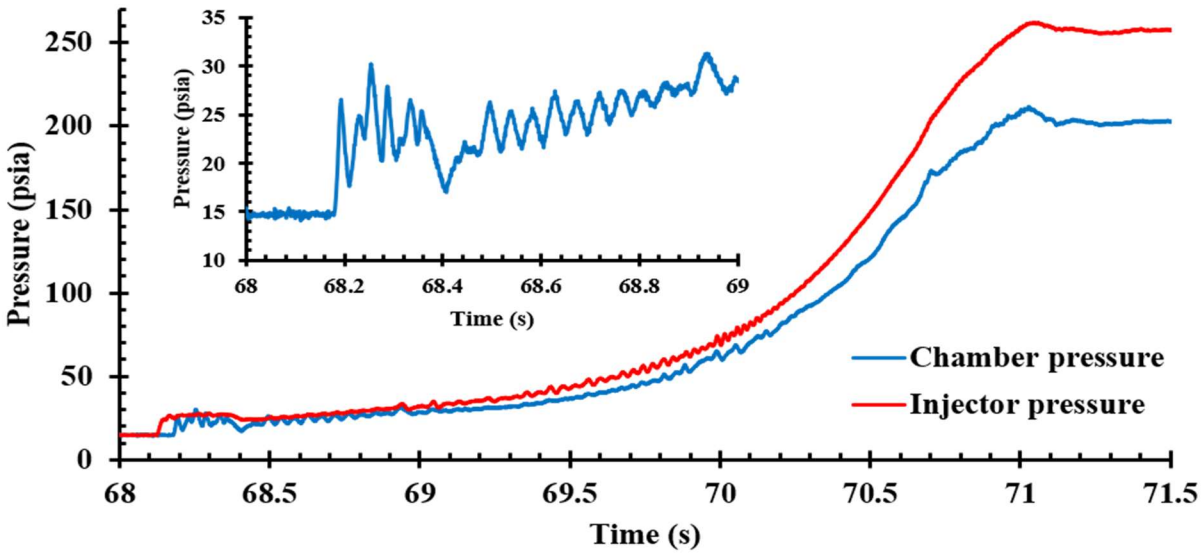

Figure 44: Representative chamber and injector pressure traces during the initial ignition phase (data for test no. 4 shown)

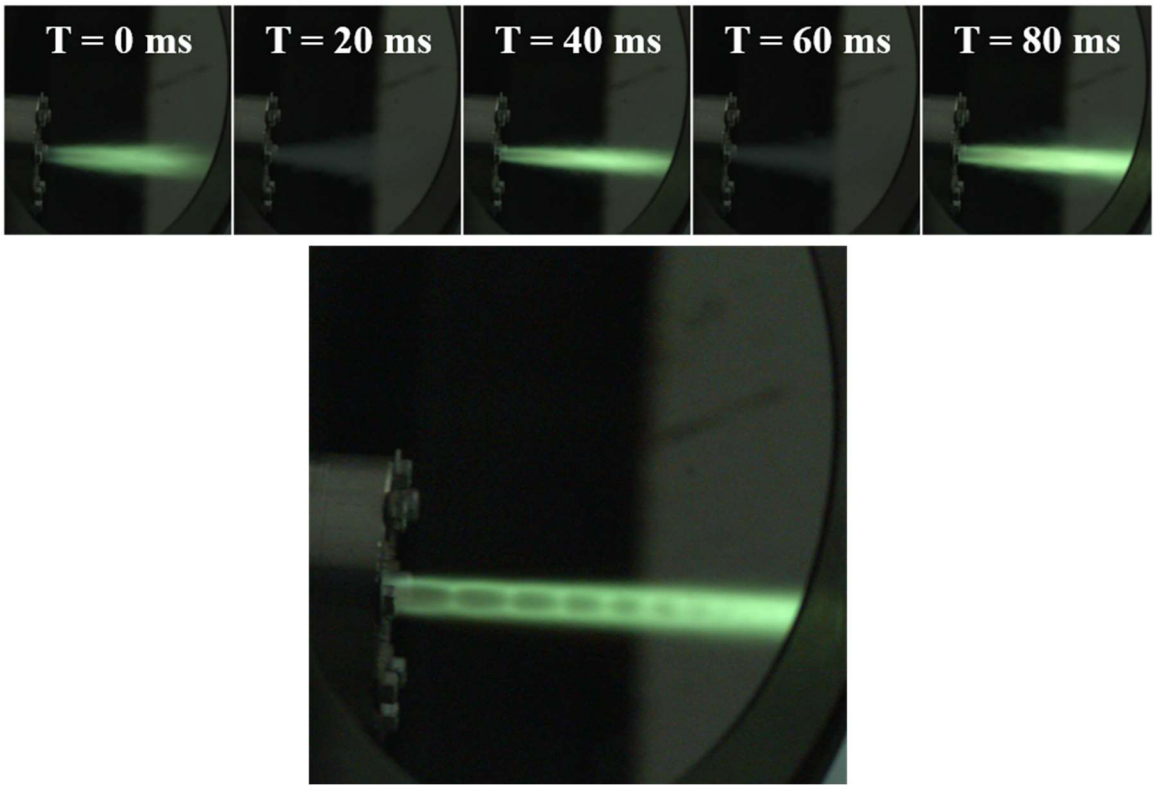

Figure 45: Image sequence showing motor exhaust plume during the transient ignition period (top) and during steady-state operation (bottom)

For the first full duration hot-fire test (test no. 2), the fuel mass flow rate was much higher than expected based on the estimates from the tests performed previously with EDBB-based fuel grains. As shown in Figure 46, the measured chamber pressures for this test were significantly higher than the 100 psia chamber pressure predicted based on regression rate estimates for the work performed previously with EDBB. Unexpectedly, the chamber pressure during the steady burning phase (i.e., Time=67.1 s to 70.5s in Figure 46) exhibited two periods of relatively constant pressure, with a sharp jump/discontinuity separating the two. The higher chamber pressure after the jump may have resulted from a higher oxidizer mass flow rate, potentially due to the pressure drop across the cavitating venturi being too low to maintain cavitation in the venturi throat. For most properly performing cavitating venturis, a pressure drop of at least 15% is considered the minimum necessary for proper cavitation to occur [119]. For this test, this corresponds to an injector pressure (measured downstream of the venturi) of approximately 340 psia. As the injector pressure was at most 332-333 psia prior to the jump, the venturi was likely cavitating properly during this initial phase. Following the jump however, the injector pressure ranged from 380-385 psia, suggesting the venturi was no longer cavitating, leading to the higher oxidizer mass flow rate and chamber pressure observed during this period. Given the gradual decrease in chamber pressure leading to the jump, the exact cause of this discontinuity is unclear.

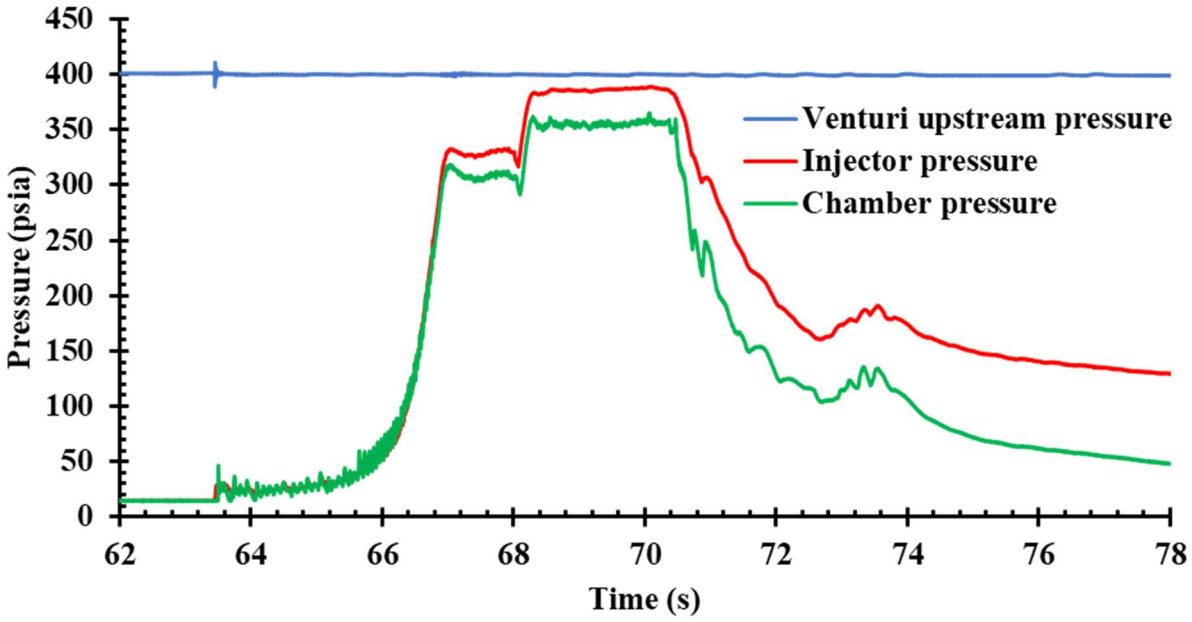

Figure 46: Chamber pressure, injector pressure, and venturi upstream pressure vs time for test no. 2

As shown previously in

Table 15, for each of the full hot-fire tests performed (i.e., tests number 2 through 5), the measured C* efficiencies (η_{C^*}) ranged from 66 to 76 %. These relatively low η_{C^*} values suggest the incomplete combustion of the fuel and oxidizer. Low combustion efficiencies can in many cases result from non-optimal combustion chamber design (e.g. low residence times, poor injection/mixing, heat loss to the combustor walls, etc.) [23]. Additionally, the formation of condensed-phase product species can result in further reductions in the overall combustion efficiency. These issues can in many cases be remedied through further optimization of the combustion chamber design for a given fuel and oxidizer combination.

For all the tests performed during this test campaign, examination of the nozzle and post combustion chamber following each test revealed that a considerable amount of condensed-phase products had accumulated on the surfaces of the post combustion chamber and nozzle. Representative images showing this behavior can be seen in Figure 47. As these products do not contribute to the chamber pressure while still counting towards the total fuel mass consumed, their formation was likely a contributing factor to the low C* efficiencies encountered here. However, it is unknown if the formation of these products occurred during regular motor operations or during the nitrogen purge period that followed each test. This issue is convoluted further through the potential ejection of condensed phase material from the fuel grain during this purge period. In some cases (such as the test case shown in Figure 47), larger chunks of material were observed in the converging section/throat of the nozzle. This ejected material would introduce additional error in the fuel mass consumed and consequently result in reduced C* efficiencies.

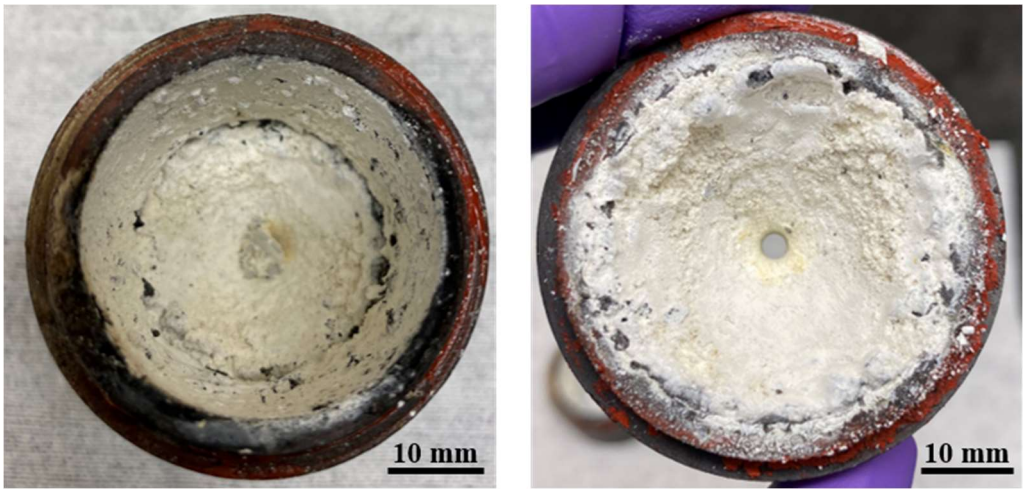

Figure 47: Representative images showing accumulation of condensed phase products on surface of post combustion chamber and nozzle

Unlike the more conventional solid fuels used in hybrid rockets, where the fuel surface regresses as it is consumed during motor operation, the AB-epoxy fuels used here exhibited considerable swelling during the tests performed. As a result, even though approximately 56-60%

of the fuel mass was consumed, the fuel port diameters remained roughly constant or in some cases decreased compared to the pre-fired port diameters. In addition, the fuel surface along the length of the fuel grain was highly irregular, with certain sections swelling more than others. Representative images taken down the ports of different fired fuel grains can be found in Figure 48. As a result of these issues, obtaining regression rate measurements using direct measurements of the port diameter was not practical, as doing so would result in inaccurate (or negative) regression rates.

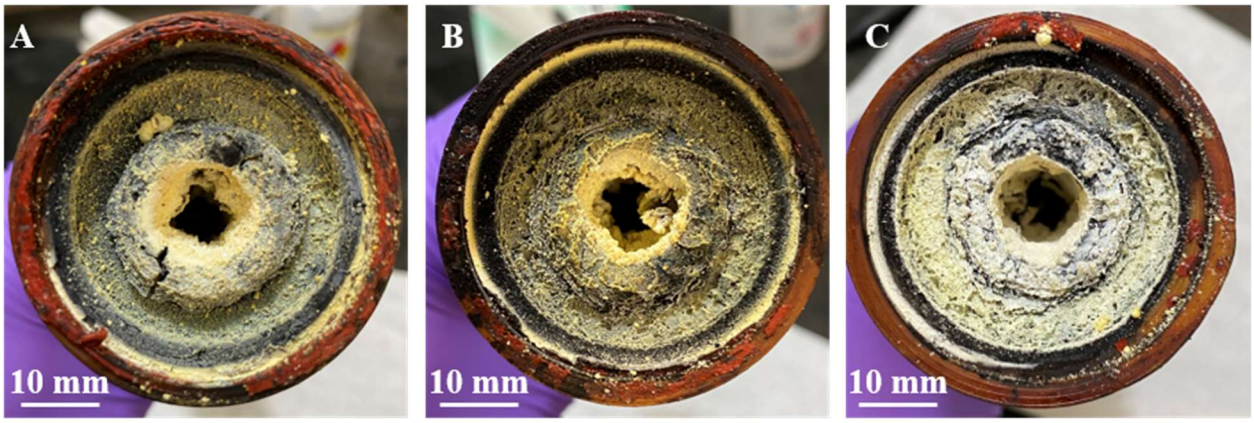

Figure 48: Representative images of the post-fired ports of different AB-epoxy fuel grains (A: test no. 3, B: test no. 4, C: test no. 5)

To enable comparison with EDBB-epoxy and other solid fuels, the "effective" regression rate (i.e. the regression rate of the fuel had it regressed like a more conventional fuel) was estimated for each of the tests performed. For each of the fuel grains used, the mass, length, inner diameter, and outer diameter were measured for each fuel grain segment to determine the average fuel density. The effective final port diameter was than determined based on the final fuel mass and the average fuel grain density. From this effective port diameter, the change in fuel grain web thickness was calculated, after which the effective regression rate was calculated by dividing the change in web thickness by the burn duration.

The effective regression rates for each of the tests performed are plotted as a function of oxidizer mass flux in Figure 49. The values listed in parentheses next to each data point are the average chamber pressures measured for each test case. Also included in the plot are the results obtained previously for EDBB-epoxy (80% EDBB by wt.) with WFNA using the same hybrid combustor used here [7]. As shown in the plot, the regression rates of the AB-based fuels rivaled the highest regression rates measured for the EDBB-based fuels. This is made more noteworthy based on the fact that the EDBB-based fuels grains used in this earlier study had a series of 8 2.54 mm slots cut around the circumference of the port, resulting in a higher fuel surface area relative to the simple center perforated grain used here [7]. In addition, unlike the regression rate behavior of the EDBB-based fuels, which varied considerably from test-to-test, the effective regression rate of the AB fuels was almost constant across all four tests performed.

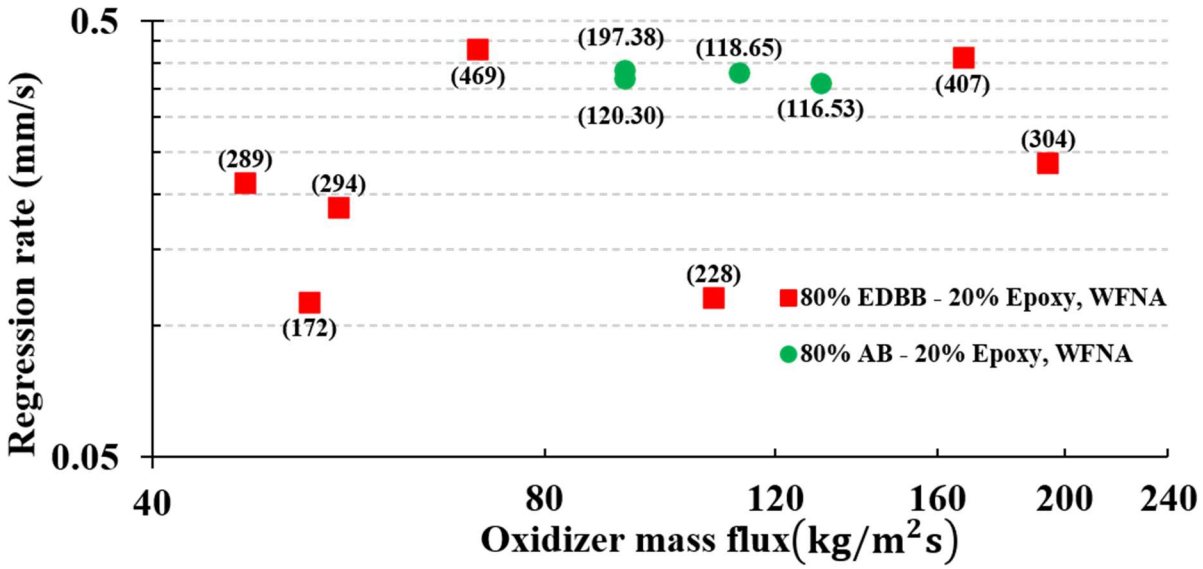

Figure 49: Effective regression rate data for AB-Epoxy fuel grains with WFNA in comparison to EDBB-Epoxy with WFNA (Pfeil) [7]. The values listed in parentheses for each data point are the average chamber pressures during the full burn duration

Unlike more conventional solid fuels, whose regression rates generally scales with the oxidizer mass flux, the AB-based fuels exhibited little to no dependence on the oxidizer mass flux

for the range of mass fluxes used here. In addition, the regression rate behavior of these fuels also showed no significant dependence on chamber pressure in notable contrast to that of the EDBB-based fuels. This may suggest that the mechanism governing the mass flow rate of the AB-based fuels is fundamentally different from that of the foam layer theory by Pfeil for EDBB, where the chamber pressure strongly influenced regression rates [7].

Given the typical range of fuel consumed during each test (approximately 56-60%), the thermal decomposition of the AB may be one of the major factors driving the fuel mass flow rate. Thermogravimetric analysis (TGA) of ammonia borane by Frueh et al. has shown that AB will undergo a significant mass loss of approximately 65% when heated from 98 ºC to approximately 200-250 ºC [120]. Further heating of the AB did not result in additional mass loss until a temperature of 1170 ºC was reached, at which point an additional mass-loss phase occurred [120]. As the fuel grains used here consisted of 80% AB, assuming the fuel grain reached temperatures of 200-250 ºC, the AB contributions to the mass loss would be expected to be approximately 52%. The remaining mass loss would then be due to the epoxy component of the fuel grains being consumed as a more conventional solid fuel. As this thermal decomposition likely continued to some extent during the purge period, this would also have contributed to the low C* efficiencies discussed previously. This was demonstrated most clearly for the first test performed, where (as shown in Figure 50), the fuel continued burning with the ambient air for almost a full minute during the purge phase despite the WFNA flow shutting off after 3-4 seconds.

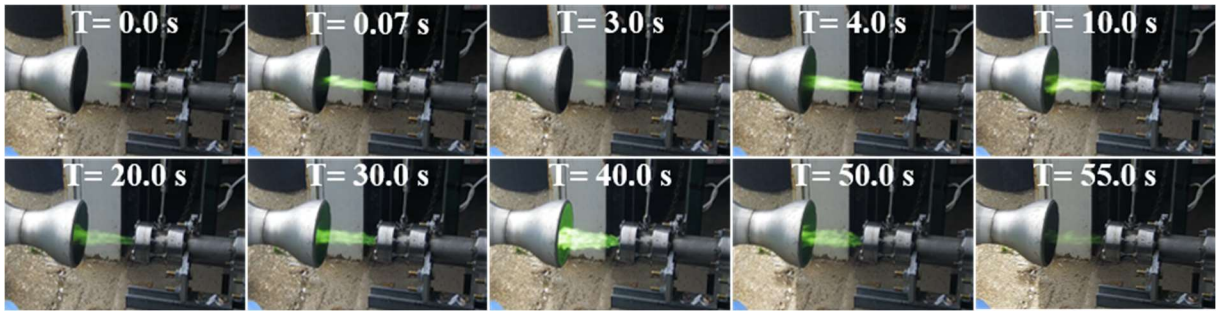

Figure 50: Image sequence from test no. 1, where thermal decomposition of the fuel grain resulted in the fuel continuing to burn for approximately 50-55 seconds after oxidizer shut-off

7.4 Conclusions

The performance of ammonia borane-based fuel grains in a hypergolic hybrid rocket motor was successfully characterized for the first time in the open literature. For each of the 5 tests performed, hypergolic ignition of the fuel grain was achieved in all cases with no evidence of hard-starts occurring. However, the rate at which the pressure built up within the combustion chamber was generally slow, with the combustor taking 3-4 seconds to reach steady-state operating conditions in some cases. Further optimization of the injector spray (increasing the fuel surface area wetted by the WFNA) and overall combustor design may help reduce the duration of this start-up transient period.

In comparison to the earlier reported results for EDBB-based fuels with WFNA in a hypergolic hybrid motor, the AB-based fuels used here exhibited regression rates that, at slowest, rivaled the fastest observed for the EDBB-based fuels. Unlike these EDBB-based fuel grains however, the regression rate of the AB-based fuel grains showed little-to-no dependence on both chamber pressure and oxidizer mass flux. Instead, the fuel mass flow rate appears to be driven largely by the thermal decomposition of the ammonia borane. In each case, the total amount of fuel consumed was on par with the mass loss expected for the thermal decomposition of ammonia

borane heated beyond 200-250 ℃. Investigations of the thermal profiles present in the fuel grain during motor operation is necessary to confirm this, however.

Assuming the thermal decomposition of AB is indeed the phenomena governing the fuel mass flow rate, it may introduce additional design/operation limitations to hybrid rockets utilizing ammonia borane-based fuels. Depending on the temperatures reached in the fuel grain, residual heat present in the fuel grain after the motor has extinguished may result in continued decomposition of the fuel. While this would likely not affect simpler flight/mission profiles with a single burn phase, flight profiles requiring shut-off and restart capability may necessitate shorter burn durations and careful grain design to limit the internal temperatures reached by the fuel. In addition, full consumption of the fuel may be impractical if this necessitates heating the fuel to beyond 1170 ºC to initiate the final thermal decomposition step for the AB, introducing potential "dry" weight to any systems using these fuels.

8. CONCLUSIONS AND FUTURE WORK

8.1 Conclusions

Through the course of the various experimental efforts discussed throughout this dissertation, ammonia borane has been investigated for use as a potential fuel for use in hypergolic hybrid rocket systems. Using a small-scale hypergolic ignition drop test configuration, the ignition delay behavior of AB was characterized with white fuming nitric acid. For the neat material, a particle size dependency on the ignition delay was observed, with finer particles resulting in ignition delays as short as 0.6 milliseconds, some of the shortest ever reported for hypergolic solid fuels. To enable future testing efforts, a survey of available fuel binders was performed, and a series of compatibility tests performed to find a binder compatible for use with AB. Of the binders investigated, Sylgard-184 ® (a silicone elastomer based formulation) was found to result in properly curing fuel samples when mixed with AB. When tested with WFNA, these fuel samples resulted in ignition delays typically between 20-40 milliseconds, suggesting that this formulation may be suitable for use in a hypergolic hybrid rocket motor.

As a means of potentially investigating the surface chemistry and combustion behavior of AB when reacting with WFNA (and other hypergolic oxidizers), the feasibility of using phosphor thermography to measure the surface temperature of reacting AB was investigated. As a proof-of-concept study, this technique was adapted for use in measuring the surface temperature of burning nitrocellulose (a homogeneous solid propellant). Using a system operating at 10 Hz, the average surface temperature across the burning propellant surface was measured to be approximately 534 K. These values were in good agreement with reference thermocouple data published previously for nitrocellulose (T=523 K). This demonstrated the viability for using phosphor thermography to

study the surface temperatures of energetic materials, particularly for measurements obtained through a flame.

As an additional means of studying the combustion behavior and ignition dynamics of AB, a novel high speed multi-spectral imaging technique was developed. Unlike earlier spectral imaging efforts published elsewhere which focused primarily on studying hydrocarbon combustion, this work investigated the use of several boron based species (e.g. BO, BO_2, HBO_2, and the B-H stretch mode of AB and its assorted fuel decomposition products). Using a combination of a high speed visible and IR camera, simultaneous emissions from two species could be obtained, with the potential for additional species to be obtained simultaneously using additional cameras or more elaborate imaging configurations. This technique was used to study the hypergolic ignition of AB with 70% nitric acid as well as the quasi-steady case of AB burning with air. During the ignition period, emissions from HBO_2 were observed during the initial gas evolution state (prior to ignition), suggesting the rapid formation of HBO_2 even at pre-ignition temperatures. The heat release resulting from the formation of HBO_2 at the AB-nitric acid interface may help provide the energy necessary to decompose the AB/nitric acid as well as drive the thermal runaway eventually resulting in ignition. Once nitric acid was consumed/dispersed and the AB pellets began burning with the ambient air, a quasi-steady diffusion flame formed. Intensity profiles for the various species during this time revealed that the BO/BO_2 emissions were strongest in the flame zone, where temperatures are expected to be the highest. Unexpectedly, the HBO_2 emissions reached their peak values within the inner (fuel rich) region of the flame, after which they gradually dropped off across the flame zone. This is seemingly contradictory to the current understanding that HBO_2 is a stable product species, as the emission intensity would be expected to increase with temperature assuming the concentration remains roughly constant. Further

investigation of the temperature profiles in these flames as well as the emissions of the other boron oxides not investigated here (e.g. B_2O_2, B_2O_3, etc.) is necessary to say this conclusively, however.

Given the short ignition delays for ammonia borane (and other amine-boranes), a side study investigating the impacts of adding these materials to tetramethylethylenediamine (TMEDA), was performed with the interest of providing an additional use case for these materials beyond hybrid rockets. For this work, ammonia borane, ethylenediamine bisborane, tetramethylethylenediamine bisborane, and triethylamine borane (a liquid amine-borane) were considered. Mixtures of TMEDA and TEB resulted in the shortest ignition delays as short as 3-4 milliseconds, shorter than those found for either fuel individually. Unfortunately, these fuel mixtures do not appear to be suitable for long-term use, as reactions between the TMEDA and TEB would result in the formation of TMEDABB over time. Despite being only sparingly soluble in TMEDA in some cases, the three solid amine boranes (AB, EDBB, and TMEDABB) resulted in the ignition delay of these solutions being 43-51% shorter than that of TMEDA itself. Gelled TMEDA fuel formulations with 5, 10, and 15% solid amine-borane by mass were also prepared and tested to allow for additive loadings beyond their respective solubility limit. For AB and EDBB however, increasing the additive loading beyond the solubility limit resulted in longer ignition delays. For TMEDABB, increasing the additive loading seemed to decrease the ignition delays, though the shortest ignition delays were still on par with the saturated TMEDA solutions. While their predicted performance with WFNA was less than that of the hydrazine-based fuels, the simplicity, reduced toxicity, and short ignition delays of the saturated TMEDA solutions could enable them to serve as safer alternatives to the standard hypergolic fuels currently in use.

Finally, using a small scale hybrid rocket motor, the behavior of fuel grains based on AB was characterized when tested with WFNA under typical motor conditions. For each of the tests

performed, hypergolic ignition of the fuel grain was achieved successfully in all cases. However, the duration of the pressure buildup phase was longer than expected, with most tests requiring 3-4 seconds before reaching the steady-state/operating pressure was reached. Additionally, the C* efficiencies measured during the tests performed generally ranged from 66 to 76%, suggesting incomplete combustion of the fuel and oxidizer. These issues could likely be remedied in part through further optimization of the combustion chamber and injector design, however. In general, the fuel mass flow rates were much higher than expected based on earlier results obtained for EDBB-based fuel grains using this same hybrid combustor. Additionally, the regression rate of the AB-based fuels used here seemed to be independent of both the oxidizer mass flux and chamber pressure. The fuel mass flow rate instead appears to have been largely driven by the thermal decomposition of the AB, with the mass consumed for each test being on par with values expected for AB heated to approximately 200-250 ºC. Further study of the thermal profiles in the fuel grain during motor operation is necessary to confirm this, however.

8.2 Future work

Over the course of this broader research effort, several potential areas for future research were identified but were not pursued as part of this work due to time constraints or simply being beyond the scope of this work. If pursued, these potential avenues for future research would help build upon the work described throughout this document and provide additional information regarding ammonia borane based hypergolic fuels as well as the broader amine-borane family of fuels.

As discussed in chapter 4, phosphor thermography has been shown to be a viable means of measuring surface temperatures for burning solid propellants. While the experimental system used for this work was limited to 10 Hz repetition rates, this technique could also be adapted for use

with higher repetition rate laser/detector systems, significantly improving the temporal resolution of these measurements. This technique has recently been adapted for use with a burst-mode laser system capable of 10-100 kHz laser repetition rates [121]. These repetition rates would result in temporal resolutions of 0.1 and 0.01 milliseconds, respectively. For most practically viable hypergolic propellants, the fuel and oxidizer are rapidly heated to combustion temperatures generally within 10-20 milliseconds following contact between the two. Utilizing phosphor thermography in conjunction with burst-mode laser systems could enable new insights into the ignition dynamics of ammonia borane as well as hypergolic hybrid propellants in general.

As discussed in chapter 7, the fuel mass flow rate of the ammonia borane based fuels used here appears to be governed primarily by the thermal decomposition of the ammonia borane. As this behavior is fundamentally different from that of more conventional solid fuels used in hybrid rockets, further investigation of this behavior is warranted. As only a relatively small range of oxidizer mass fluxes and chamber pressures was investigated during the test campaign discussed in chapter 7, characterizing the behavior of these fuels across a wider range of operating conditions would help confirm or reject the theorized thermal decomposition governing mechanism. Supplementing these efforts with the use of an optically accessible hybrid rocket motor (such as the optical cylindrical combustor (OCC) utilized previously by Shark et al.) would allow for direct observation of the fuel grain under motor operating conditions [122].

Finally, methyl-substituted amine-boranes have been shown elsewhere to be highly soluble in methanol and other common solvents [123, 124]. To date, these materials have been investigated primarily for hydrogen storage applications. As such, the hypergolic nature of these materials has yet to be investigated. Given the high predicted solubility limits of these materials in methanol (56.6% for monomethylamine borane and 84.0% for dimethylamine borane), fuel solutions based

on these materials could serve as novel liquid hypergolic fuels that are less hazardous than the more conventional hydrazine-based fuels. In addition, it has been shown that eutectic solid mixtures of monomethylamine borane with ammonia borane can dramatically improve the solubility of these materials compared to either material alone [123, 124]. Given the high predicted performance of ammonia borane, this could help improve the predicted performance of these fuel solutions by both improving the overall AB mass fraction while also reducing the total solvent weight fraction. Given the low melting temperatures of these eutectic mixtures (approximately 38-42 ºC), there exists the potential to eliminate the use of lower energy solvents, assuming these materials are stable at these elevated temperatures. If sufficiently hypergolic and thermally stable, these MMAB-AB eutectic mixtures have the potential to serve as high performance fuels in both conventional hypergolic hybrid and liquid rocket systems, with predicted performance that rivals (or surpasses) the standard MMH-NTO hypergolic combination (as shown in Figure 51).

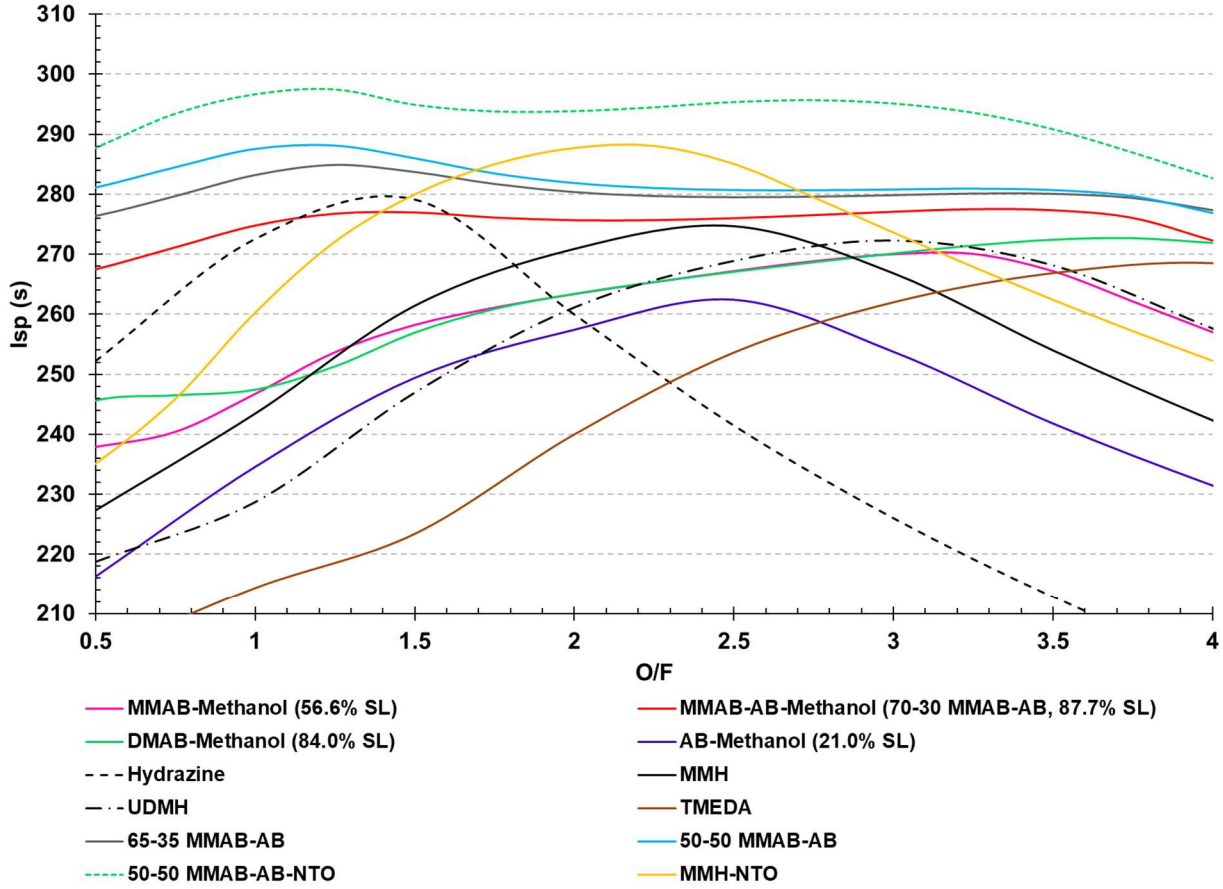

Figure 51: Predicted performance of various proposed hypergolic fuels based on methyl-substituted amine boranes (Note: all calculations performed with WFNA unless otherwise noted).

REFERENCES

[1.] Clark, J. D. *Ignition! An Informal History of Liquid Rocket Propellants*. New Brunswick, New Jersey: Rutgers University Press, 1972.

[2.] Ramachandran, P. V., Kulkarni, A. S., Pfeil, M. A., Dennis, J. D., Willits, J. D., Heister, S. D., Son, S. F., and Pourpoint, T. é. L. "Amine-Boranes: Green Hypergolic Fuels with Consistently Low Ignition Delays," *Chemistry: A European Journal* Vol. 20, No. 51, 2014, pp. 16869-16872.
doi: 10.1002/chem.201405224

[3.] Pfeil, M. A., Kulkarni, A. S., Ramachandran, P. V., Son, S. F., and Heister, S. D. "Solid Amine-Boranes as High-Performance and Hypergolic Hybrid Rocket Fuels," *Journal of Propulsion and Power* Vol. 32, No. 1, 2016, pp. 23-31.

[4.] Baier, M. J., Ramachandran, P. V., and Son, S. F. "Characterization of the Hypergolic Ignition Delay of Ammonia Borane," *Journal of Propulsion and Power* Vol. 35, No. 1, 2019, pp. 182-189.

[5.] Clements, K. A., Baier, M. J., Ramachandran, P. V., and Son, S. F. "An Experimental Study of Factors Affecting Hypergolic Ignition of Ammonia Borane," *AIAA Propulsion and Energy*. AIAA, Indianapolis, IN, 2019.

[6.] Connell Jr., T. L., Risha, G. A., Yetter, R. A., and Natan, B. "Investigation of Gel Hydrocarbon Fuels and Hydrogen Peroxide as a Hypergolic Bipropellant," *International Journal of Energetic Materials and Chemical Propulsion* Vol. 17, No. 1, 2018.

[7.] Pfeil, M. A. "Solid Amine-Boranes as High Performance Hypergolic Hybrid Rocket Fuels and their Combustion Behavior in a Hypergolic Hybrid Combustor." Vol. Doctor of Philosophy, Purdue University, West lafayette, IN, 2014, p. 234.

[8.] Gao, H., and Shreeve, J. M. "Ionic liquid solubilized boranes as hypergolic fluids," *Journal of Materials Chemistry* Vol. 22, No. 22, 2012, pp. 11022-11024.
doi: 10.1039/C2JM31627G

[9.] Dequasie, A. "The Green Flame: Surviving Government Secrecy." American Chemical Society, Washington, DC, 1991.

[10.] Rapp, L. R., and Strier, M. P. "The Effect of Chemical Structure on the Hypergolic Ignition of Amine Fuels," *Journal of Jet Propulsion* Vol. 27, No. 4, 1957, pp. 401-404.
doi: 10.2514/8.12793

[11.] Pfeil, M. A., Dennis, J. D., Son, S. F., Heister, S. D., Pourpoint, T. L., and Ramachandran, P. V. "Characterization of Ethylenediamine Bisborane as a Hypergolic Hybrid Rocket Fuel Additive," *Journal of Propulsion and Power* Vol. 31, No. 1, 2015, pp. 365-372.

[12.] Venkatesh, P. B., Back, C., Liberman, A., and Pourpoint, T. L. "Freezing Point Depression and its Effects on Density and Ignition Delay of Triethylamine Borane," *53 AIAA/SAE/ASEE Joint Propulsion Conference*. AIAA, Atlanta, GA, 2017.

[13.] Willits, J. D., Dennis, J. D., Kulkarni, A. S., Ramachandran, P. V., and Pourpoint, T. L. "Combustion Characterization of Amine Borane Hypergolic Propellants," *50th AIAA/ASME/SAE/ASEE Joint Propulsion Conference*. AIAA, Cleveland, OH, 2014.

[14.] Zarbo, N., Belal, H., and Pourpoint, T. L. "Effect of Water and Humidity on Hypergolic Propellant Ignition and Combustion," *AIAA Propulsion and Energy Forum*. AIAA, Orlando, Fl, 2015.

[15.] Peng, B., and Chen, J. "Ammonia borane as an efficient and lightweight hydrogen storage medium," *Energy & Environmental Science* Vol. 1, No. 4, 2008, pp. 479-483. doi: 10.1039/B809243P

[16.] Shore, S. G., and Parry, R. W. "The Crystalline Compound Ammonia-Borane, H3NBH3," *Journal of the American Chemical Society* Vol. 77, No. 22, 1955, pp. 6084-6085. doi: 10.1021/ja01627a103

[17.] Staubitz, A., Robertson, A. P. M., and Manners, I. "Ammonia-Borane and Related Compounds as Dihydrogen Sources," *Chemical Reviews* Vol. 110, No. 7, 2010, pp. 4079-4124. doi: 10.1021/cr100088b

[18.] Stephens, F. H., Pons, V., and Baker, R. T. "Ammonia-borane: the hydrogen source par excellence," *Dalton Transactions* Vol. 36, No. 25, 2007, pp. 2613-2626. doi: 10.1039/B703053C

[19.] Lee, J. G., Weismiller, M., Connell Jr., T. L., Rishia, G. A., Yetter, R. A., Gilbert, P. D., and Son, S. F. "Ammonia Borane Based-Propellants," *44th AIAA/ASME/SAE/ASEE Joint Propulsion Conference & Exhibit*. AIAA, Hartford, CT, 2008, p. 5037.

[20.] Weismiller, M. R., Connell Jr., T. L., Risha, G. A., and Yetter, R. A. "Characterization of Ammonia Borane (NH3BH3) Enhancement to a Paraffin Fueled Hybrid Rocket System," *46th AIAA/ASME/SAE/ASEE Joint Propulsion Conference & Exhibit*. AIAA, Nashville, TN, 2010.

[21.] Chiaverini, M. "Review of Solid-Fuel Regression Rate Behavior in Classical and Nonclassical Hybrid Rocket motors," *Fundamentals of Hybrid Rocket Combustion and Propulsion*. Vol. 218, American Institute of Aeronautics and Astronautics, Reston, VA, 2007, pp. 37-125.

[22.] Altman, D., and Holzman, A. "Overview and History of Hybrid Rocket Propulsion," *Fundamentals of Hybrid Rocket Combustion and Propulsion*. Vol. 218, American Institute of Aeronautics and Astronautics, Reston, VA, 2007, pp. 1-36.

[23.] Sutton, G. P., and Biblarz, O. *Rocket Propulsion Elements*. Hoboken, New Jersey: John Wiley & Sons, Inc., 2010.

[24.] Marxman, G., and Gilbert, M. "Turbulent boundary layer combustion in the hybrid rocket," *Proceedings of the Combustion Institute* Vol. 9, No. 1, 1963, pp. 371-383. doi: 10.1016/S0082-0784(63)80046-6

[25.] Muzzy, R. J. "Schlieren and Shadowgraph Studies of Hybrid Boundary-Layer Combustion," *AIAA Journal* Vol. 1, No. 9, 1963, pp. 2159-2160. doi: 10.2514/3.2017

[26.] Marxman, G. A., Wooldridge, C. E., and Muzzy, R. J. "Fundamentals of Hybrid Boundary-Layer Combustion," *Heterogeneous Combustion*. Vol. 15, American Institute of Aeronautics and Astronautics, New York, NY, 1963, pp. 485-522.

[27.] Muzzy, R. J. "Applied Hybrid Combustion Theory," *AIAA/SAE 8th Joint Propulsion Specialist Conference*. AIAA, New Orleans, LA, 1972, pp. 1-8.

[28.] Smoot, L. D., and Price, C. F. "Regression Rates of Nonmetalized Hybrid Fuel Systems," *AIAA Journal* Vol. 3, No. 8, 1965, pp. 1408-1413. doi: 10.2514/3.3160

[29.] Smoot, L. D., and Price, C. F. "Regression Rate Mechanisms of Nonmetalized Hybrid Fuel Systems," *2nd Aerospace Sciences Meeting*. AIAA, New York, NY, 1965, pp. 1-58.

[30.] Smoot, L. D., and Price, C. F. "Regression Rates of Metalized Hybrid Fuel Systems," *AIAA Journal* Vol. 4, No. 5, 1966, pp. 910-915. doi: 10.2514/3.3566

[31.] Smoot, L. D., and Price, C. F. "Pressure Dependence of Hybrid Fuel Regression Rates," *AIAA Journal* Vol. 5, No. 1, 1967, pp. 102-106. doi: 10.2514/3.3914

[32.] Smoot, L. D., Price, C. F., and Mihlfeith, C. M. "The Pressure Dependence of Hybrid Fuel Regression Rates," *3rd Aerospace Sciences Meeting*. AIAA, New York, NY, 1966, pp. 1-29.

[33.] Marxman, G. A. "Boundary-Layer combustion in propulsion," *Proceedings of the Combustion Institute* Vol. 11, No. 1, 1967, pp. 269-289. doi: 10.1016/S0082-0784(67)80153-X

[34.] Paul, P. J., Mukunda, H. S., Narahari, H. K., Venkataraman, R., and Jain, V. K. "Regression Rate Studies in Hypergolic System," *Combustion Science and Technology* Vol. 26, No. 1, 1981, pp. 17-24. doi: 10.1080/00102208108946942

[35.] Durgapal, U. C., and Chakrabarti, A. K. "Regression Rate Studies of Aniline Formaldehyde-Red Fuming Nitric Acid Hybrid System," *Journal of Spacecraft and Rockets* Vol. 11, No. 6, 1974, pp. 447-448.
doi: 10.2514/3.62102

[36.] Munjal, N. L., and Parvatiyar, M. G. "Regression Rate Studies of Metalized Aniline Formaldehyde Hybrid Fuel," *Journal of Spacecraft and Rockets* Vol. 13, No. 9, 1976, pp. 572-573.
doi: 10.2514/3.27928

[37.] George, P., Krishnan, S., Varkey, P. M., Ravindran, M., and Ramachandran, L. "Fuel regression rate enhancement studies in HTPB/GOX hybrid rocket motors," *34th AIAA/ASME/SAE/ASEE Joint Propulsion Conference & Exhibit*. AIAA/ASME/SAE/ASEE, Cleveland, OH, 1998.

[38.] Brübach, J., Pflitsch, C., Dreizler, A., and Atakan, B. "On surface temperature measurements with thermographic phosphors: A review," *Progress in Energy and Combustion Science* Vol. 39, 2013, pp. 37-60.
doi: 10.1016/j.pecs.2012.06.001

[39.] Allison, S. W., and Gillies, G. T. "Remote thermometry with thermographic phosphors: Instrumentation and applications," *Review of Scientific Instruments* Vol. 68, No. 7, 1997, pp. 2615-2650.
doi: 10.1063/1.1148174

[40.] Aldén, M., Omrane, A., Richter, M., and Särner, G. "Thermographic phosphors for thermometry: A survey of combustion applications," *Progress in Energy and Combustion Science* Vol. 37, No. 4, 2011, pp. 422-461.
doi: 10.1016/j.pecs.2010.07.001

[41.] Särner, G., Richter, M., and Aldén, M. "Investigations of blue emitting phosphors for thermometry," *Measurement Science and Technology* Vol. 19, 2008.
doi: 10.1088/0957-0233/19/12/125304

[42.] Särner, G., Richter, M., and Aldén, M. "Two-dimensional thermometry using temperature-induced line shifts of ZnO:Zn and ZnO:Ga fluorescence," *Optics Letters* Vol. 33, No. 12, 2008, pp. 1327-1329.
doi: 10.1364/OL.33.001327

[43.] Casey, A. D., Roberts, Z. A., Satija, A., Lucht, R. P., Meyer, T. R., and Son, S. F. "Dynamic imaging of the temperature field within an energetic composite using phosphor thermography," *Applied Optics* Vol. 58, No. 16, 2019, pp. 4320-4325.
doi: 10.1364/AO.58.004320

[44.] Goss, L. P., Smith, A. A., and Post, M. E. "Surface thermometry by laser-induced fluorescence," *Review of Scientific Instruments* Vol. 60, 1989.
doi: 10.1063/1.1140478

[45.] Vander wal, R. L., Householder, P. A., and Wright II, T. W. "Phosphor Thermometry in Combustion Applications," *Applied Spectroscopy* Vol. 53, No. 10, 1999, pp. 1251-1258.
doi: 10.1366/0003702991945498

[46.] Omrane, A., Ossler, F., and Aldén, M. "Two-dimensional surface temperature measurements of burning materials," *Proceedings of the Combustion Institute* Vol. 29, 2002, pp. 2653-2659.
doi: 10.1016/S1540-7489(02)80323-6

[47.] Omrane, A., Ossler, F., and Aldén, M. "Surface temperature measurement of flame spread using thermographic phosphors," *Fire Safety Science* Vol. 7, 2003, pp. 141-152.
doi: 10.3801/IAFSS.FSS.7-141

[48.] Omrane, A., Ossler, F., Aldén, M., Svenson, J., and Pettersson, J. B. C. "Surface temperature of decomposing construction materials studied by laser-induced phosphorescence," *Fire and Materials* Vol. 29, No. 1, 2005, pp. 39-51.
doi: 10.1002/fam.876

[49.] Omrane, A., Wang, Y. C., Göransson, U., Holmstedt, G., and Aldén, M. "Intumescent coating surface temperature measurement in a cone calorimeter using laser-induced phosphorescence," *Fire Safety Journal* Vol. 42, 2007, pp. 68-74.
doi: 10.1016/j.firesaf.2006.08.006

[50.] Ramachandran, P., and Kulkarni, A. "Water-promoted, safe and scalable preparation of ammonia borane," *International Journal of Hydrogen Energy* Vol. 42, No. 2, 2016, pp. 1451-1455.
doi: 10.1016/j.ijhydene.2016.06.231

[51.] Ramachandran, P. V., Mistry, H., Kulkarni, A. S., and Gagare, P. D. "Ammonia-mediated, large-scale synthesis of ammonia borane," *Dalton Trans.* Vol. 43, No. 44, 2014, pp. 16580-16583.
doi: 10.1039/C4DT02467B

[52.] Ramachandran, P. V., and Gagare, P. D. "Preparation of Ammonia Borane in High Yield and Purity, Methanolysis, and Regeneration," *Inorg. Chem.* Vol. 46, No. 19, 2007, pp. 7810-7817.
doi: 10.1021/ic700772a

[53.] Bernard, M. L., Cointot, A., Auzanneau, M., and Sztal, B. "The Role of Surface Reactions in Hypergolic Ignition of Liquid-Solid Systems," *Combustion and Flame* Vol. 22, No. 1, 1974, pp. 1-7.
doi: 10.1016/0010-2180(74)90002-9

[54.] Rajendran, G., and Jain, S. R. "Novel solid hypergolic fuels for hybrid propellants," *Fuel* Vol. 63, No. 5, 1984, pp. 709-712.
doi: 10.1016/0016-2361(84)90171-6

[55.] Bastea, S., Fried, L. E., Glaesemann, K. R., Howard, W. M., Kuo, I. F., Souers, P. C., and Vitello, P. A. "Cheetah Ver. 7.0." Lawrence Livermore National Laboratory, Livermore, CA, 2012.

[56.] Hill, P. G., and Peterson, C. R. *Mechanics and Thermodynamics of Propulsion*: Addison-Wesley Publishing Company, Inc., 1970.

[57.] Beckstead, M. W., Derr, R. L., and Price, C. F. "A model of composite solid-propellant combustion based on multiple flames," *AIAA Journal* Vol. 8, No. 12, 1970, pp. 2200-2207.
doi: 10.2514/3.6087

[58.] Klein, R., Mentser, M., Von Elbe, G., and Lewis, B. "Determination of the thermal structure of a combustion wave by fine thermocouples," *Journal of Physical and Colloid Chemistry* Vol. 54, No. 6, 1950, pp. 877-884.
doi: 10.1021/j150480a018

[59.] Sabadell, A. J., Wenograd, J., and Summerfield, M. "Measurement of temperature profiles through solid propellant flames using fine thermocouples," *AIAA Journal* Vol. 3, No. 9, 1965, pp. 1580-1584.
doi: 10.2514/3.3212

[60.] Suh, N. P., Tsai, C. L., Thompson Jr., C. L., and Moore, J. S. "Ignition and surface temperatures of double base propellants at low pressure: 1. Thermocouple Measurements," *AIAA Journal* Vol. 8, No. 7, 1970, pp. 1314-1321.
doi: 10.2514/3.5891

[61.] Zenin, A. "HMX and RDX: Combustion Mechanism and Influence on Modern Double-Base Propellant Combustion," *Journal of Propulsion and Power* Vol. 11, No. 4, 1995, pp. 752-758.
doi: 10.2514/3.23900

[62.] Powling, J., and Smith, W. A. W. "Measurement of the Burning Surface Temperatures of Propellant Compositions by Infra-red Emission," *Combustion and Flame* Vol. 6, No. 3, 1962, pp. 173-181.
doi: 10.1016/0010-2180(62)90087-1

[63.] Lengelle, G., Fourest, B., Godon, J. C., and Guin, C. "Condensed Phase Behavior and Ablation Rate of Fuels for Hybrid Propulsion," *AIAA/SAE/ASME/ASEE 29th Joint Propulsion Conference and Exhibit*. AIAA, Monterey, CA, 1993.

[64.] Thompson Jr., C. L., and Suh, N. P. "The Interaction of Thermal Radiation and M-2 Double-Base Solid Propellant," *Combustion Science and Technology* Vol. 2, No. 2, 1970, pp. 59-66.
doi: 10.1080/00102207008952235

[65.] Cohen, N. S., Fleming, R. W., and Derr, R. L. "Role of Binders in Solid Propellant Combustion," *AIAA Journal* Vol. 12, No. 2, 1974, pp. 212-218.
doi: 10.2514/3.49195

[66.] Khan, M. A., Allemand, C., and Eagar, T. W. "Noncontact temperature measurement. I. Interpolation based techniques," *Review of Scientific Instruments* Vol. 62, No. 2, 1991, pp. 392-402.
doi: 10.1063/1.1142133

[67.] Pourmortazavi, S. M., Hosseini, S. G., Rahimi-Nasrabadi, M., Hajimirsadeghi, S. S., and Momenian, H. "Effect of nitrate content on thermal decomposition of nitrocellulose," *Journal of Hazardous Materials* Vol. 162, 2009, pp. 1141-1144.
doi: 10.1016/j.jhazmat.2008.05.161

[68.] Abram, C., Fond, B., and Beyrau, F. "High-precision flow temperature imaging using ZnO thermographic phosphor tracer particles," *Optics Express* Vol. 23, No. 15, 2015, pp. 19453-19468.
doi: 10.1364/OE.23.019453

[69.] Huggett, C. "Combustion of Solid Propellants," *Combustion Processes*. Oxford University Press, London, 1956, pp. 514-576.

[70.] Robbins, F. W., and Keys, T. "The burning rate behavior of pure nitrocellulose propellant samples." U.S. Army Research Laboratory, USA, 1993.

[71.] Barrère, M. "Introduction to Nonsteady Burning and Combustion Stability," *Nonsteady Burning and Combustion Stability of Solid Propellants*. Vol. 143, AIAA, Washington DC, 1990, pp. 17-58.

[72.] Bruno, C., Riva, G., Zanotti, C., Dondè, R., Grimaldi, C., and De Luca, L. "Experimental and Theoretical Burning of Solid Rocket Propellants Near the Pressure Deflagration Limit," *Acta Astronautica* Vol. 12, No. 5, 1985, pp. 351-360.
doi: 10.1016/0094-5765(85)90069-4

[73.] Huffington, J. D. "The Burning and Structure of Cordite," *Transactions of the Faraday Society* Vol. 47, No. 1, 1951, pp. 864-876.
doi: 10.1039/TF9514700864

[74.] Huffington, J. D. "The Unsteady Burning of Cordite," *Transactions of the Faraday Society* Vol. 50, No. 1, 1954, pp. 942-952.
doi: 10.1039/TF9545000942

[75.] Svetlichnyi, I. B., Margolin, A. D., and Pokhil, P. F. "Low-Frequency Self-Oscillatory Processes in Propellant Combustion," *Combustion, Explosion and Shock Waves* Vol. 7, No. 2, 1971, pp. 156-161.
doi: 10.1007/BF00748964

[76.] Tang, C., Lee, Y., and Litzinger, T. A. "Simultaneous Temperature and Species Measurements During Self-Oscillating Burning of HMX," *Journal of Propulsion and Power* Vol. 15, No. 2, 1999, pp. 296-303.
doi: 10.2514/2.5427

[77.] Brewster, M. Q. "Solid Propellant Combustion Response: Quasi-Steady (QSHOD) Theory Development and Validation," *Solid Propellant Chemistry, Combustion, and Motor Interior Ballistics*. Vol. 185, AIAA, Reston, VA, 1999, pp. 607-638.

[78.] Miller, M. S. "Thermophysical Properties of Six Solid Gun Propellants." Army Research Laboratory, USA, 1997, pp. 1-25.

[79.] Dauerman, L., and Tajima, Y. A. "Thermal Decomposition and Combustion of Nitrocellulose," *AIAA Journal* Vol. 6, No. 8, 1968, pp. 1468-1473.
doi: 10.2514/3.4790

[80.] Ramachandran, P. V., Kulkarni, A. S., Pfeil, M. A., Dennis, J. D., Willits, J. D., Heister, S. D., Son, S. F., and Pourpoint, T. L. "Amine-Boranes: Green Hypergolic Fuels with Consistently Low Ignition Delays," *Chemistry: A European Journal* Vol. 20, No. 51, 2014, pp. 16869-16872.

[81.] Gagnon, M.-A., Tremblay, P., Savary, S., Farley, V., Mancaruso, E., and Sequino, L. "Chemical Imaging in a Diesel-Ignited Optical Engine Using High-Speed Infrared Narrowband Imaging," *Proceedings of the Combustion Institute - Canadian Section Spring Technical Meeting*. McGill University, Montréal, 2017.

[82.] Huot, A., Gagnon, M.-A., Lagueux, P., Farley, V., Chamberland, M., and Kastek, M. "Analysis of combustion reaction based on infrared multispectral imaging," *Measurement Automation Monitoring* Vol. 61, No. 6, 2015, pp. 165-168.

[83.] Khosravi, M., Rochussen, J., Yeo, J., Kirchen, P., McTaggart-Cowan, G., and Wu, N. "Effect of Fuelling Control Parameters on Combustion Characteristics of Diesel-Ignited Natural Gas Dual-Fuel Combustion in an Optical Engine," *2016 ASME Internal Combustion Engine Fall Technical Conference*. Greenville, SC, 2016.

[84.] Lagueux, P., Tremblay, P., Savary, S., Farley, V., Mancaruso, E., Sequino, L., Kastek, M., and Firmanty, K. "High-speed infrared imaging for analysis of a diesel engine supplied with a premixed methane-air charge," *Measurement Automation Monitoring* Vol. 63, No. 2, 2017, pp. 60-64.

[85.] Marcotte, F., DeChamplain, A., Jean, J., Fossi, A., and Ringuette, S. "Detailed Ignition Sequence Studied with a Fast Infrared Camera," *Proceedings of Combustion Institute-Canadian Section Spring Technical Meeting*. Université Laval, Quebec, 2013, pp. 285-290.

[86.] Rochussen, J., and Kirchen, P. "Characterization of reaction zone growth in an optically accessible heavy-duty diesel/methane dual-fuel engine," *International Journal of Engine Research* Vol. 20, No. 5, 2019, pp. 483-500.

[87.] Xie, S., Song, Y., and Liu, Z. "In situ high-pressure study of ammonia borane by Raman and IR spectroscopy," *Canadian Journal of Chemistry* Vol. 87, No. 9, 2009, pp. 1235-1247.

[88.] Zhang, J., Zhao, Y., Akins, D. L., and Lee, J. W. "Thermal Decomposition and Spectroscopic Studies of Preheated Ammonia Borane," *Journal of Physical Chemistry* Vol. 114, No. 45, 2010, pp. 19529-19534.

[89.] Pearse, R. W. B., and Gaydon, A. G. *The Identification of Molecular Spectra*. London: Chapman and Hall, 1950.

[90.] Spalding, M. J., Krier, H., and Burton, R. L. "Boron Suboxides Measured During Ignition and Combustion of Boron in Shocked Ar/F/O2 and Ar/N2/O2 mixtures," *Combustion and Flame* Vol. 120, No. 1-2, 2000, pp. 200-210.

[91.] Karmakar, S., Acharya, S., and Dooley, K. M. "Combustion of Boron Nano-Particles in Ethanol Spray Flame," *Proceedings of the ASME 2010 International Mechanical Engineering Congress & Exposition*. Vol. 5, Vancouver, British Columbia, Canada, 2010, pp. 691-698.

[92.] White, D., Walsh, P. N., and Mann, D. E. "Infrared Emission Spectra of B2O3(g) and B2O2(g)," *The Journal of Chemical Physics* Vol. 28, No. 3, 1958, pp. 508-509. doi: https://doi.org/10.1063/1.1744169

[93.] Hanst, P. L., Early, V. H., and Klemperer, W. "Infrared Spectrum and Molecular Structure of B2O3," *The Journal of Chemical Physics* Vol. 42, No. 3, 1965, pp. 1097-1104.

[94.] Kawashima, Y., Endo, Y., Kawaguchi, K., and Hirota, E. "Detection and Equilibrium Molecular Structure of a Short-Lived Molecule, HBO, by Microwave Spectroscopy," *Chemical Physics Letters* Vol. 135, No. 4-5, 1987, pp. 441-445.

[95.] Lory, E. R., and Porter, R. F. "Infrared Spectrum of Matrix-Isolated HBO," *Journal of the American Chemical Society* Vol. 93, No. 23, 1971, pp. 6301-6302.

[96.] White, D., Mann, D. E., Walsh, P. N., and Sommer, A. "Infrared Emission Spectrum of Gaseous HBO2," *The Journal of Chemical Physics* Vol. 32, No. 2, 1960, pp. 488-492.

[97.] Ramachandran, P., and Kulkarni, A. "Water-promoted, safe and scalable preparation of ammonia borane," *International Journal of Hydrogen Energy*, 2016.

[98.] Johns, J. W. C. "The Absorption Spectrum of BO2," *Canadian Journal of Physics* Vol. 39, No. 12, 1961, pp. 1738-1768.

[99.] Yetter, R. A., Rabitz, H., Dryer, F. L., Brown, R. C., and Kolb, C. E. "Kinetics of High-Temperature B/O/H/C Chemistry," *Combustion and Flame* Vol. 83, No. 1-2, 1991, pp. 43-62.

[100.] Connell Jr., T. L., Risha, G. A., Yetter, R. A., Roberts, C. W., and Young, G. "Boron and Polytetrafluoroethylene as a Fuel Composition for Hybrid Rocket Applications," *Journal of Propulsion and Power* Vol. 31, No. 1, 2015, pp. 373-385.

[101.] Young, G., Stoltz, C. A., Mayo, D. H., Roberts, C. W., and Milby, C. L. "Combustion Behavior of Solid Fuels Based on PTFE/Boron Mixtures," *Combustion Science and Technology* Vol. 183, No. 8, 2013, pp. 1261-1280.

[102.] Glassman, I., and Yetter, R. A. *Combustion*: Academic Press, 2008.

[103.] Hollingshead, J. M., Litzinger, M., Kiaoulias, D., Eckenrode, L. M., Moore, J. D., Risha, G. A., and Yetter, R. A. "Combustion of a TMEDA/WFNA Hypergolic in a Bipropellant Rocket Engine," *AIAA Propulsion and Energy Forum*. AIAA, Indianapolis, IN, 2019.

[104.] Stevenson, W. H., Felton, L. D., and Slocum-Wang, Z. "Hypergolic Liquid or Gel Fuel Mixtures." United States of America, 2008, pp. 1-14.

[105.] Bittner, D. E., Sell, J. L., and Risha, G. A. "Effect of Jet Momentum Ratio and Equivalence Ratio on the Ignition process of TMEDA and White Fuming Nitric Acid (WFNA)," *49th AIAA/ASME/SAE/ASEE Joint Propulsion Conference*. AIAA, San Jose, CA, 2013, pp. 1-12.

[106.] McQuaid, M. J., and Chen, C.-c. "BH3-Amine and B(CH3)3-Amine Adducts as Additives for Liquid/Gel Hypergols and Solid Hybrid Rocket Motor Fuels: Property and Performance Predictions." Army Research Laboratory, 2013.

[107.] Gao, H., and Shreeve, J. n. M. "Ionic liquid solubilized boranes as hypergolic fluids," *Journal of Materials Chemistry*, No. 22, 2012, pp. 11022-11024.

[108.] Clements, K. A., Baier, M. J., Ramachandran, P. V., and Son, S. F. "Experimental Study of Factors Affecting Hypergolic Ignition of Ammonia Borane," *Journal of Propulsion and Power*, 2020, pp. 1-9.
doi: 10.2514/1.B37976

[109.] Li, S., Gao, H., and Shreeve, J. n. M. "Borohydride Ionic Liquids and Borane/Ionic-Liquid Solutions as Hypergolic Fuels with Superior Low Ignition-Delay Times," *Angewandte Chemie* Vol. 126, No. 11, 2014, pp. 3013-3016.
doi: 10.1002/ange.201309044

[110.] Chitsaz, S., Breyhan, T., Pauls, J., and Neumüller, B. "Crystal Structures of TMEDA Adducts and of Salts with Protonated TMEDAMolecules," *Zeitschrift für anorganische und allgemeine Chemie* Vol. 628, No. 5, 2002, pp. 956-964.

[111.] Gordon, S., and McBride, B. J. "Computer Program for Calculation of Complex Chemical Equilibrium Compositions and Applications I. Analysis." 1994.

[112.] McBride, B. J., and Gordon, S. "Computer Program for Calculation of Complex Chemical Equilibrium Compositions and Applications II. Users Manual and Program Description." 1996.

[113.] McQuaid, M. J., Stevenson, W. H., and Thompson, D. M. "Computationally Based Design and Screening of Hypergolic Multiamines." US Army Research Laboratory, Aberdeen Proving Ground, MD, 2004.

[114.] Solomon, Y., DeFini, S. J., Pourpoint, T. L., and Anderson, W. E. "Gelled Monomethyl Hydrazine Hypergolic Droplet Investigation," *Journal of Propulsion and Power* Vol. 29, No. 1, 2013, pp. 79-86.
doi: 10.2514/1.B34634

[115.] Dennis, J. D., Willits, J. D., and Pourpoint, T. L. "Performance of neat and gelled monomethylhydrazine and red fuming nitric acid in an unlike-doublet combustor," *Combustion Science and Technology* Vol. 190, No. 7, 2018, pp. 1141-1157.
doi: 10.1080/00102202.2018.1428571

[116.] Mordosky, J. W., Zhang, B. Q., Kuo, K. K., Tepper, F., and Kaledin, L. A. "Spray combustion of gelled RP-1 propellants containing nano-sized aluminum particles in rocket engine conditions," *37th AIAA/ASME/SAE/ASEE Joint Propulsion Conference and Exhibit*. AIAA, Salt Lake City, Utah, 2001, pp. 1-11.

[117.] Sabourin, J. L., Yetter, R. A., Asay, B. W., Lloyd, J. M., Sanders, V. E., Risha, G. A., and Son, S. F. "Effect of Nano-Aluminum and Fumed Silica Particles on Deflagration and Detonation of Nitromethane," *Propellants, Explosives, Pyrotechnics* Vol. 34, No. 5, 2009, pp. 385-393.
doi: 0.1002/prep.200800106

[118.] Yetter, R. A., Risha, G. A., and Son, S. F. "Metal particle combustion and nanotechnology," *Proceedings of the Combustion Institute* Vol. 32, No. 2, 2009, pp. 1819-1838.
doi: 10.1016/j.proci.2008.08.013

[119.] Randall, L. N. "Rocket Applications of the Cavitating Venturi," *Journal of the American Rocket Society* Vol. 22, No. 1, 1952, pp. 28-38.
doi: 10.2514/8.4412

[120.] Frueh, S., Kellett, R., Mallery, C., Molter, T., Willis, W. S., King'ondu, C., and Suib, S. L. "Pyrolytic decomposition of ammonia borane to boron nitride," *Inorg Chem* Vol. 50, No. 3, 2011, pp. 783-92.
doi: 10.1021/ic101020k

[121.] Ayers, Z., Fisher, J., Brown, A., Son, S. F., and Meyer, T. R. "kHz-Rate Temperature Imaging Using Time-Domain Thermographic Phosphorescence," *AIAA Scitech 2019 forum*. AIAA, San Diego, CA, 2019, pp. 1-6.

[122.] Shark, S. C., Zaseck, C. R., Graham Jr., J. T., Pourpoint, T. L., Son, S. F., and Heister, S. D. "Visualization and Performance of Hybrid Rocket Solid Fuels in an Optical Cylindrical Combustor," *49th AIAA/ASME/SAE/ASEE Joint Propulsion Conference*, 2013.

[123.] Confer, M. P., DeSimone, A., Burnham, H., McLeod, W., Klein, T. M., Street, S. C., and Dixon, D. A. "Solubility thermodynamics of amine boranes in polar solvents," *International Journal of Hydrogen Energy* Vol. 46, No. 18, 2021, pp. 10801-10808.
doi: 10.1016/j.ijhydene.2020.12.163

[124.] Grant, D. J., Matus, M. H., Anderson, K. D., Camaioni, D. M., Neufeldt, S. R., Lane, C. F., and Dixon, D. A. "Thermochemistry for the dehydrogenation of methyl-substituted ammonia borane compounds," *J Phys Chem A* Vol. 113, No. 21, 2009, pp. 6121-32.
doi: 10.1021/jp902196d

PUBLICATIONS

1. M. J. Baier, P. V. Ramachandran, S. F. Son, "Characterization of the hypergolic ignition delay of ammonia borane" *Journal of Propulsion and Power* Vol. 35, No. 1
2. M. J. Baier, A. Satija, A. Casey, R. P. Lucht, S. F. Son, "Surface Temperature Measurements of Burning Solid Propellants Using Phosphor Thermography" *Journal of Propulsion and Power* Vol. 36, No. 5
3. M. J. Baier, A. J. McDonald, K. A. Clements, C. S. Goldenstein, S. F. Son, "High-Speed Multi-Spectral Imaging of the Hypergolic Ignition of Ammonia Borane" *Proceedings of the Combustion Institute* Vol. 38, No. 3
4. K. A. Clements, M. J. Baier, P. V. Ramachandran, S. F. Son, "An Experimental Study of Factors Affecting Hypergolic Ignition of Ammonia Borane" *Journal of Propulsion and Power* Vol. 37, No. 2
5. G. Young, T. L. Connell Jr., K. Fennell, S. Possehl, M. Baier, "Examining Port Geometry/Solid Loading for Additively Manufactured Fuels in Hybrid Rockets" *Journal of Propulsion and Power* Vol. 37, No. 2
6. M. J. Baier, C. M. Jarocki, A. R. Noel, K. A. Clements, S. F. Son, "Performance of Ammonia Borane-based fuels in Hypergolic Hybrid Rocket Motors" *Journal of Propulsion and Power* (**Draft in Progress**)
7. M. J. Baier, C. M. Jarocki, A. R. Noel, S. F. Son, "Performance Enhancement and Ignition Delay Suppression of TMEDA using Amine-Borane Additives" *International Journal of Energetic Materials and Chemical Propulsion* (**Final edits underway before submission**)

Conference publications

8. Connell Jr., T. L., Young, G., Beckett, K., Gumm, C., Gonzàlez, D., Baier, M., "Enhanced Solid Fuel Regression in a Hybrid Rocket Employing Additively Manufactured Fuels Exhibiting Novel Grain Port Geometries" *AIAA Scitech 2019 Forum,* 2019
9. Clements, K. A., Baier, M. J., Ramachandran, P. V., Son, S. F., "An Experimental Study of Factors Affecting Hypergolic Ignition of Ammonia Borane" *AIAA Propulsion and Energy 2019 Forum,* 2019
10. M. J. Baier, A. J. McDonald, K. A. Clements, C. S. Goldenstein, S. F. Son, "High-Speed Multi-Spectral Imaging of the Hypergolic Ignition of Ammonia Borane" *38th International Symposium on Combustion,* January 24-29th 2021
11. M. J. Baier, A. R. Noel, S. F. Son, "Performance Enhancement and Ignition Delay Suppression of TMEDA using Amine-Borane Additives" *12th International Symposium on Special Topics in Chemical Propulsion & Energetic Materials,* March 22-25th 2021

APPENDIX A: HYBRID COMBUSTOR PLUMBING AND INSTRUMENTATION DIAGRAM

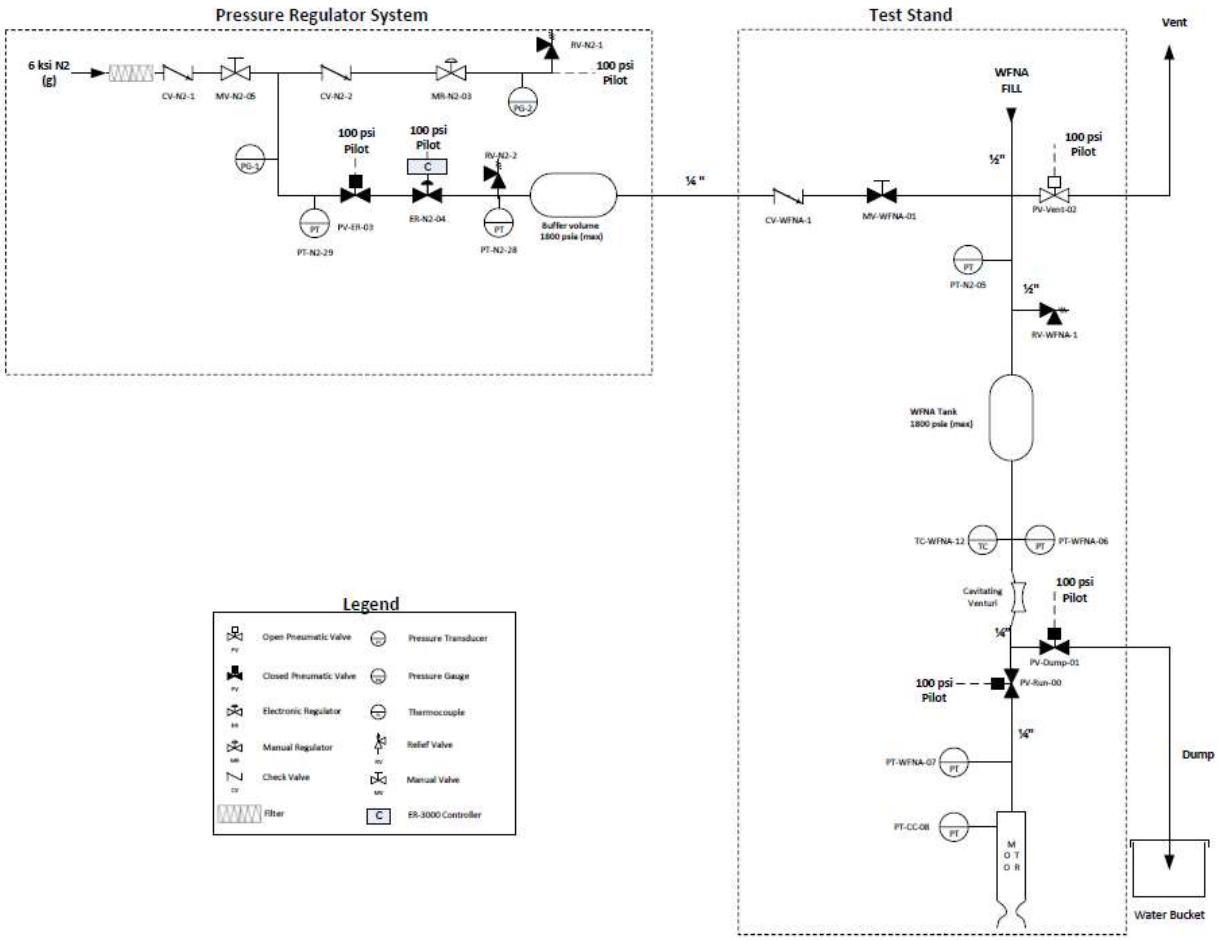

Figure A.1: Plumbing and instrumentation diagram used for hypergolic hybrid rocket motor

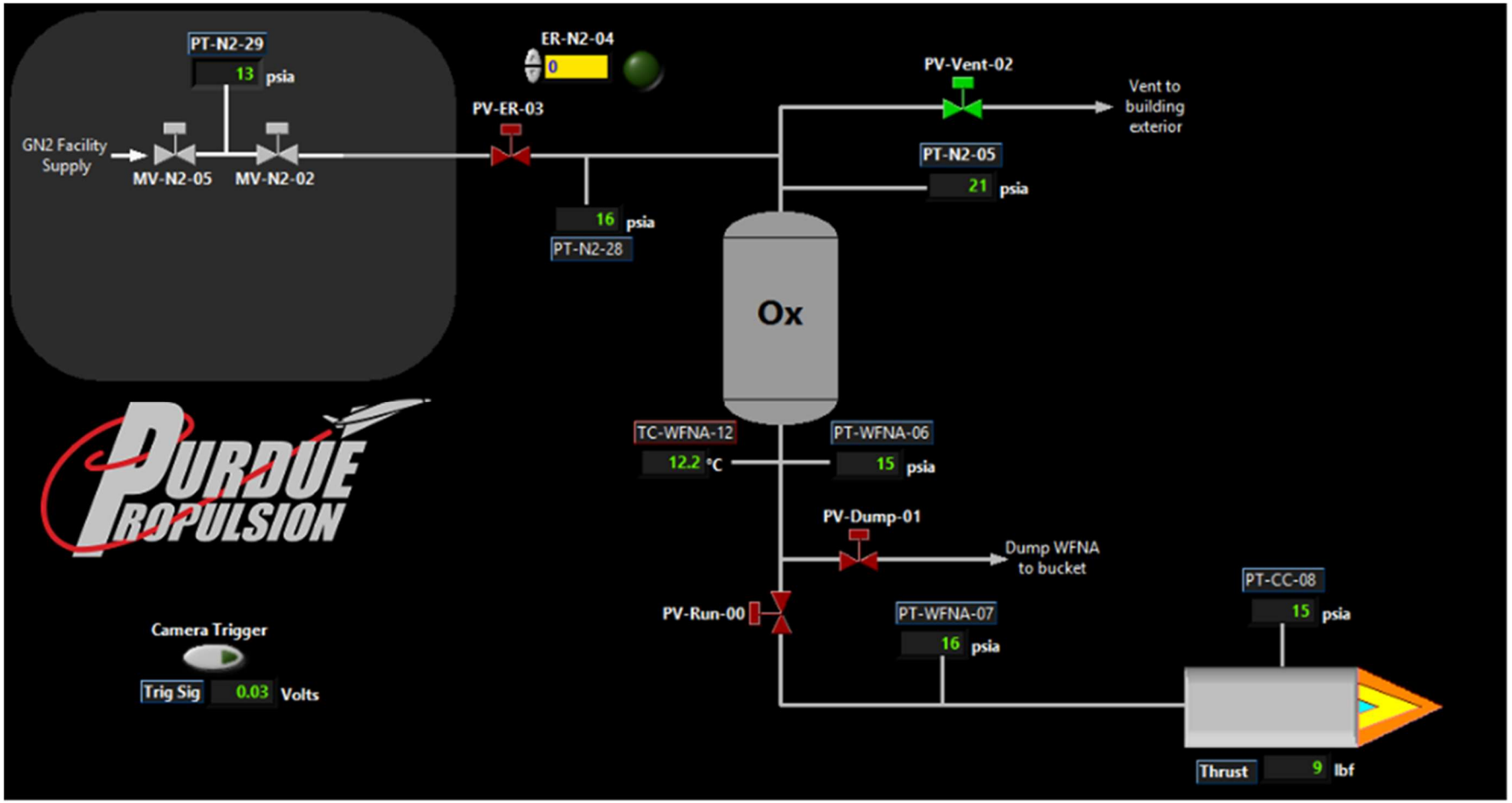

Figure A.2: Labview VI used to run hypergolic hybrid motor tests

Instrument Cable Number	T-Cell Patch Number	DAQ designation	Description	Fluid	Input voltage		Manufacturer
					Min	Max	
PV-Run-00	DO-20	SC1Mod5/port0/line20	WFNA run valve	WFNA	0	24	Habonim/El-O-Matic/Versa
PV-Dump-01	DO-21	SC1Mod5/port0/line21	WFNA dump valve	WFNA	0	24	Habonim/El-O-Matic/Versa
PV-Vent-02	DO-22	SC1Mod5/port0/line22	N2 vent valve	N2/WFNA fumes	0	24	Habonim/El-O-Matic/Versa
PV-ER-03	DO-5	SC1Mod5/port0/line5	N2 electronic regulator isolation valve	N2	0	24	Habonim/El-O-Matic/Versa
ER-N2-04	AO-1	SC1Mod6/ao1	N2 electronic regulator	N2	0	10	Tescom
PT-N2-05	AI-10	SC1Mod2/ai10	Oxidizer tank/ullage pressure	N2	8	30	Druck
PT-WFNA-06	AI-09	SC1Mod2/ai9	Cavitating venturi upstream pressure	WFNA	8	30	Druck
PT-WFNA-07	AI-11	SC1Mod2/ai11	Injector upstream pressure	WFNA	14	32	Stellartech
PT-CC-08	AI-12	SC1Mod2/ai12	Combustion chamber pressure	Combustion gases	8	30	Druck
PT-N2-28	AI-23	SC1Mod1/ai23	N2 electronic regulator feedback pressure	N2	8	30	Druck
PT-N2-29	AI-01	SC1Mod1/ai1	Bulk N2 pressure	N2	8	30	Druck
TC-WFNA-12	TC-WFNA-12	SC1Mod3/ai12	Cavitating venturi upstream temperature	WFNA	N/A	N/A	Omega
Camera Trigger	DO-15	SC1Mod5/port0/line15	Camera trigger	N/A	0	5	N/A
Load cell	AI-18	SC1Mod2/ai17	Load cell	N/A	0	20	Interface

Figure A.3: Instrumentation and valve list for hypergolic hybrid motor flow system

APPENDIX B: HYPERGOLIC HYBRID ROCKET MOTOR TEST PROCEDURES

WFNA hybrid motor test procedures

Originator: Michael Baier
Responsible Professor: Steven Son
Authorized: Michael Baier

TABLE OF CONTENTS

Hazards, Mitigation, and PPE
1: High Pressure System: Safety glasses, face shield, fencing, remote operation, burn, warning signs
2: WFNA Handling: Nitrile gloves, safety glasses, face shield, tyvek coveralls with boots, water hose safety shower, arm protectors, over gloves
3: Fire Hazard: Fire extinguisher, face shield, water hose
4: Hazardous solid fuels: safety glasses, nitrile gloves, lab coat

Acronyms	
TC	Test Conductor: In charge of all aspects of the test. Directs test operations through use of the test procedures
TOP	Test Operator: Performs all test stand related activities associated with loading propellants and pressurant gases. Receives instructions from the Test Conductor during operation of the test procedures.
DSO	Data System Operator: Responsible for the installation and operability of all instrumentation and controls consistent with the requirements for each test. Operates the computer control and data acquisition system during tests
SAF	Site Safety: Responsible for insuring all test site safety equipment is in place and functioning properly. Is Responsible for keeping the site clear of unauthorized personnel during test operations
Motor Operations	

At least three people must be present during testing operations. If only three people are present, the DSO and SAF duties can be satisfied by one person. During propellant loading/unloading procedures, two test personnel must be present in the test cell while a third (i.e. the DSO/SAF) monitors from the control room.

Coordinate with those performing experiments in ZL6 and the blast room in ZL4 to ensure people are not using that building during motor operation

SECTION 1: PRE-Test Checklist				REQ'D PERSONNEL: TC, TOP, SAF, DSO PPE: Gloves, Safety Glasses, Lab coat					
1.000		SAF	Verify access to the safety shower and flush until clean water flows from shower						
1.001		SAF	Verify CO2 fire extinguisher is in place in test cell hall way						
1.002		SAF	Verify garden hose w/spray nozzle is in place in t-cell and pressurized with water						
1.003		SAF	Verify stepladder is present in test cell						
1.004		TC	Verify all test plans are present and complete						
1.005		TC	Verify the test article is installed per the test plan and the appropriate drawings						
1.006		DSO	Verify instrumentation and controls are patched per test plan						
1.007		DSO	Start control room computer (if not currently running)						

1.008		DSO	Turn on SCXI chasis						
1.009		DSO	Run T-cell main labview VI						
1.010		DSO	Load DAQ labview configuration file						
1.011		DSO	Load and acquire on analog inputs						
1.012		DSO	Load Controls labview configuration file						
1.013		DSO	Open WFNA hybrid labview schematic						
1.014		DSO	Turn on valve and instrumentation power						
1.015		DSO	Verify all data channels are reading properly						
1.016		DSO	Verify ER3000 set pressure is set to 0 psia						
1.017		TOP	Verify cameras and visual instrumentation are in position and functioning properly by triggering using labview VI						
1.018			**Place all manually controlled valves and regulators in the proper pre-test positions**						
1.019		TOP	Open t-cell garage door						
1.020		TOP	Ensure all manual pressure regulators (MR-N2-01, MR-N2-02, and MR-N2-03) are unloaded						
1.021		TOP	Verify isolation valve on left test stand coming off main pressurization stand is closed						
1.022		TOP	Slowly open System nitrogen supply pressure manual valve MV-N2-05 to pressurize system						
1.023		TOP	LOAD Pneumatic valve actuation supply pressure regulator MR-N2-03 to 100 psig						
1.024		TOP	OPEN test stand manual isolation valve MV-WFNA-1						
1.025		TOP	Verify the nitrogen supply pressure is at least 2500 psi and matches bulk N2 supply pressure on gauge outside of test cell						
1.026		TOP	Check Pneumatic valve actuation supply pressure (MR-N2-03) to ensure it is set to 100 psig						
1.027			**Verify remote controlled valves are functioning correctly**						
1.028		TOP/DSO	Cycle WFNA run valve PV-Run-00						
1.029		TOP/DSO	Cycle WFNA dump valve PV-Dump-01						
1.030		TOP/DSO	Cycle WFNA vent valve PV-Vent-02						
1.031		TOP/DSO	Cycle N2 electronic regulator isolation valve PV-ER-03						
1.032			**Note: proper valve function is checked by listening for this valve to cycle or by checking visually**						
1.033			**Verify all remote controlled valves are in their correct power off position**						
1.034		TOP/DSO	Verify WFNA run valve PV-Run-00 **CLOSED**						
1.035		TOP/DSO	Verify WFNA dump valve PV-Dump-01 **CLOSED**						
1.036		TOP/DSO	Verify WFNA vent valve PV-Vent-02 **OPEN**						
1.037		TOP/DSO	Verify N2 electronic regulator isolation valve PV-ER-03 **CLOSED**						
1.038		TOP	CLOSE test stand manual isolation valve MV-WFNA-1						
1.039		TOP	Position 5 gallon bucket filled with water under line downstream of WFNA Dump valve PV-Dump-01						
SECTION 2: Fuel Grain Loading				REQ'D PERSONNEL: TC, TOP, SAF					
				PPE: Safety glasses, nitrile gloves, Lab coat, Face shield					
			NOTE: Personnel entering test cell should wear PPE appropriate for handling fuel grains						
2.000		SAF	Clear t-cell of all unneccesary personnel and close t-cell hallway door						
2.001		SAF	Turn on outside and inside warning lights						
2.002		TC	Verify the nozzle and venturi match the current test plan, record venturi and nozzle throat/exit diameters on test data sheet						
2.003		TOP	Ensure correct O-rings are installed on graphite nozzle for current test and properly lubricated						
2.004		TOP	Attach aft motor section to main motor section using **grade 8 bolts and grade 8 nuts**, torque bolts to 96 in-lbf						
2.005		TOP	Sand fuel grain port with 100 grit sand paper in fume hood						
2.006		TOP/TC	Weigh fuel grain/phenolic and measure I.D. of fuel grain center port, record on test data sheet						
2.007		TOP	Insert fuel grain into main motor chamber, ensuring that the head end of the phenolic tube is flush with the injector plate (Note: the head end of the fuel grain should be the one with the fuel grain recessed 0.25 inches from the end of the phenolic tube)						
2.008		TOP	Add RTV silicone to forward and aft lips of post combustion chamber						
2.009		TOP	Mate head end lip of post combustion chamber with aft end lip of phenolic tube, align drilled hole in post combustion chamber with port in aft motor section for chamber pressure transducer, clean excess RTV						
2.010		TOP	Insert head end lip of graphite nozzle into aft end lip of post combustion chamber						
2.011		TOP	Verify nozzle retainer plate seal o-rings are in place and coated with vacuum grease						

2.012		TOP	Attach nozzle retainer plate to aft motor section using grade 5 bolts and grade 8 nuts, torque bolts to 96 in-lbf						
2.013		TOP	Position rocket motor exhaust guide pipe at exit of rocket motor						
2.014		TOP	Place water sheet generator at exit of rocket motor exhaust guide pipe, attach water hoses						
2.015		DSO	Acquire zero data						
SECTION 3: Oxidizer Loading				REQ'D PERSONNEL: TC, TOP, SAF, DSO PPE: Safety glasses, nitrile gloves, Tyvek coveralls w/boots, positive pressure hood, over gloves, arm protectors, NO2 detector					
3.000		TOP	Loosen 1/2" AN fitting above main WFNA tank						
3.001		SAF	Ensure a water hose with a spray nozzle is connected to a water faucet, pressurized, and ready for use in case of an oxidizer spill						
3.002		TOP	Place a 5 gallon bucket with water next to test stand						
3.003		TOP	Open door in t-cell control to outside of building						
3.004		TOP	Place large industrial fan inside t-cell and turn on to induce flow from front of building out through test cell garage door						
3.005			**Oxidizer Handling/Loading**						
3.006		TOP	Prop open door from t-cell hallway to outside of ZL4 at the rear of the building						
3.007		SAF	Exit the building and ensure no personnel are performing any work outside near the south side of ZL-4 or north east side of ZL-1						
3.008		SAF	Place warning signs outside behind burm and next to t-cell						
3.009		SAF	Secure chains in area outside of test cell (Chain 1: between burm and shipping container, Chain 2: between shipping container and ZL4)						
3.010		SAF	Turn on interior and exterior T-cell warning lights						
3.011		TOP/TC	Don proper PPE for handling of nitric acid including Tyvek suit, appropriate large over boots, nitrile gloves, safety glasses, face shield, chemical resistant over gloves, and arm protectors						
3.012		TOP/TC	Place graduated cylinder appropriate for amount of oxidizer needed for current test in ZL4 115B fume hood						
3.013		TOP/TC	Position step ladder near main WFNA tank for use during pour filling						
3.014		TOP/TC	Obtain WFNA bottle from ZL4 115B fridge and carefully move into 115B fume hood **Note:** if bottle has not been opened before, open first in fume hood behind barrier to protect test personnel in case the bottle has self-pressurized						
3.015		TOP/TC	Slowly open the oxidizer bottle lid and carefully measure out the amount of oxidizer needed for test into graduated cylinder, record volume of oxidizer on test data sheet, carefully apply parafilm to open end of graduated cylinder.						
3.016		TOP/TC	Replace lid on oxidizer bottle, wipe down bottle exterior with kim-wipes wetted with DI water, dry and place in ziploc bag, and return bottle to 115B fridge						
3.017		TOP/TC	Exit the building with the WFNA graduated cylinder and carefully walk along the exterior of ZL4 to the test cell. Carefully place the graduated cylinder on the table in test cell.						
3.018		TOP/TC	Rinse and dry gloves with water and shop towels						
3.019		TOP/TC	Don positive pressure hoods and connect to supplied air lines in T-cell hallway						
3.020		SAF	Turn on supplied air pump in ZL4 entry hallway						
3.021		TOP/TC	When ready to load oxidizer, lift the loosened tubing from the AN fitting above oxidizer tank and secure with bungie straps						
3.022		TOP/TC	Insert glass funnel in open fitting on upstream side of main WFNA tank						
3.023		TOP/TC	Verify Run valve (PV-Run-00) and Dump valve (PV-Dump-01) are both closed						
3.024		TOP/TC	Operator 1: stand on step ladder if necessary to ensure that WFNA is not being poured at eye level, Operator 2: take graduated cylinder from table and carefully pass to operator 1. Ensure spray nozzle and hose is ready for use in the event of oxidizer spill						
3.025		TOP/TC	Operator 1: Remove parafilm from opening of graduated cylinder and **SLOWLY** pour WFNA from graduated cylinder into glass funnel, making sure to not overfill funnel while the WFNA flows from the funnel into tank. Once fully transferred to tank, pass graduated cylinder to operator 2. Operator 2: carefully submerge and rinse graduated cylinder in 5 gallon bucket filled with water						
3.026		TOP/TC	Remove glass funnel from main WFNA tank, rinse with DI water to remove any residual WFNA, place carefully in water bucket						
3.027		TOP/TC	Clean up any spilled oxidizer with a kim wipe and put in an appropriate water source for later neutralization						
3.028		TOP/TC	Rinse gloves in 5 gallon bucket of water, dry gloves with kim wipes/ shop towels and collect waste for later neutralization/disposal						
3.029		TOP/TC	Disconnect bungie straps, lower upper tubing assembly onto 1/2" AN fitting on upper end of WFNA tank and carefully tighten fitting with wrench						

3.030		TOP/TC	Wipe down tubing exterior with kimwipe and DI water and place kimwipe in appropriate water source						
3.031		TOP/TC	Check for leaks and/or smoke coming from the motor chamber.						
3.032		TOP/TC	Rinse gloves in 5 gallon bucket of water, dry with shop towels						
3.033			**Note: From this point until the conclusion of the current test, all personnel should remain clear of the area between the motor and burm**						
3.034		TOP	OPEN test stand manual isolation valve MV-WFNA-1						
3.035		SAF	Clear all remaining personnel from T-Cell						
3.036		SAF	Close door from T-cell hallway to rear side of building (i.e. towards the burm)						
3.037		TOP	Turn on water to water sheet generator						
3.038		SAF	Turn off positive pressure pump						
3.039		SAF	Exit T-cell, close T-cell door and place safety chain in T-cell hallway						
3.040		TOP/TC	PPE for loading oxidizer may now be removed						
Section 4: Motor Test Firing				REQ'D PERSONNEL: TC, TOP, SAF, DSO PPE: Gloves, Goggles, Lab coat, Face Shield, hearing protection					
4.000		DSO	Verify camera settings/operating properly						
4.001		SAF	Ensure that no one is in the blast room and place safety chain in front of blast room door						
4.002		SAF	Place safety chain in front of door to T-cell hallway, Close the door that separates the T-cell and T-cell control room from the rest of ZL-4						
4.003		DSO	Ready phantom cameras by pressing capture in control software						
4.004		DSO	CLOSE vent valve PV-Vent-02						
4.005		DSO	OPEN N2 electronic regulator isolation valve PV-ER-03						
4.006		SAF	Exit the building and make certain the test area is clear (**keeping clear of area between motor and burm**)						
4.007		DSO	START acquiring data in labview VI						
4.008		SAF	Sound warning siren						
4.009			**Verify all personnel present have appropriate hearing protection**						
4.010		DSO	SET ER3000 set pressure in labview VI to desired test condition						
4.011		DSO	**Note:** if set pressure overshoots due to presence of check valve, cycle vent valve PV-Vent-02 until system reaches desired pressure						
4.012		TC	Verify venturi inlet pressure corresponds to desired test condition via PT-WFNA-06						
4.013		DSO	**WHEN READY TO PERFORM TEST:** OPEN WFNA run valve PV-Run-00						
4.014		DSO	Upon completion of test (when motor quenches/WFNA is fully consumed), SET ER3000 to purge pressure (300 psia), stop recording data, keep WFNA run valve PV-Run-00 open for 10 minutes to purge residual WFNA/WFNA fumes						
4.015			**NOTE: in the event of EXPLOSION or FAILURE of the test article, OPEN the WFNA dump valve PV-Dump-01 to dump remaining WFNA into 5 gallon bucket filled with water under the test stand. Purge the system for 10 minutes and contact Scott Meyer or a professor immediately.**						
4.016		SAF	Turn off warning siren						
4.017		DSO	After completing initial purge, CLOSE WFNA run valve PV-Run-00						
4.018		DSO	Cycle WFNA dump valve PV-Dump-01 several times to dump any residual WFNA retained between T-fitting and dump valve.						
4.019		DSO	Cycle run valve PV-Run-00 and leave open for a minute at least 3 times. If no vapor/smoke is observed after 3th cycle, continue the procedures. Otherwise, continue cycling until vapor/smoke is no longer observed						
4.020		DSO	Verify there is no smoke or fumes exhausting from motor nozzle via video cameras						
4.021		DSO	Close WFNA run valve PV-Run-00						
4.022		DSO	Unload ER3000						
4.023		DSO	CLOSE N2 electronic regulator isolation valve PV-ER-03						
4.024		DSO	Open vent valve PV-vent-02						
4.025		TOP/TC	Don proper PPE for handling of nitric acid including Tyvek suit, appropriate large over boots, nitrile gloves, safety glasses, positive pressure hood, chemical resistant over gloves, and arm protectors						
4.026		SAF	Remove chain from in front of T-cell door, open test cell door and confirm there is no smoke or fumes coming from motor nozzle						
4.027		TOP	Turn off water supply to water sheet generator						
4.028		SAF	Remove safety chain from blast room door						
4.029		SAF	Turn off inside and outside warning lights						
4.030		TOP	Move exhaust guide pipe to allow access to bolts on motor nozzle retainer plate						
4.031			**NOTE: some liquid WFNA may still be present between phenolic tube and motor housing**						
4.032		TOP	Check for any acid at fittings and if necessary, wipe off using kimwipe and place in 5 gallon bucket of water						
4.033		TOP	Remove bolts from aft flange that attaches the nozzle retainer plate to the body of the motor, remove nozzle retainer plate						
4.034		TOP	Disconnect data cable on chamber PT (PT-CC-08)						

4.035		TOP	Remove bolts from intermediate flange located between the nozzle retainer plate and the main combustor flange (i.e. the section housing the fuel grain) and remove the aft motor section						
4.036		TOP	Remove nozzle/post combustion chamber/fuel grain assembly						
4.037		TOP	Place nozzle in ziploc bag labeled with current test number						
4.038		TOP	Using kimwipe and DI water, wipe down interior/exterior of motor. Place used kimwipes in 5 gallon bucket of water						
4.039		TOP	Using kimwipe and DI water, wipe down exterior of phenolic tube. Place used kimwipes in 5 gallon bucket of water						
4.040		TOP	Weigh post-fire fuel grain mass and measure approximate center port diameter (if practical), record on test data sheet						
4.041		TOP	Place fuel grain in ziploc bag labeled with test date and number						
4.042		TOP	Unscrew injector from injector flange						
4.043		TOP	Disassemble and clean injector						
4.044		TOP	Reassemble and install injector back in injector flange						
4.045		TOP	Turn off large industrial fan						
4.046		DSO	Ensure valves are in their appropriate de-energized states						
4.047		DSO	Turn off instrumentation and valve power						
4.048		DSO	Stop the labview VI and restart for next test (or stand safing)						
4.049		DSO	Turn on instrumentation and valve power						
4.050			If more tests are to be conducted, return to SECTION: 2. If test series is completed, proceed to SECTION: 5						
4.051				REQ'D PERSONNEL: TOP, SAF, DSO PPE: Gloves, Goggles, Lab coat, Face Shield					
5.000		TOP	Turn on large industrial fan						
5.001		DSO	Verify valves are in their appropriate de-energized states						
5.002		DSO	OPEN N2 electronic regulator isolation valve PV-ER-03						
5.003		DSO	Set ER3000 pressure to 200 psi and vent for 5 minutes through vent valve PV-Vent-02						
5.004		DSO	Set ER3000 pressure to 0 psi						
5.005		TOP	Reattach aft motor section to main motor section and tighten bolts						
5.006		TOP	Place blue flashbreaker tape over exit of Aft motor section						
5.007		TOP	CLOSE system nitrogen supply pressure manual valve MV-N2-05						
5.008		DSO	Set ER3000 pressure to 50 psi to slowly bleed off residual system pressure via vent valve PV-Vent-02						
5.009		DSO	Once residual line pressure reaches approximately 200 psi, set ER3000 pressure to 0						
5.010		DSO	CLOSE N2 electronic regulator isolation valve PV-ER-03						
5.011		DSO	Verify valves are in their appropriate de-energized states						
5.012		TOP	UNLOAD Pneumatic valve actuation supply pressure regulator MR-N2-03 to 50 psig						
5.013		TOP	Vent residual line pressure via manual valve in T-cell control room						
5.014		DSO/TOP	Verify system pressure has been properly vented down to atmospheric pressure						
5.015		TOP	UNLOAD Pneumatic valve actuation supply pressure regulator MR-N2-03						
5.016		TOP	CLOSE test stand manual isolation valve MV-WFNA-1						
5.017		SAF	Announce the test cell is safe and open to all personnel						
5.018		DSO	Turn off valve and instrumentation power						
5.019		DSO	Shutdown labview						
5.020		DSO	Turn off SCXI chassis						
Section 6: EMERGENCY PROCEDURES									
IN CASE OF FIRE:									
6.001			CALL fire department at 9-1-1						
IN CASE OF SEVERE INJURY:									
6.002			IF ambulance treatment is necessary, dial 9-1-1						
6.003			TRANSPORT injured party away from area only if in danger of further injury						
6.004			SECURE test cell area, if safely possible.						
6.005			If test cell cannot be safely secured, monitor until appropriate safety personnel are present						
6.006			Contact Scott Meyer and any appropriate professors						

MEDICAL CARE INFORMATION
Purdue University Student Health Center
Phone: 765-494-1724
Location: Corner of University st. and Stadium Ave. (near ARMS/Civil/WTHR)

IU Health Arnett Hospital
Phone: 765.448.8000
Location: 5165 McCarty Ln